SUBJECT-SPECIFIC COMPUTATIONAL FLUID-STRUCTURE INTERACTION MODELING OF TYPE-1 THYROPLASTY

By

Amit Goraksh Avhad

Dissertation

Submitted to the Faculty of the

Graduate School of Vanderbilt University

in partial fulfillment of the requirements

for the degree of

DOCTOR OF PHILOSOPHY

in

Mechanical Engineering
May 10, 2024
Nashville, Tennessee

Approved:

Haoxiang Luo, Ph.D.

Bernard Rousseau, Ph.D.

Ravindra Duddu, Ph.D.

Robert Pitz, Ph.D.

Caglar Oskay, Ph.D.

To all my friends and family.

ACKNOWLEDGMENTS

I would like to express my deepest gratitude to my advisor, Professor Haoxiang Luo, for his guidance, support, and encouragement throughout my doctoral studies. His profound knowledge in the field has been instrumental in my academic and personal growth.

I am immensely grateful to the Department of Mechanical Engineering at Vanderbilt University for providing me with the opportunity to pursue my PhD studies.

I extend my sincere gratitude to Dean Bernard Rousseau, the Principal Investigator of this research, for his unwavering support and encouragement throughout our research endeavors. His expertise in the field and his commitment to fostering a collaborative research environment have been invaluable to our team's success.

I am also deeply grateful to my dissertation committee members, Professor Robert Pitz, Professor Caglar Oskay, and Professor Ravindra Duddu, for their invaluable insights, constructive feedback, and unwavering support throughout my research journey. Their guidance has been instrumental in shaping my work and expanding my understanding of the field.

I would like to express my gratitude to our research collaborators at the University of Pittsburgh, Lea Sayce and Azure Wilson, for their valuable contributions to our research projects.

I am thankful to senior lab members Dr. Siyuan Chan and Dr. Zheng Li for their guidance and support in my research work. I would like to extend my gratitude to ACCESS and Stampede2 for granting us access to their high-performance computing resources, enabling us to execute our simulations and significantly advance our research endeavors.

I am grateful for the financial support received from the National Institute on Deafness and Communication Disorders of the National Institute of Health under award number 5R01DC016236, which has played a crucial role in the realization of this research.

TABLE OF CONTENTS

LIST OF TABLES

LIST OF FIGURES

CHAPTER 1

Introduction

1.1 Vocal fold vibration during phonation

1.1.1 Physiology of human voice production

Human voice production is a complicated physical process that involves coordinated work of a generator (the lung), an oscillator (the larynx), a resonator (the three-dimensional space including the oral cavity, nasopharynx, sinuses, and nasal cavity), and articulators (the tongue, cheeks, teeth, and lips). When the air driven by the pressure in the lung passes through the trachea and then the glottis hosted in the larynx, the flow causes the vocal fold (VF), a pair of elastic tissue folds stretched across the larynx, to oscillate. This flow-induced vibration is called phonation, and it produces sound with a fundamental frequency that is the same as the vocal fold vibration frequency. The sound then resonates in the space of the resonator, forming harmonic waves, and is further shaped by the articulators to become recognizable words.

In addition to the proper structural and material properties of the VF tissue, the onset of healthy phonation requires that the lung pressure be above a threshold level (Titze, 1992) and that the two sides of the VF be abducted toward the midline by the laryngeal muscles to form a narrowed or closed glottis (Van den Berg et al., 1957). Under such conditions, the air from the lung pushes the VF to open slightly so that it goes through the glottis. As the air flows through the glottis at a fast speed, however, the intraglottal pressure drops due to the Bernoulli effect. Thus, the VF recoils back to its position, and the glottis closes up again. As long as the conditions are maintained, this opening-closing cycle repeats itself, and the VF vibration is sustained without the necessary additional muscle input (Titze, 1994).

In terms of the roles of various muscles involved in phonation, the laryngeal muscles including the thyroarytenoid, interarytenoid, and the lateral cricoarytenoid muscles are re-

sponsible for the VF adduction prior to phonation, and the posterior cricothyroid is responsible for the VF abduction (separation) (Saran et al., 2023). During phonation, the thyroarytenoid and cricothyroid muscles work in a coordinated manner to control the pitch of voice (Yin and Zhang, 2013). The cricothyroid muscle contraction causes the thyroid cartilage to tilt forward, which elongates the VF and increases its tension, thus raising its natural vibratory frequency. On the other hand, the thyroarytenoid contraction is more complicated, and it may either increase or decrease the VF stiffness (and thus the frequency) depending on the state of the VF and simultaneous contraction of the cricothyroid (Yin and Zhang, 2013). Since all these muscles have distinct and important roles, any disruption to their activation would cause abnormality in voice production.

1.1.2 Unilateral vocal fold paralysis (UVFP) and type-1 thyroplasty

Voice is the most important tool for our daily communications. Any disorder inside the glottis may have adverse effects on phonation in addition to breathing or swallowing (Ruben, 2000; Wilson et al., 2021). Such voice disorders are debilitating and can lead to significant socioemotional consequences, loss of income, and long-term disability. One major voice disorder is unilateral vocal fold paralysis (UVFP), which is mostly caused by damage to the vagus nerve or the recurrent laryngeal nerve as a result of cancers, trauma, or surgery (Kelchner et al., 1999; Paniello et al., 2011; Francis et al., 2014). Due to the nerve damage, one side of the VF cannot be abducted or medialized toward the midline by the neurological command. Thus, the glottis is unable to close up despite that the healthy side is medialized. As a result, the VF vibration cannot be induced by the airflow normally by the fluid-structure interaction (FSI) mechanism, or there is only a little vibration. In this condition, patients have difficulty producing voice and may show symptoms of dysphonia, dysphagia, and aspiration (Leder et al., 2012). Based on incidence rates and frequency of thyroid and cervical spine surgeries, it is probable that over 20,000 new patients are diagnosed with UVFP due to surgical causes annually. These account for only 50% of incident

UVFP cases. Thus, conservative estimates place the annual incidence of UVFP diagnoses upwards of 40,000 in the United States alone.

Otolaryngologists have several interventional options in UVFP treatment such as thyroplasty, arytenoid adduction, injection laryngoplasty and laryngeal reinnervation (Siu et al., 2016). One of the most common methods for UVFP treatment is medialization, pushing the paralyzed side toward the midline, using an implant in a surgical procedure (Francis et al., 2014), i.e., type-1 thyroplasty. Payr (1915) originally described medialization thyroplasty for paralyzed VF by pressing inward the thyroid cartilage flap. Later, Isshiki et al. (1975) modified the procedure by using a silastic implant through a window created in the thyroid cartilage. This method was made popular by Koufman (1986), and since then it has become standard care in the long-term treatment for UVFP (Woo et al., 2001).

1.1.3 Optimization of type-1 thyroplasty

Since its introduction in 1975 (Isshiki et al., 1975), type-1 thyroplasty has emerged as a cornerstone of surgical interventions for UVFP. The procedure revolves around the experiential placement of a medialization implant into the thyroid cartilage to restore VF vibration and improve voice quality (Francis et al., 2014; Cameron et al., 2020; Reddy et al., 2022; Daniero et al., 2014). Although it is generally a safe procedure, type-1 thyroplasty still has significant limitations in restoring patients' voice. Since the FSI of phonation requires the intricate interplay of the airflow and the VF tissue, the implant needs to be designed and placed carefully for it to have the maximal beneficial effect on the voice production of individual patients. On the other hand, there is a lack of specific guidance for the best location, size, and shape of the implant, and the surgeons have to rely heavily on their experience and intraoperative assessments (Iwahashi et al., 2015). To date, the pre-operative optimization of the implant for individual patients remains a complex and subjective endeavor.

From numerous studies on laryngoplasty revision (Woo et al., 2001; Netterville et al., 1993; Maragos, 2001; Lundeberg et al., 2011; Andrews et al., 2008; Cohen et al., 2004;

Iwahashi et al., 2015), not all patients have been reported to achieve satisfactory outcomes following type-1 thyroplasty. This situation highlights the need for a more thorough understanding of the factors that contribute to successful or unsuccessful outcomes.

Woo et al. (2001) identified a persistent posterior glottic gap as one of the most common causes of unsuccessful type-1 thyroplasty. They recommended arytenoid adduction in addition to type-1 thyroplasty for patients with vocal fold level differences or a large posterior glottic gap. Other studies have reported the common causes of failed type-1 thyroplasty due to implant window misplacement on the thyroid cartilage (Maragos, 2001; Andrews et al., 2008; Zapater et al., 2019; Desuter et al., 2020), oversized implant usage (Netterville et al., 1993; Lundeberg et al., 2011), and inappropriate insertion depth of the implant (Maragos, 2001; Desuter et al., 2017). In addition, Cohen et al. (2004) discussed the failure due to inadequate or excessive VF repositioning.

Medical imaging, e.g., computed tomography (CT) and magnetic resonance imaging (MRI) scans, has proven to be very effective in assessing the pre- and post-surgical states of the larynx for the individuals undergoing UVFP treatment (Zeiberg et al., 1996; Yumoto et al., 1999; Hiramatsu et al., 2008). In addition, Yumoto et al. (1999) reported the ability of CT endoscopic images to visualize sagging/thinning and adduction/augmentation of the affected VF before and after type-1 thyroplasty. Hiramatsu et al. (2008) further demonstrated the potential of CT images acquired during glottal closure and glottal opening to provide insights into the underlying causes of unsatisfactory outcomes after type-1 thyroplasty. Furthermore, Hara et al. (2014) showed that preoperative determination of the window position in type-1 thyroplasty using reconstructed CT images resulted in favorable vocal outcomes. Iwahashi et al. (2015) discussed the importance of integrating CT images in the comprehensive assessment of VF positioning for surgical planning.

A recent study by Desuter et al. (2017) points out the importance of the shape of the larynx, and particularly the shape of the thyroid cartilage, in the outcome of type-1 thyroplasty. This study discussed that females have a distinct larger thyroid angle compared

to men and thus a gender-specific surgical approach is essential to improve the outcome.

Some earlier mathematical models may offer a means of approximating the VF location (Tucker et al., 1993; Meiteles et al., 1992), but their reliability was limited due to the individual differences in anatomy and physiology (Laccourreye et al., 2021; Zapater et al., 2014). These differences are particularly discussed through experimental procedures by Zapater et al. (2019), who extended beyond gender-specific differences and sought for the optimal placement of the thyroid cartilage window.

These previous studies have shown that type-1 thyroplasty should be highly patient-specific. On the other hand, even though many studies have focused on the effects of implant parameters, such as implant material (Palaparthi et al., 2019; Wu and Zhang, 2023), insertion depth (Smith et al., 2020), and shape (Zhang et al., 2015), there is still a lack of effective approach to determine the optimal implant parameters for individual UVFP patients (Movahhedi et al., 2021; Orestes et al., 2014). The challenges stem from several inherent factors such as the complex effects associated with the implant parameters, variations from individual anatomy, and limited trials during the surgery. As a result of these challenges, although type-1 thyroplasty is currently the accepted gold standard for the treatment of glottic insufficiency in UVFP, its outcome still needs to be improved. In fact, a reported 4.5% – 16% of implant procedures require revision (Parker et al., 2015; Wilson et al., 2021; Woo et al., 2011; Nasseri and Maragos, 2000; Cohen et al., 2004; Maragos, 2001)

To address the challenges, there is a need to focus on developing surgical planning tools that can accurately predict the effects of implant parameters such as location and insertion depth on the VF vibration during phonation. Since the FSI is a mechanical process involving fluid dynamics of the glottal airflow and solid mechanics of the VF tissue, computational modeling of this FSI process would have the potential to predict the effects of the implant using a physics-informed approach. Especially, the techniques of high-fidelity computational modeling have advanced greatly in recent years because of the fast growth in

high-performance computing and also because of the availability of high-resolution medical imaging that can capture the specific laryngeal anatomy of individual patients. Now it is possible to explore the potential of computational modeling as a surgical planning tool.

In clinical applications, such a physics-based computational modeling tool promises to simulate the effects of different implant parameters on the VF vibration and could be used to optimize those parameters for surgical planning. The resulting information can provide surgeons with individualized predictions of implant effects, enabling them to make informed decisions that help reduce the demand for surgeons' experience and help improve the surgical outcome.

1.2 Computational modeling of vocal fold vibration

Computational modeling of VF vibration has useful applications in the fundamental understanding, diagnostics, and management (e.g., surgical planning) of voice disorders (Titze, 1994; Mittal and Iaccarino, 2005; Mittal et al., 2013; Wilson et al., 2021; Yang et al., 2017). With the growth of computational resources and improvement of the modeling approach, computational models for the FSI of VF vibration have advanced substantially in recent years. These models typically couple a 2D or 3D glottal airflow model and a finite-element representation of the VF tissue (Alipour et al., 2000; Hunter et al., 2004; Thomson et al., 2005; Cook and Mongeau, 2007; Luo et al., 2008, 2009; Zheng et al., 2010; Shurtz and Thomson, 2013; Chang et al., 2013; Zhang, 2017; Yang et al., 2017, 2018). These models adopt an increasingly high resolution and have provided an insightful fundamental understanding of the FSI system such as vortex dynamics, pressure on the VF surface, tissue deformation pattern, energy transfer, and acoustic wave. In these references, the VF was often represented by a schematic that captures only the overall characteristics of the laryngeal geometry. Such models are obviously not sufficient for realistic or subject-specific representation.

The advancement of medical imaging technologies such as magnetic resonance imaging

(MRI) have permitted the subject-specific features in the laryngeal geometry. For example, Wu and Zhang (2016) used an MRI-derived human VF model to perform a study of the geometric parameters. A recent study by Xue et al. (2014) presented a 3D FSI simulation using the subject-specific geometry of the human larynx based on MRI data. This research particularly highlighted the importance of the use of actual geometries as compared with simplistic models in the previous FSI studies. The authors pointed out the asymmetry observed in the flow in the supraglottal region when viewed in the mid-sagittal plane. This flow behavior was mainly attributed to the asymmetry in the geometry. A similar study was carried out for avian phonation using subject-specific geometries (Jiang et al., 2020).

Despite their significant advancement, these studies have the limitation of being unable to prescribe the individual characteristics of the VF tissue's material properties, and the tissue specifications were primarily based on the general population's data. Generally, there has been a lack of available experimental validation for subject-specific computational models of VF in the literature. One of the reasons for very few studies on the subject-specific FSI study of the VF is the high computational cost of simulating the problem. Even with the availability of high-performance computers for fast calculations, the complex anatomy of the larynx and VF movement pose a huge challenge for meshing in the 3D computational fluid dynamics of the glottal airflow. Another major challenge is the uncertain material properties, which could be significantly different among individuals. Within a species, every individual VF has unique material properties (Chan et al., 2007; Riede and Titze, 2008). This unavailability of the individual tissue properties restricts the validity of a subject-specific FSI model.

In addition to these difficulties on the modeling side, setting up corresponding experiments to test and validate the subject-specific computational model has its own challenges, especially for in vivo phonation, e.g., obtaining the 3D scan data and high-speed images of VF vibration in addition to managing the VF adduction.

There have been a few computational studies that focus on the biomechanics of diseased

VFs such as vocal fold nodules (Jiang et al., 1998), scars (Berry et al., 2005), polyps (Ji et al., 2022), and UVFP (Li et al., 2021b). Most of these studies were limited to greatly simplified laryngeal geometries that do not represent the actual anatomy. One exception is that of Li et al. (2021b), where a subject-specific model of the rabbit VF was developed to model the UVFP mimicked in the animal experiment and to analyze the fundamental frequencies of the two sides using an eigenmode approach.

To the best knowledge of the author, there is only one computational study available at present for type-1 thyroplasty (Movahhedi et al., 2021), which presents the medialization process and resulting phonation characteristics by using FSI modeling. In their study, the muscle activation-enabled finite-element model is used besides the implantation process for achieving the vocal fold pre-phonation posturing, and the subsequent FSI was simulated to obtain the VF vibration. However, in their FSI model, a simple one-dimensional (1D) flow model was used for the glottal airflow, and a generic tissue model was adopted to represent the larynx. Furthermore, there was no experimental validation for their numerical model.

In summary, despite the progress on the computational modeling of phonation, there is still much work to do toward patient-specific modeling of the VF vibration, especially in incorporating the detail of the material properties of the tissue as well as in coordinated experimental and computational efforts to validate such computational models. In my dissertation, we will address this technical gap and advance the computational modeling of vocal fold vibration toward patient-specific applications.

1.3 Summary of this research project

This research project is built upon the existing work in our group at Vanderbilt University on computational FSI of phonation. In the past, our group has developed a 3D numerical FSI method that is versatile and suitable for a range of biological and biomedical programs involving flow at moderate Reynolds numbers interacting soft tissue deformations (Luo et al., 2008, 2009, 2012; Tian et al., 2014; Chang et al., 2015; Chen and Luo, 2020). In

addition, a suite of computational modeling tools have been developed by our group to address the FSI of phonation in a complementary manner, for example, simplified 2D (Luo et al., 2008, 2009), 3D (Tian et al., 2014), subject-specific laryngeal geometries (Chang et al., 2015), as well as a simplified 1D glottal flow model that was later enhanced by machine learning (Li et al., 2020; Chen et al., 2020; Li et al., 2021a).

Along the same line of work by the previous group members, my project will extend the use of subject-specific FSI models that are built from laryngeal image data and incorporate individual sample's tissue properties. Furthermore, my project will focus on the integrated experimental/computational study and validation of the computational model. Although the experiment is performed by our collaborators at the University of Pittsburgh, it is an integral part of this research and will thus be included in this dissertation with necessary acknowledgments.

Overall, our research can be divided into three separate parts in terms of specific objectives and research tasks. Each part is briefly summarized below and will be expanded in a chapter later.

In the first part of this dissertation (Chapter 3), we will consider modeling of healthy VF vibration along with experiment validation. Specifically, a full 3D FSI study of the subject-specific VF vibration will be carried out based on the previously reconstructed VF models of rabbit larynges. The primary focuses are the vibration characteristics of the VF, the unsteady 3D flow field, and a comparison with a recently developed 1D glottal flow model that incorporates machine learning, as well as against the *in vivo* animal phonation experiment. Five different samples of the rabbit larynx, reconstructed from MRI scans after the in vivo phonation experiments, will be used in the FSI simulation. These samples have distinct geometries and different inlet pressures measured in the experiment. Furthermore, the material properties of the VF tissue have been determined previously for each individual sample. we will discuss comparisons of the VF vibration and intraglottal pressure against previous results including experiment data, the roles of the inferior and supraglottal

geometries, as well as the significance of the flow pattern.

In the second part (Chapter 4), we will conduct a subject-specific modeling for type-1 thyroplasty of an excised rabbit larynx. The VF model will be built using the preoperative MRI scan. Two steps of simulations will be carried out in this work: 1) FEM simulation of medialization (both type-1 thyroplasty and the healthy medialization that are mimicked in the experiment), and 2) FSI simulation of vibration of the medialized VF. These two simulations will be validated separately. The simulation of medialization is validated against the postoperative MRI scan, and the simulation of vibration is validated against the high-speed video data. To my knowledge, this is the first attempt of subject-specific FSI modeling of the vF and also the first attempt of its experiment validation.

In the third part (Chapter 5), we will perform an optimization study of the implant placement using the 3D FSI model that is built in the second part. Specifically, the window location on the thyroid cartilage will be systematically varied, and for each location, the two-step simulation (medialization and then FSI) will be repeated to obtain the new VF configuration and the vibration characteristics. We will compare the degrees of VF medialization as well as the vibratory characteristics of these cases and evaluate the optimal design based on the results. Although experiment validation is not available for the optimized design, this study represents a demonstration of using 3D subject-specific modeling to perform optimization and planning of type-1 thyroplasty.

Finally, we will discuss in Chapter 6 the future work toward applying our computational tools in the eventual application of surgical planning for type-1 thyroplasty.

CHAPTER 2

Numerical method for fluid-structure interaction simulations

2.1 Introduction

A high-fidelity subject-specific computational model of phonation involves a complex 3D geometry of the lumen surface reconstructed from images of the larynx, which will be used in the computational fluid dynamics (CFD) of the airflow in the FSI simulation. The numerical method in the CFD also has to deal with moving boundaries that are caused by dynamic deformation of the vocal fold during vibration. Sometimes the glottis may fully close, thus cutting the flow domain into two separate parts. Such complex and moving geometries are extremely challenging for conventional CFD methods due to the requirement for frequently re-meshing the domain during the simulation. For this purpose, I have adopted a versatile immersed-boundary method that was previously developed and fully parallelized in our lab. For the tissue mechanics, a nonlinear finite-element method has been incorporated to perform coupled FSI simulations. In this chapter, I will summarize the methods for the flow, the solid, and their coupling. Further details can be found in previous publications from our group, especially in (Luo et al., 2012) and (Tian et al., 2014).

2.2 Governing equations and numerical method

2.2.1 Immersed-boundary method for the flow

Glottal airflow is a 3D pulsatile jet characterized by turbulence in the supraglottal region (Alipour et al., 1996; Lasota et al., 2021) and has an average speed on the order of 30 m/s. Therefore, its Mach number is low, and the jet can be approximated as an incompressible flow for the purpose of flow-induced vocal fold vibration. Acoustic wave propagation is not part of our flow model, and its effect on the vocal fold vibration is considered negligible.

The flow is thus governed by the 3D viscous incompressible Navier-Stokes equation

that includes the momentum and continuity equations,

$$\frac{\partial v_i}{\partial t} + v_j \frac{\partial v_i}{\partial x_j} = -\frac{1}{\rho}\frac{\partial p}{\partial x_i} + \nu \frac{\partial^2 v_i}{\partial x_j^2} \tag{2.1}$$

$$\frac{\partial v_i}{\partial x_i} = 0 \tag{2.2}$$

where v_i is the velocity vector, ρ and ν are constant density and kinematic viscosity of the air, respectively, and p is the pressure. The lumen surface is assumed to be a no-slip and no-penetration wall (Figure 2.1 (b)). At the subglottal inlet, a constant gage pressure of around 1 kPa is assumed to drive the flow. At the supraglottal outlet, ambient conditions are assumed where the gage pressure is 0 kPa.

A non-uniform cartesian grid with a cell-centered and non-staggered arrangement is used to discretize the governing equations (Figure 2.2). The Navier-Stokes equation is solved using a fractional-step method that includes three steps. An advection-diffusion equation without pressure is solved in the first step by using the Crank-Nicolson scheme. A second-order central scheme is used to discretize all the spatial derivatives which improves numerical stability. A projection method approximates the pressure and then the pressure Poisson equation is solved by using the multigrid method.

For the immersed-boundary method, a set of Lagrangian marker points and triangular elements represent the solid body surface, which allows efficient geometrical quantity calculations such as the surface normal, interpolation over the surface, and fluid/solid node identification. As shown in Figure 2.2, each of the nodal points on the Cartesian grid is identified either as a "fluid" node or a "solid" node. The fluid nodes immediately next to the solid surface are further identified as "hybrid" nodes, and the solid nodes immediately next to the solid surface are further identified as "ghost" nodes. For the fluid nodes away from the solid surface, the second-order central finite-difference method can be implemented in a standard manner. However, the hybrid nodes and ghost nodes require special treatment as briefly described next.

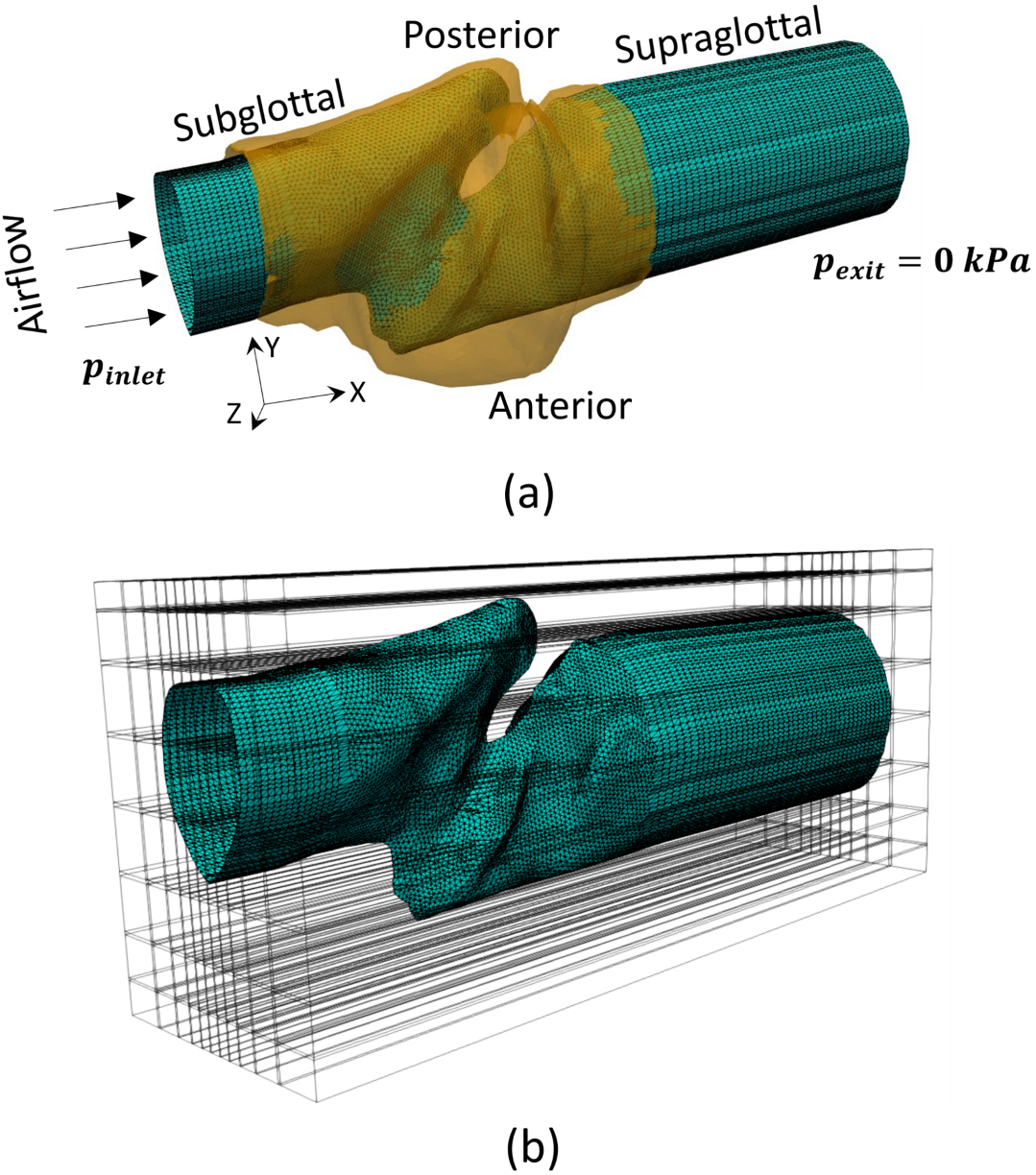

Figure 2.1: (a) The computational FSI model showing the flow domain (lumen) in the blue surface mesh and the tissue domain in transparent orange. (b) 2D decomposition of the flow domain for parallel computation, where each block represents a sub-domain for parallel computing.

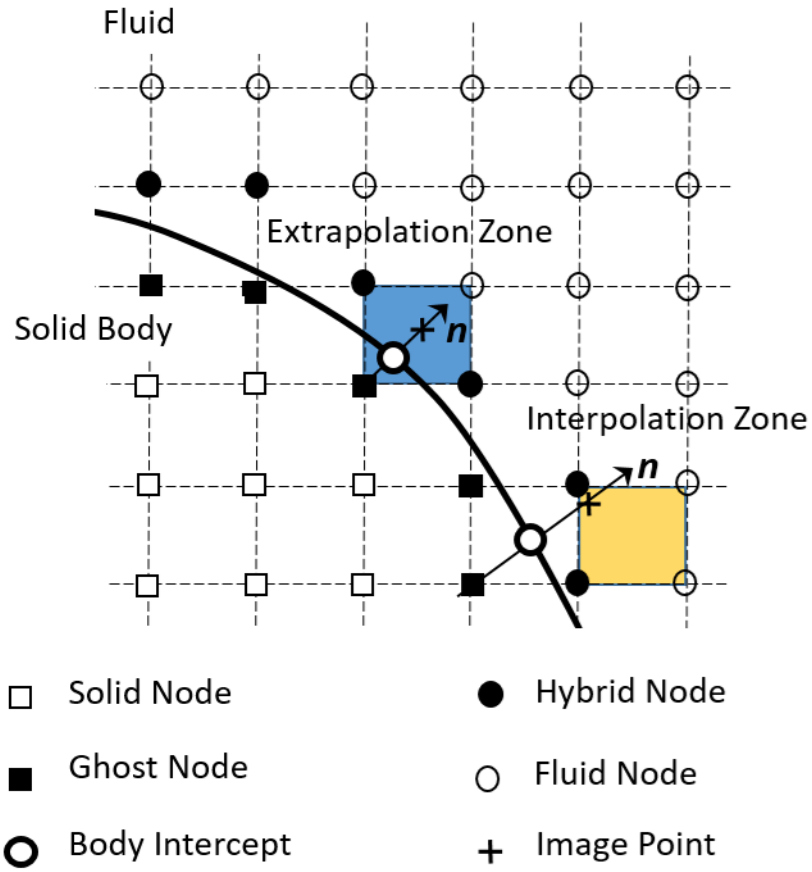

Figure 2.2: Illustration of the immersed-boundary method using a 2D Cartesian grid.

At a ghost node, flow variables, i.e., the velocity and pressure, are extrapolated from the fluid nodes near the ghost node and its projection onto the boundary, where the boundary conditions at the project point are involved in the extrapolation. At a hybrid node, both interpolation and governing equations are used to obtain the flow variables. The interpolation involves the fluid nodes nearby as well as the boundary conditions at the projection of the hybrid node onto the boundary. To balance between the interpolation and the governing equation, a weighted average is calculated based on the distance of the hybrid node to the boundary. This approach handles a node switching its identity between an interior fluid node and a solid ghost node as the boundary moves across the grid, and it alleviates the numerical oscillations associated with the boundary movement (Luo et al., 2012).

2.2.2 Finite-element method for the tissue

The dynamic solid-body deformation is governed by the equation of elasticity:

$$\rho_s \frac{\partial^2 u_i}{\partial t^2} + \eta_d \frac{\partial u_i}{\partial t} = \frac{\partial \sigma_{ij}}{\partial x_j} \tag{2.3}$$

where u_i is the displacement vector, ρ_s is the material density, η_d is the mass damping coefficient, and σ_{ij} is Cauchy stress tensor.

During vibration, vocal fold displacement is on the order of 1 mm. In comparison, the vocal fold length is about 1 cm in humans. The relative deformation is thus small. However, previous studies have shown that the nonlinear strain may still play a significant role as a small displacement of the medial surface of the vocal fold would significantly affect the glottal flow and the pressure load, which would in turn influence the vocal fold vibration. Therefore, we adopt the hyperelastic Saint-Venant Kirchhoff model to represent the elastic tissue, which incorporates nonlinear strains due to finite displacements.

2.2.3 Method of FSI coupling

The incompressible Navier-Stokes equation is solved on the fluid domain, while the structural dynamics equations are solved on the solid domain. The Lagrangian mesh of the solid is independent of the Cartesian mesh used by the flow solver. The two domains are coupled through the boundary conditions, which enforce the no-slip, no-penetration, and traction conditions,

$$\mathbf{v} = \mathbf{v}_b, \quad \mathbf{f} = \sigma \cdot \mathbf{n}, \quad at \quad \mathbf{X} = \mathbf{X_b}, \tag{2.4}$$

where $\mathbf{X}$ and $\mathbf{v}$ are, respectively, the position and velocity of the boundary, $\mathbf{f}$ is the traction on the boundary which includes the pressure and viscous stress, σ is the stress tensor in the flow, and $\mathbf{n}$ is the surface normal. The no-slip and no-penetration conditions state that the fluid velocity at the boundary must be equal to the velocity of the solid. The traction condition states that the force exerted by the fluid on the boundary is equal to the load on the solid.

An explicit coupling approach for FSI coupling is straightforward but can lead to numerical instability. To improve stability, an implicit coupling approach based on iterations is employed, where the flow and solid solvers are repeatedly iterated and the boundary conditions are updated. Verification and validation studies of this FSI method can be found in a previous work of our group (Tian et al., 2014).

2.3 The 1D flow model used for comparison

Recently, some former members of our group have developed a 1D pulsatile flow model for glottal airflow that incorporates machine learning (Chen et al., 2020; Li et al., 2021a). In this model, the continuity and momentum equation are written as

$$\frac{\partial A}{\partial t} + \frac{\partial Au}{\partial x} = 0 \tag{2.5}$$

$$\rho \frac{\partial u}{\partial t} + \rho u \frac{\partial u}{\partial x} = -\frac{\partial p}{\partial x} + \frac{\partial \tau}{\partial x} \tag{2.6}$$

where $u(x,t)$ and $p(x,t)$ are the flow velocity and pressure, respectively, A is the effective cross-sectional area of the vocal fold lumen, and τ represents the pressure loss due to viscous and flow separation effects. Since the entrance effect is considered as the flow enters the narrow glottis from the subglottal region, A is based on correction of the actual cross-sectional area (Li et al., 2020; Chen et al., 2020).

To incorporate the area correction, a correction coefficient, α, is defined so that $\alpha(x) = A(x)/A_0(x)$, where $A_0(x)$ is the actual cross-sectional area as shown in Figure 2.3.

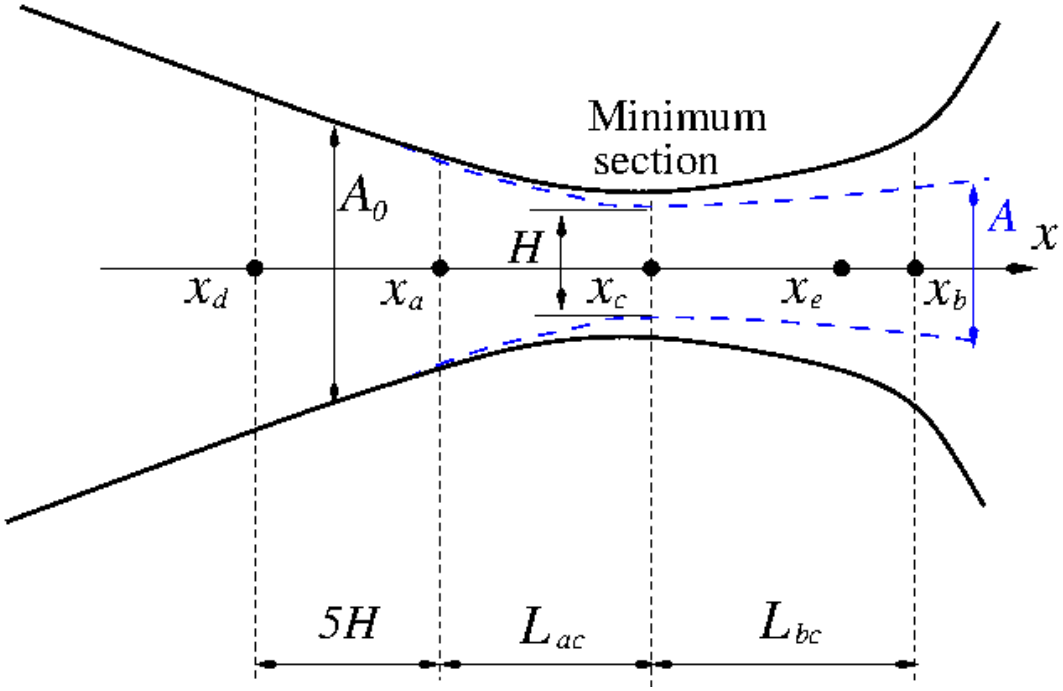

Figure 2.3: Schematic for the 1D pulsatile flow model, where the characteristics of the vocal fold are described by a simple 2D converging-diverging channel. Here x_c is the narrowest section, x_a is an inferior location, x_b is the glottal exit, x_e is an intermediate location in the diverging section, and x_d is a subglottal location.

In the 1D model, $\alpha(x)$ is assumed to be a parabolic function with $\alpha = 1$ at x_c and $\mathrm{d}\alpha/dx = 0$ at x_b. Thus, only $\alpha(x_b)$ needs to be determined. For the pressure loss, $\tau(x_e)$ and $\tau(x_b)$ are to be determined, and $\tau(x)$ follows an assumed 3rd-order polynomial function between x_a and x_b.

The non-dimensional variables describing the flow are the Reynolds number Re, the divergence angle r_b, the length of the divergence section l_{bc}, the inferior section angle

r_a, the length of the convergence section l_{ac}, and the subglottal section angle r_d. These variables are defined as

$$\begin{aligned} r_b &= A(x_b)/A(x_c) \\ l_{bc} &= L_{bc}/H \\ r_a &= A(x_a)/A(x_c) \\ l_{ac} &= L_{ac}/H \\ r_d &= A(x_d)/A(x_a) \\ Re &= \rho\, u_c H/\mu. \end{aligned} \tag{2.7}$$

Using these input variables, Li et al. (2021a) used a machine learning model to determine the area correction coefficient α and pressure loss parameters. The enhanced flow model was used for FSI simulation of the vocal fold vibration, which produced agreeable results with the experiment data (Li et al., 2021a).

CHAPTER 3

Subject-specific modeling of healthy phonation

3.1 Introduction

In this chapter, we consider the computational modeling of healthy phonation and its experiment validation. As discussed in Chapter 1, an integrated computational/experimental study for model development and validation is still lacking. This issue will be addressed here using healthy phonation as the first step.

The animal experiment and larynx reconstruction based on the MRI scan have been done previously in our lab (Chang et al., 2015). This work is built upon the previous work by using the rabbit larynx models constructed by Chang et al. (2015), but 3D FSI simulation, validation, and detailed analyses are the main focus of the present work. The use of rabbit models in this research is justified due to the similarities in laryngeal size and histological features between rabbits and humans (Thibeault et al., 2002; Henrich et al., 2003). Previous studies have contributed to our understanding of the rabbit larynx's phonatory characteristics, making it a suitable model for studying vocal fold behavior and potential interventions (Döllinger et al., 2018). The insights gained from this research can have implications for future studies involving human subjects and further our understanding of vocal fold function and voice disorders.

The overall study is summarized below. Live rabbits were used for evoked *in vivo* phonation tests with simultaneous high-speed imaging and subglottal pressure measurement Novaleski et al. (2016). The larynx was excised after the tests for MRI scan and geometric reconstruction. The finite-element model (FEM) of the vocal fold tissue was then built for FSI analysis. Furthermore, the tissue stiffness properties were adjusted in a simplified FSI model, i.e., a 1D flow coupled with 3D FEM, to match the vibration frequency of each individual sample. The resulting FSI model therefore has both geometric and ma-

terial features of individual subjects. 3D FSI simulations of such subject-specific models are performed to investigate the flow and vocal fold behavior. The results will be compared with the *in vivo* phonation data for validation, as well as with the previous 1D-flow FSI for comparison. Furthermore, the flow analyses will provide an in-depth understanding of rabbit phonation and lead to a constructive discussion on the validity of using rabbits as an alternative to human study.

3.2 Construction of subject-specific models

MRI scans are performed on the excised larynx in the pre-phonatory and post-phonatory states. These scans help capture the morphological details of tissue and distinguish cartilage. Following details are for the five samples discussed in the current chapter. The excised larynges are placed in a 12 ml syringe with Fomblin 06/6 perfluoropolyether (Solvay Solexis, Thorofare, NJ) and having a 38-mm inner diameter radiofrequency coil. T2-weighted-prep with an echo train length of 40 and repetition time of 550 ms is used. A Varian 9.4 T horizontal bore imaging system (Varian Inc., Palo Alto, CA) provides multi-scale scout images in the axial, coronal, and sagittal planes in the $512 \times 256 \times 256$ matrix size and a $32 \times 17 \times 17$ mm^3 field-of-view. These details are extracted as it is from the previously published work by Chang et al. (2015).

The MRI scans are then used for manual segmentation using the open-source software ITK-SNAP. This allows us to construct the tissue and the three major cartilages viz. thyroid, cricoid, and arytenoid as shown in Figure 3.1. The MRI scans used for evoked phonation in the current chapter, are processed for smoothening operation using the Gaussian image tool, and the tetrahedral mesh is achieved by using ANSYS ICEM. The thin cover of the vocal fold was determined roughly based on its thickness identified from the MRI. A mesh-refinement test with a static load and finer mesh near the vocal fold cover resulted in an error of only 1.58%. This mesh model was used as the finite-element model of the vocal fold tissue. The 3D model was then processed in MATLAB to extract the lumen as the

flow domain, which was then extended in both subglottal and supraglottal directions to incorporate the inlet and exit flow through the larynx. The entire process is shown in Figure 2, where the vocal fold is seen to surround the flow domain except for the inlet and outlet extensions.

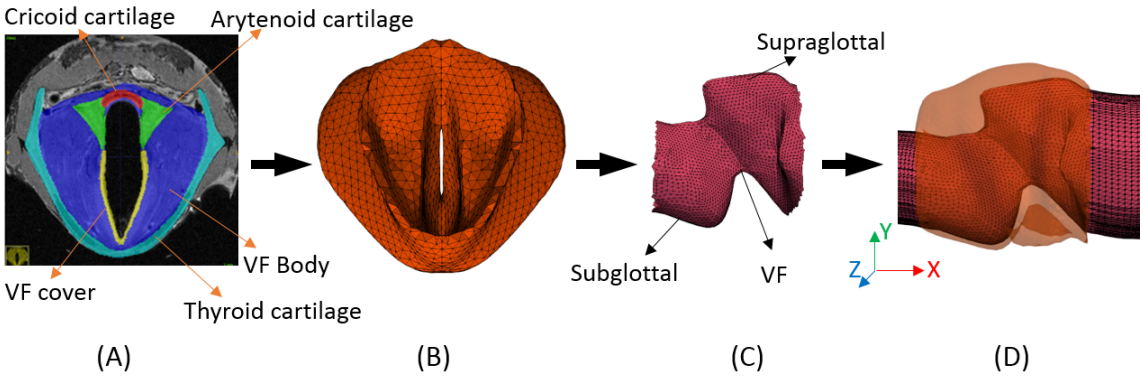

Figure 3.1: (A) Manual segmentation of the MRI data for the vocal fold (VF). (B) Reconstructed 3D VF mesh model. (C) Extracted lumen from the 3D larynx. (D) Extensions added in both directions as the flow domain (only a small portion of inlet and outlet are shown).

All five larynx samples have distinct geometries, which are shown in Figure 3.2 for comparison. Table 3.1 lists the total number of tetrahedral elements in each vocal fold. The finite-element model has all the exterior surfaces with the fixed boundary condition, whereas the lumen surface from the inside has a free boundary subject to the forces from the fluid. The vocal fold tissue is considered isotropic and described by the Saint Venant-Kirchhoff model, which includes the finite strain for possible large displacements and rotation (Tian et al., 2014; Chang et al., 2013). For each sample, Chang et al. (2015) used an iterative method to determine the stiffness properties for the vocal fold body and lamina propria. That is, Young's moduli were determined by matching the vibration frequency and amplitude between the 1D-flow-based FSI simulation result and the phonation experiment. The tissue density and Poisson's ratio are $\rho_s = 1000$ kg/m^3 and 0.3 respectively. The air density is at $\rho = 1.0$ kg/m^3, and the air viscosity is increased by four times to reduce the Reynolds number and the demand for the simulation.

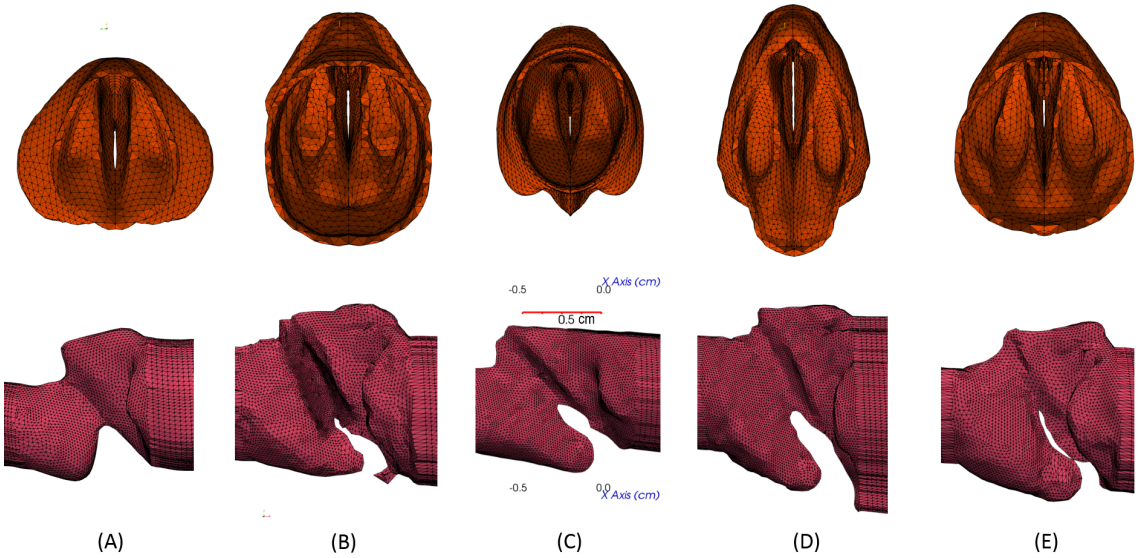

Figure 3.2: Top row: the reconstructed larynx models for all samples as viewed from the supraglottal side for samples 1 to 5 in [A-E] respectively; bottom row: the corresponding extracted lumen. A scale of 0.5 cm is shown in (**c**).

Table 3.1: Number of tetrahedral elements in the finite-element model of the vocal fold.

Sample	**1**	**2**	**3**	**4**	**5**
Elements	40,394	63,070	84,368	101,166	81,386

3.2.1 Phonation experiments

The experiments were conducted on five male New Zealand white breeder rabbits under the approval of the Vanderbilt University Institutional Animal Care and Use Committee. Readers can refer to Novaleski et al. (2016), Ge et al. (2009), and Swanson et al. (2010) for detailed experimentation procedures and objectives. A bilateral Isshiki-type IV thyroplasty was performed, involving suturing of thyroid and cricoid cartilages to bring together the two sides of the vocal fold. This procedure enables *in vivo* rabbit phonation when a continuous humidified airflow is delivered through the glottis. A high-speed camera recorded the supraglottal view of vocal fold vibration at 10,000 frames-per-second (FPS). During

this process, subglottal pressure and flow rate were also recorded. Figure 3.3 shows images of the glottis from the high-speed camera for each larynx sample.

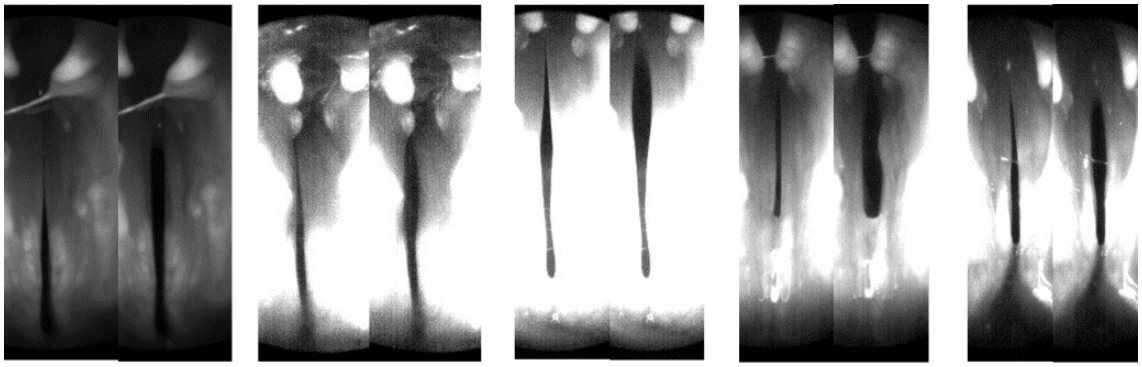

Figure 3.3: Images of the glottis during phonation (supraglottal view) from the high-speed camera for the five samples 1 to 5 in (**a-e**) respectively. The left image for every sample represents the vocal fold closure, and the right side represents the vocal fold opening.

3.2.2 Simulation setup and mesh refinement study

The flow domain in the 3D FSI is discretized using a non-uniform Cartesian grid, on which the mesh is stretched in the lateral (Z coordinate in Figure 2.1) direction so that it is finest in the glottis. For each sample, the mesh is approximately 200 in the axial direction, 130 in the lateral direction, and 130 in the anterior-posterior direction. The rectangular flow domain is decomposed into multiple subdomains to facilitate the parallel processing of the simulation. We have used approximately 65 to 133 processors for each sample, and the simulations were performed on Stampede2 at the Texas Advanced Computing Center (TACC). The time step used was $\Delta t = 10^{-4}$ centisecond to achieve good temporal resolution and ensure FSI stability, which leads to approximately 3000 time steps to resolve one vibration cycle.

The subglottal pressure is set to be constant and the same as in the phonation experiment, and the exit gage pressure is set to be zero. Each sample has a different inlet gage pressure, as shown in Table 3.2. In addition, Young's modulus of the vocal fold body E_b and for the cover E_c are given in Table 3.2. These parameters are used exactly as in the

Table 3.2: Inlet pressure (gage) in the experiments and Young's modulus for the vocal fold body, E_b, and for the vocal fold cover, E_c, which were previously determined for each individual samples Chang et al. (2015).

Sample	1	2	3	4	5
Pressure (kPa)	1.05	0.78	0.72	1.0	0.98
E_b (kPa)	60	80	80	90	90
E_c (kPa)	12	8	8	9	9

previous study on the 1D flow-based FSI analysis by Chang et al. (2015). In both the 3D FSI and 1D-flow-based FSI simulations, the flow is driven by the subglottal pressure, and the pulsatile flow is established automatically once the vocal fold vibration is induced in the process.

A mesh-independence study for Sample 3 is shown in the Fig. 3.4 with the baseline mesh for the flow formed by a non-uniform Cartesian grid with $211 \times 129 \times 133$ points and the refined mesh with $371 \times 154 \times 144$ points in the X, Y, and Z coordinates. The displacement of a point at the mid-glottis is used to compare between the two mesh settings. In addition, the pressure along the streamline in Fig. 3.9(a) is compared between the two FSI simulations at $t = 0.6$ cs when the VF is fully opened. In both the displacement and the intraglottal pressure comparisons, the baseline-mesh result agrees well with the result from the refined mesh. The mean error in the pressure value between the two meshes is 4%.

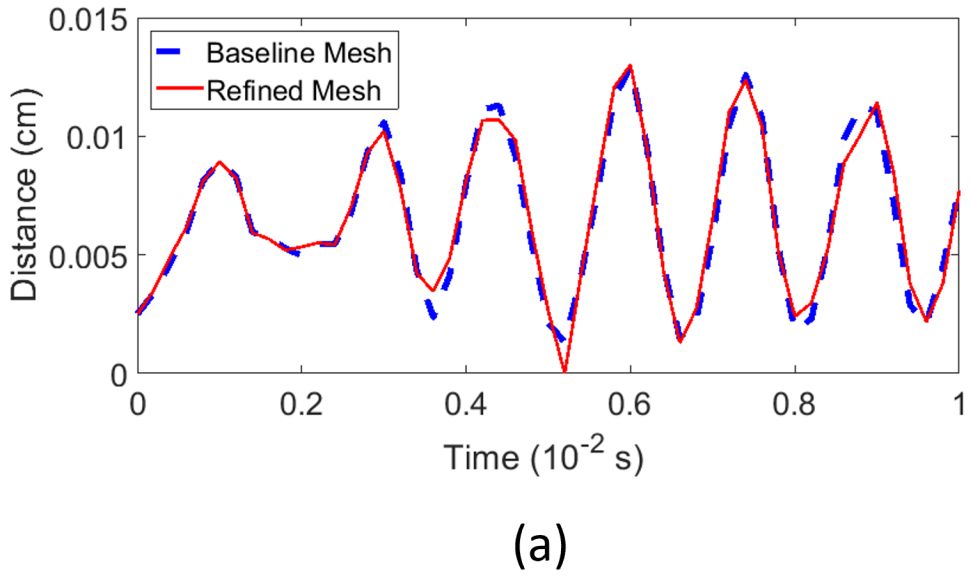

(a)

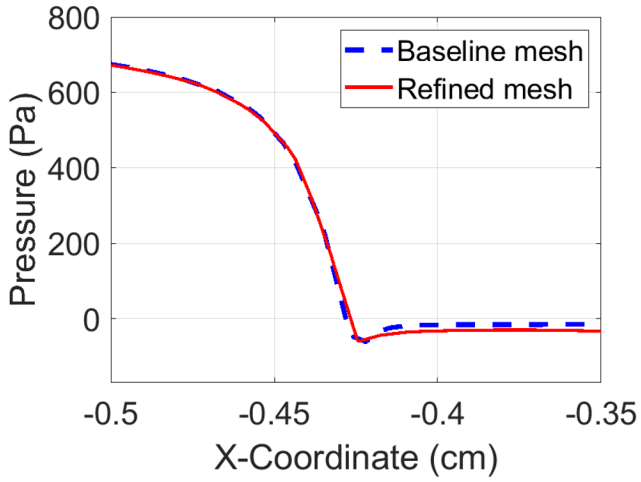

(b)

Figure 3.4: (a) vocal fold displacement; (b) intraglottal pressure plot at $t = 0.6$ cs for the baseline and refined meshes (Sample 3).

3.3 Results and discussions

3.3.1 Vocal fold vibration

The vocal fold vibrations were observed to be fairly symmetric between the left and right sides in the experiments. Thus, a marker point on one of the sides of the vocal fold around

the halfway between the anterior and the posterior of the glottis is chosen from the output to reflect the vibration amplitude. Figure 3.5a shows the vibration for this point for Sample 3. For comparison, we have included both the 3D FSI simulation result and 1D-flow-based FSI result from our previous work (Li et al., 2021a). Within the time frame of 1 centisecond (cs), approximately five to six vibration cycles are clearly visible for the sample. The vibration waveform agrees well with the two FSI models.

Some differences in the vibration amplitude and the phase between the two FSI models can be seen and are understandable since the accurate characteristics of vibration are dependent on the detail of the flow that is captured only in the 3D simulation. Indeed, it has been shown previously by Luo et al. (2012) that the fluid forces on the vocal fold could be fluctuating due to the vortices in the flow. For all the samples, the vibrations are established when simulations are extended. We have calculated the vibration frequency exhibited by each sample using the Fast Fourier Transform (FFT) and compared the result with the previously published data from the experiments and 1D-flow FSI simulation, as shown in Figure 3.5b. We see a good agreement between the frequencies reported from the experiments, the 1D-flow FSI model, and the current 3D FSI model. Note that the vibration frequencies for all five samples are in the range of generic vibration frequencies for rabbits from experiments by other groups (Döllinger et al., 2018).

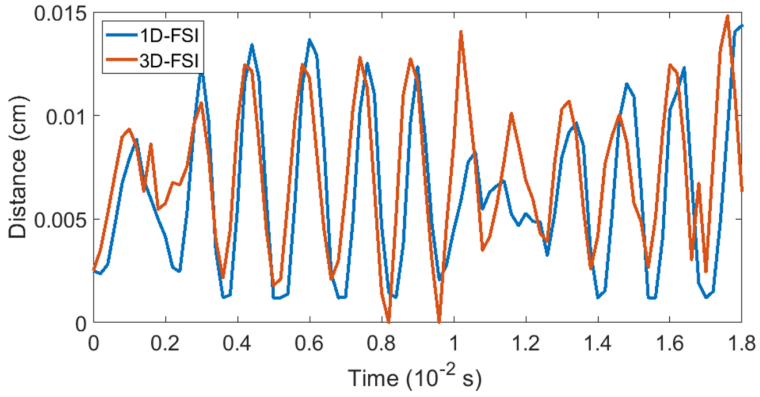

(a)

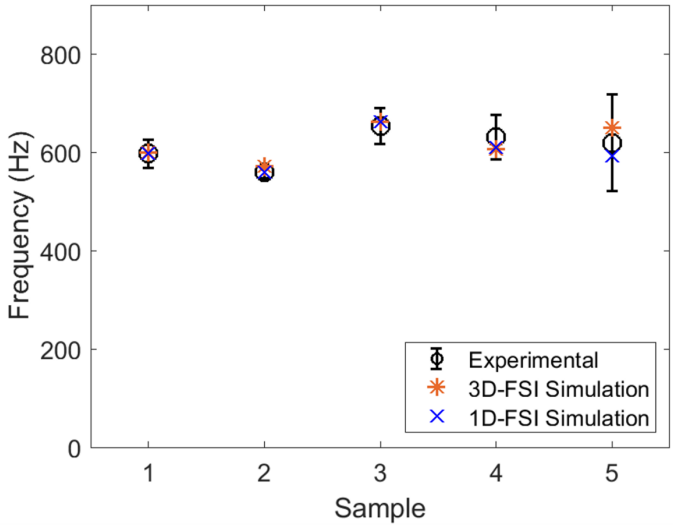

(b)

Figure 3.5: (a) VF vibration for Sample 3 plotted for the mid-glottis point in both 1D FSI model (blue line) (Chang et al., 2015) and 3D FSI model (orange line). (b) VF vibration frequency comparison of all five samples among the experiments, 1D-FSI and 3D-FSI simulations.

3.3.2 Power and energy analysis

In our numerical study, the flow is driven by a constant subglottal pressure at the inlet, which acts as the source of energy for the phonation process. In addition to providing kinetic energy to the flow, part of the energy source is transferred to the vocal fold tissue through the stresses on the vocal fold surface and the tissue's dynamic deformation. To

calculate the power transfer or rate of work, $\dot{E}$, from the flow to the tissue, we integrate the product of the fluid stress, $\mathbf{f}$, which includes the shear and normal stresses, and the velocity of the vocal fold surface, $\mathbf{v}$, so that $\dot{E} = \int \mathbf{f} \cdot \mathbf{v} dS$, where S is the vocal fold surface.

Figure 3.6 shows the work rate $\dot{E}$ along with the corresponding vocal fold vibration cycles for Sample 3. In the plot, we notice that the first opening phase (from stationary) consumes the maximum amount of power and then the instantaneous work rate oscillates between positive and negative values. The accumulated work E is also shown as a reference. From the figure, the first cycle shows a relatively large amount of work being transferred to the tissue, representing the initial opening of the vocal fold. Then, both $\dot{E}$ and E start to oscillate around their mean values, indicating the elastic recoil of the tissue structure. The average of $\dot{E}$ is small since the tissue is elastic and only a small amount of damping is added to the tissue. Further, inspection shows that $\dot{E}$ is neither exactly in phase nor out of phase with the vibration.

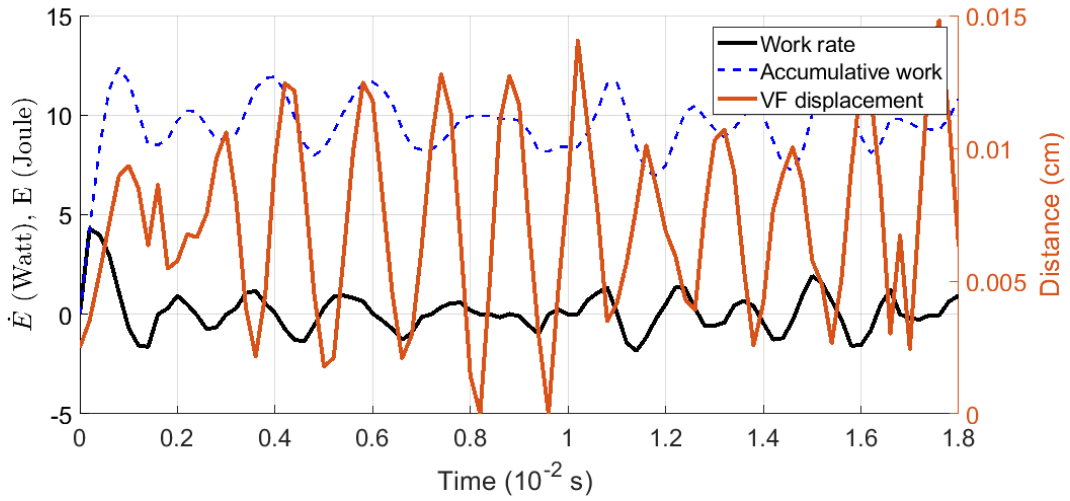

Figure 3.6: Rate of work, accumulative work, and VF vibration for Sample 3.

To better understand the energy transfer and the vocal fold vibration, in Figure 3.7 we plot the instantaneous pressure and velocity contours along with the contours of the power per unit area, $\mathbf{f} \cdot \mathbf{v}$, over the vocal fold surface at times $t = 1.5$ cs and $t = 1.6$ cs. As seen from Figure 3.6, $\dot{E}$ is positive at $t = 1.5$ cs when the vocal fold is closing and is negative at $t = 1.6$

when the vocal fold is near the maximum opening. The power contours in Figure 3.7 show that most of the work is contributed by the sub-glottal surface for both time frames. Note from the inset in this figure that the vocal fold has a gentle slope and thus a large surface area subject to the pressure force. The corresponding pressure contours in Figure 3.7 show that the surface pressure is predominantly positive in the inferior region (prior to the glottal gap), and the glottal gap the pressure level is rapidly reduced. This pressure distribution also facilitates most of the energy transfer through the inferior slope while this area of the surface is deforming. Furthermore, since the pressure is positive at the inferior region, the sign of power contours is consistent with the sign of the lateral velocity of the vocal fold surface, w, as seen in Figure 3.7.

The insets in Figure 3.7 further show the instantaneous deformations of the vocal fold in an XZ cut plane at these two time moments. At $t = 1.5$ cs, the the glottis is closing but the inferior region is expanding quickly, leading to an overall positive rate of work; while at $t = 1.6$ cs, the inferior region is contracting quickly even though the glottis is nearly fully open, which leads to overall a negative rate of work. The velocity vectors in the insets indicate that the inferior region movement has a phase difference from the glottis opening/closing. As a result, the rate of work also has a corresponding phase difference from the glottal vibration, as seen in Figure 3.6. Similar inferior geometry and pattern of the surface power distribution are also observed for the other samples. Therefore, from these results, we learn that the region has an important impact on the energy transfer of the rabbit vocal fold vibration. The effect of the inferior surface slope on the vocal fold vibration and energy transfer was discussed in previous work using idealized geometries (Smith and Thomson, 2012). The present finding of the rabbit phonation regarding the inferior surface is consistent with the conclusion in that work. This chapter carries the material as it is from recent publication (Avhad et al., 2022)

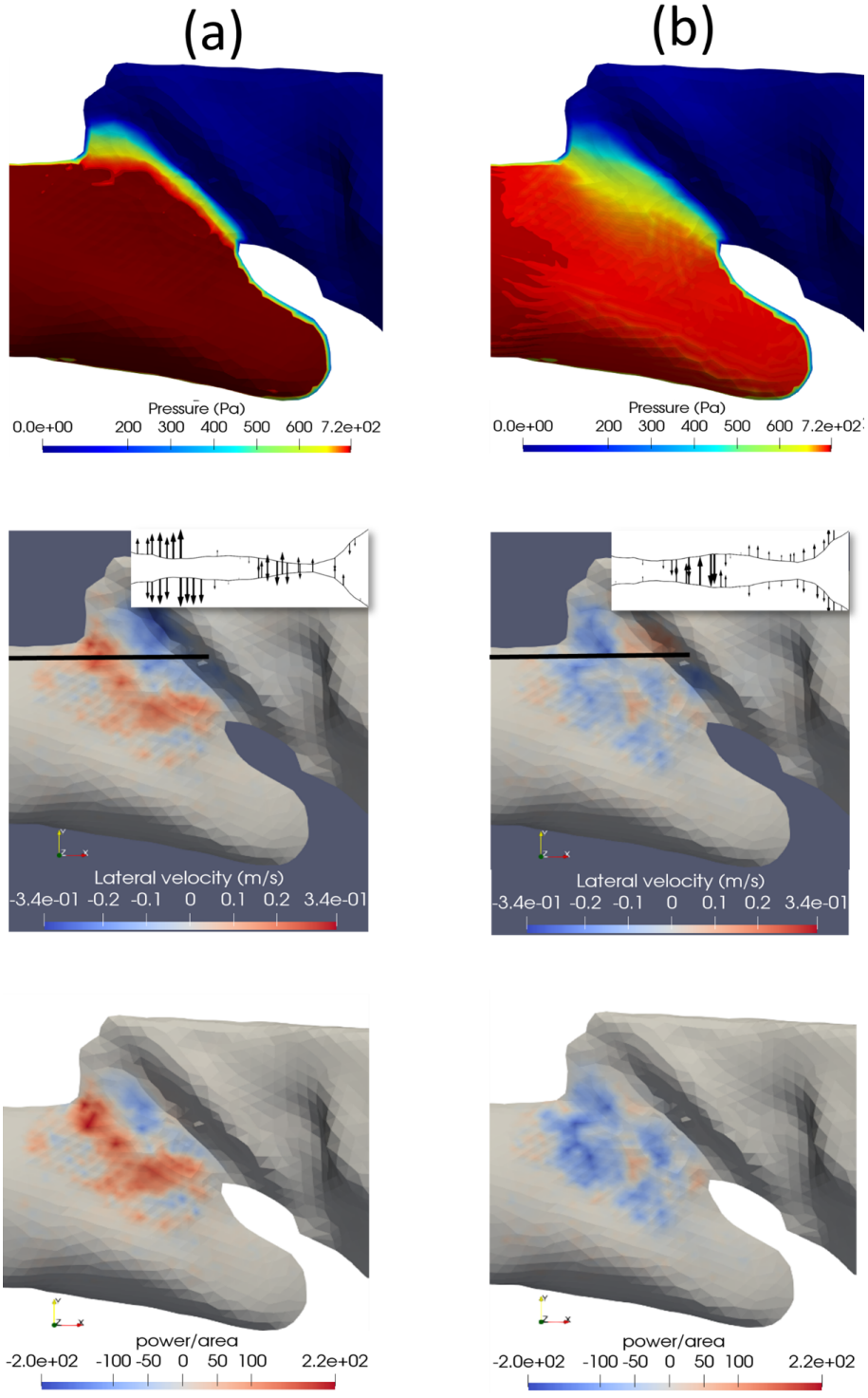

Figure 3.7: Contours on the vocal fold surface for Sample 3 at (a) $t = 1.5$ cs (VF closed) and (b) $t = 1.6$ cs (VF open). Top to bottom: pressure contour, lateral velocity w, power per unit area on the vocal fold surface. The inset on the center picture shows the vocal fold profile and the velocity vectors in the cut plane indicated by the thick bar in the picture.

In addition to the energy transfer from the fluid to the tissue, it is also important to examine the loss of mechanical energy, which can be evaluated using the total gage pressure along the flow, defined as $p_{total} = p + 0.5\rho V^2$. Note that this definition is the sum of static pressure and dynamic pressure and is measured using gage pressure here. So, it is different from the definition of the total pressure for gas mixtures (usually measured as absolute pressure).

Since the rabbit vocal fold, as seen in Figure 3.7, has a long, gradually converging inferior channel but a short and quickly diverging superior channel, it is expected that flow separation could be strong and the loss of total pressure is significant in the supraglottal area. To see this, from the 3D flow field we extract a streamline that goes through the glottis as seen in Figure 3.8(a) and (c) for Sample 3 at time $t = 0.6$ cs when the vocal fold is open and at $t = 0.66$ cs when the vocal fold is closed. The pressure and the velocity magnitude V along this streamline are plotted in Figure 3.8 (b) and (d).

It can be seen from Figure 3.8(b), where the vocal fold is open, that the total pressure drops quickly from the glottis to the supraglottal region. Before the glottis, the total pressure is well preserved. The peak velocity magnitude on the streamline in this figure is 32 m/s around $x = -0.48$ cm, which is inside the glottal gap. At the same position, the pressure drops to the minimum value, $p = -75$ Pa. According to Bernoulli's equation, the maximum flow speed should be at $V \approx 39$ m/s, using the inlet pressure $P_{in} = 0.72$ kPa and air density $\rho = 1.0$ kg/m^3, which is close to the simulated value considering the viscous effect. In addition to the large expansion ratio from the thin glottal gap to the wide supraglottal region, another factor that could have affected the total pressure loss in the supraglottal region is that the overall shape of the lumen is curved and the flow impinges on the anterior wall in the supraglottal region. This feature may have caused additional losses in the flow.

When the vocal fold is closed, as in Figure 3.8(d), the flow velocity is low, and the total gage pressure follows the pressure and quickly drops to nearly zero when reaching the

glottis. This result is expected since the flow is nearly shut off and the supraglottal region is dominated by large flow circulation as seen later in the 3D visualization. The total pressure of the remnant flow is nearly all lost after exiting the glottis.

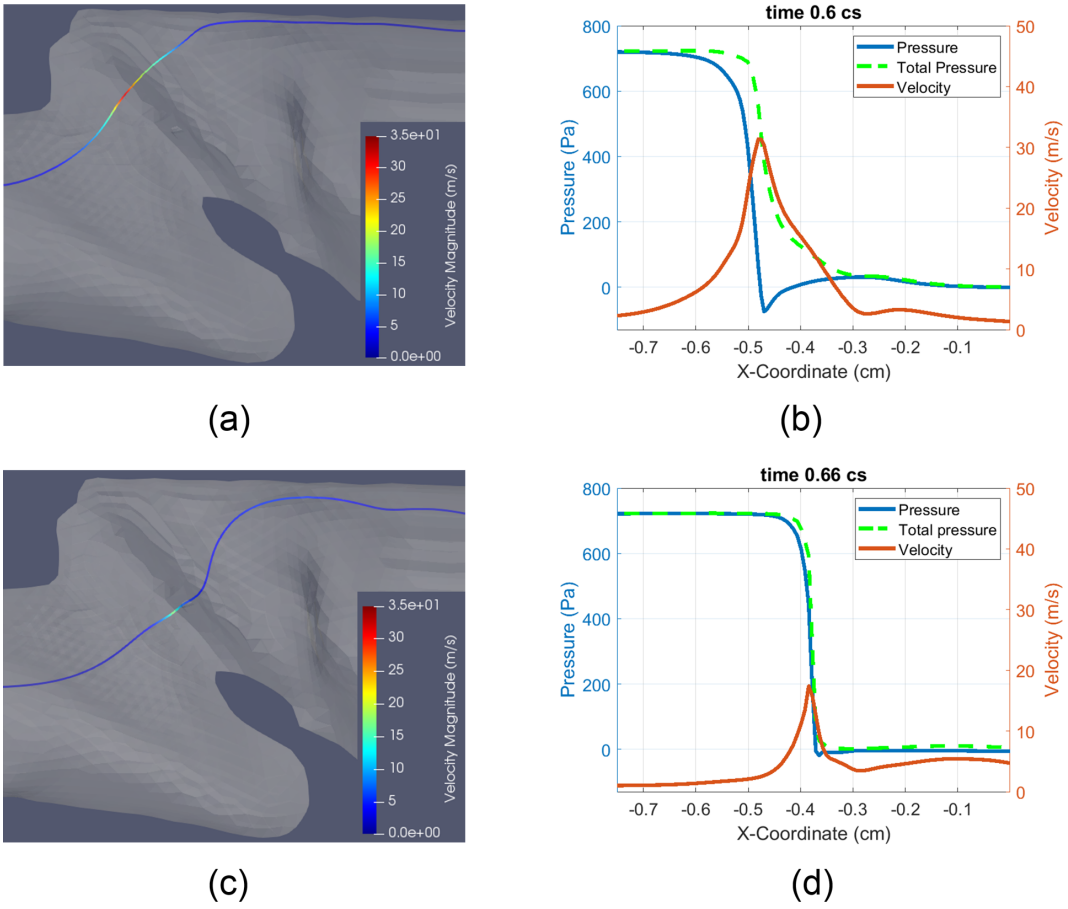

Figure 3.8: Change of the total gage pressure along a streamline at open or closed state for Sample 3. (a) A streamline at open state with t = 0.6 cs, and (b) the plots for p, V, and p_{total} along this streamline; (c) A streamline at closed state with t = 0.66 cs, and (d) plots for p, V, and p_{total} along this streamline.

3.3.3 Pressure comparison between 1D and 3D FSI

The comparison of the vocal fold vibration in previous section shows that the 1D-flow-based FSI produces a consistent vibration pattern of the vocal fold as in the current 3D FSI simulation. To further examine the performance of this general 1D flow model, we compare the intraglottal pressure predicated by the 1D flow model with that extracted from the 3D

flow field. To the comparison, we first extract a streamline through the glottis, as shown in Figure 3.9(a) for an opening or closing state. The arc length of this streamline is used as the x-coordinate in the 1D flow model in Equation The sequence of the dynamic vocal fold shapes from the 3D FSI simulation is used to calculate the cross-sectional area in the 1D flow model, which is subject to correction due to the entrance effect (Li et al., 2021a). The 1D flow model, which includes its machine learning derived functions for the pressure loss and entrance effect, is then used to calculate the pressure along the same streamline.

Figure 3.9(b) and (c) show the comparison of the flow pressure between the 3D FSI simulation and the 1D flow model. In Figure 3.9(b), the time is $t = 0.6$ cs, and the vocal fold is open; in Figure 3.9(c), the time is $t = 0.66$ cs, and the vocal fold is closed. In both of these cases, it can be seen that the 1D flow-based pressure calculation generally agrees with the pressure from the 3D simulation. Further inspection shows that at the open state, the 1D flow model slightly under-predicts the pressure prior to the narrowest gap; at the closed state, the difference is more pronounced, and the 1D flow shows lower pressure in the inferior region and some negative pressure in the glottal gap. Fortunately, such a difference did not significantly impact the vocal fold vibration during the 1D flow-based FSI simulation since the closed state is quite short in a vibration cycle.

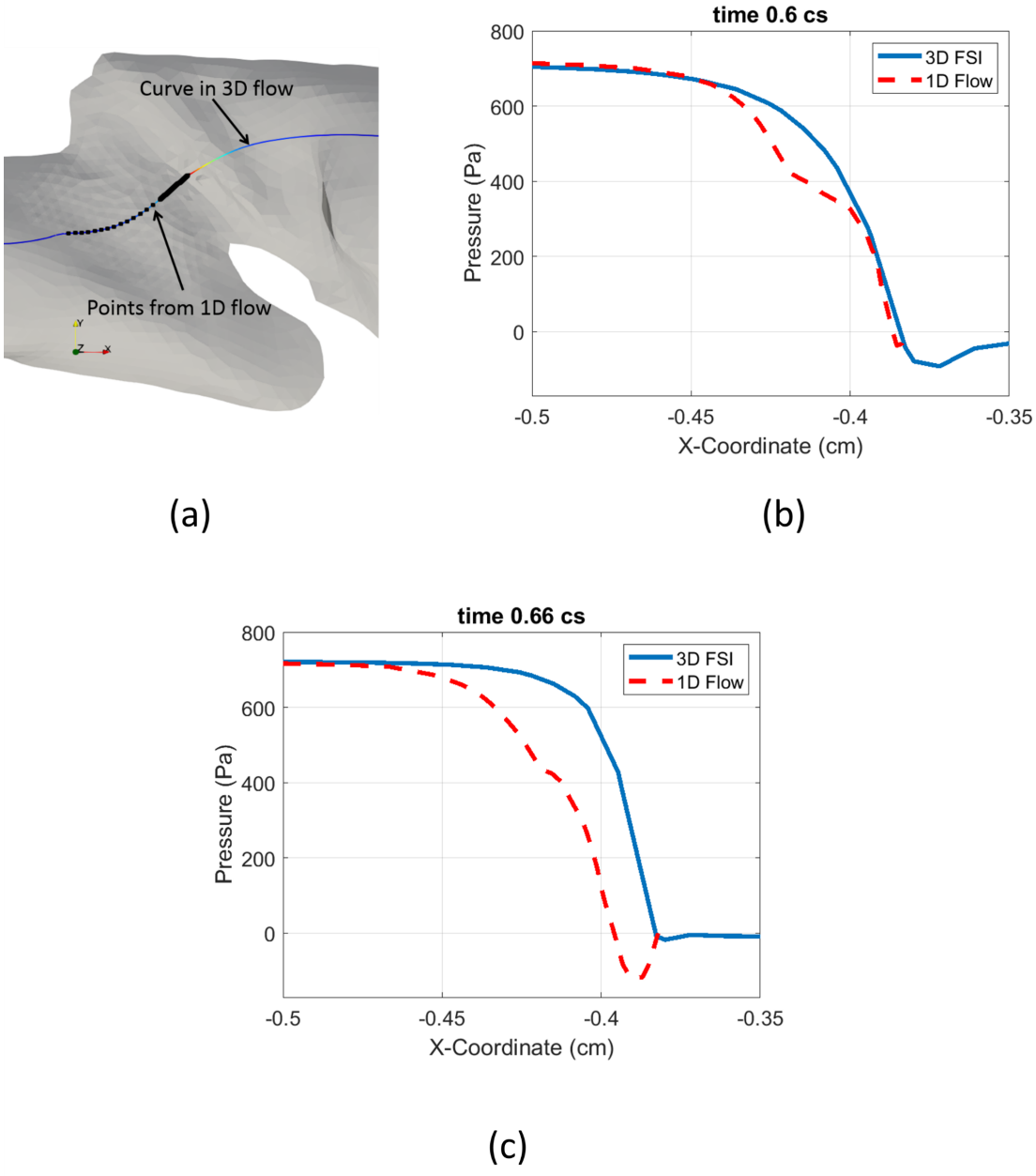

Figure 3.9: (a) Sample 3 model showing a streamline and the points (black markers) on it, along with the 1D flow model applied. (b) and (c) Gage pressure plot on the points from the 1D flow model (dashed) and 3D FSI model at an open state ($t = 0.6$ cs) (b) and closed state ($t = 0.66$ cs) (c).

3.3.4 Flow field analysis

One of the major objectives of this study is to visualize and analyze the 3D flow in rabbit phonation. This was not done previously in Chang et al. (2015), who focused mainly on

the reduced-order modeling for the FSI. There has been limited research that employed subject-specific larynx models in the 3D FSI analysis. A few previous experimental (Triep et al., 2005; Khosla et al., 2008) have found that in general the downstream flow in the supraglottal region is highly 3D. In the numerical study by Xue et al. (2014), it was found that significant asymmetry in the flow exists in the supraglottal region for the subject-specific human larynx model.

Figure 3.10 shows several time snapshots from $t = 0.56$ to 0.66 cs, representing vocal fold opening, fully open, closing, and fully closed, respectively. An important observation is that since the flow tends to follow the generally reversed Z-shaped geometry of the larynx, the majority of the flow is directed toward the anterior side after exiting the glottis. This skewed direction forms the major cause for the flow asymmetry in the supraglottal region. Fortunately, the vocal fold has an inclined orientation with respect to the larynx and remains approximately perpendicular to the flow direction. This alignment facilitates the interaction between the vocal fold and the flow and is beneficial to the flow-induced vibration. The inclination angle θ is illustrated in Figure 3.10, and Table 3.3 lists the value of θ, which is between 20 and 45 degrees for all five samples.

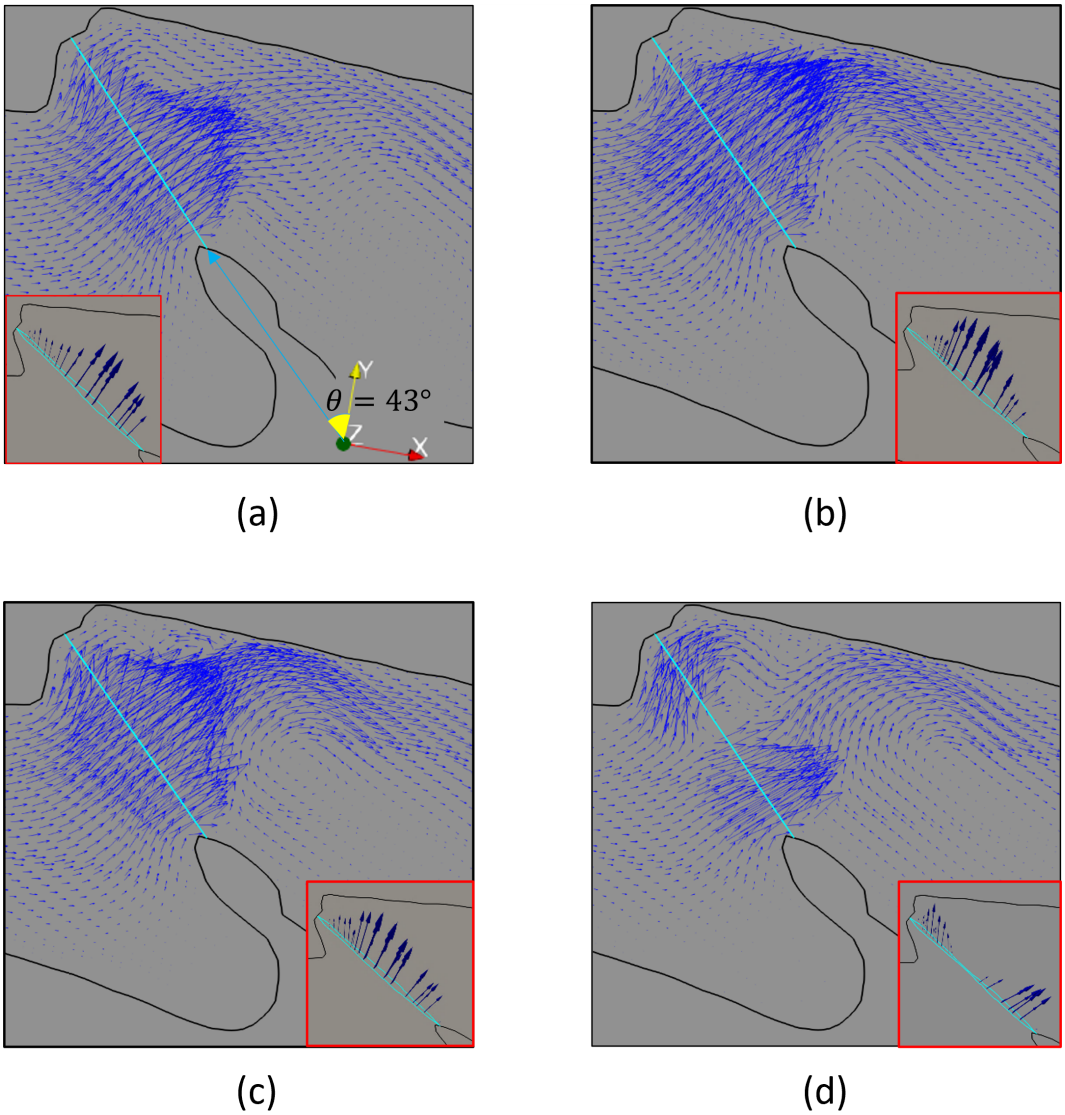

Figure 3.10: Time sequence of flow for Sample 3. a-d: $t = 0.56$, 0.6, 0.64, and 0.66 cs. Inset figures show the corresponding glottal shape along with the velocity vectors through the glottis.

Due to the flow skewness, a large circulation persists on the posterior side of the supraglottal region throughout the vibration cycle, and this major vortex is strengthened as the flow speed increases following the vocal fold opening. On the other hand, a much smaller vortex may develop at the anterior side, e.g., at $t = 0.62$ cs when the vocal fold is closing. This vortex is due to the closure of the anterior side of the glottis while the posterior side remains open (the posterior side of the vocal fold has minimal displacement and does

not close completely), allowing the flow to continue going through. Such a vortex pair is repetitively observed at the start of vocal fold closure during each cycle.

Table 3.3: VF inclination angle θ from the transverse axis (Y-axis).

Sample	**1**	**2**	**3**	**4**	**5**
θ (degrees)	41	24	43	20	29

In addition to Sample 3, we also have a similar observation for the other four samples, which are shown in Figure 3.11. In this figure, we see the notable geometry differences among the samples, especially in the alignment of the subglottal and supraglottal channels. The anterior-end vortex in the supraglottal region is prominent in Samples 1, 2, and 4 due to a protruded space in the region. In all the five samples, the large posterior-end vortex is distinctly identified. This flow feature is caused by the overall orientation of the subglottal-supraglottal channels and the inclination of the vocal fold. Such anterior-posterior flow asymmetry was also reported in a subject-specific computational analysis of the human larynx due to the similar geometric asymmetry (Xue et al., 2014), and it was believed that the flow asymmetry produced the anterior-posterior (longitudinal) asymmetry in the vocal fold vibration. In our study, we also observed longitudinal asymmetry in the vibration. However, there may be additional factors that have caused this behavior, for example, varying shapes of the vocal fold tissue structure in the transverse plane along the longitudinal direction, well as differences in the cartilages that the vocal fold is attached to at the anterior and posterior ends. Further study may be needed to better understand the longitudinal differences in the vibration.

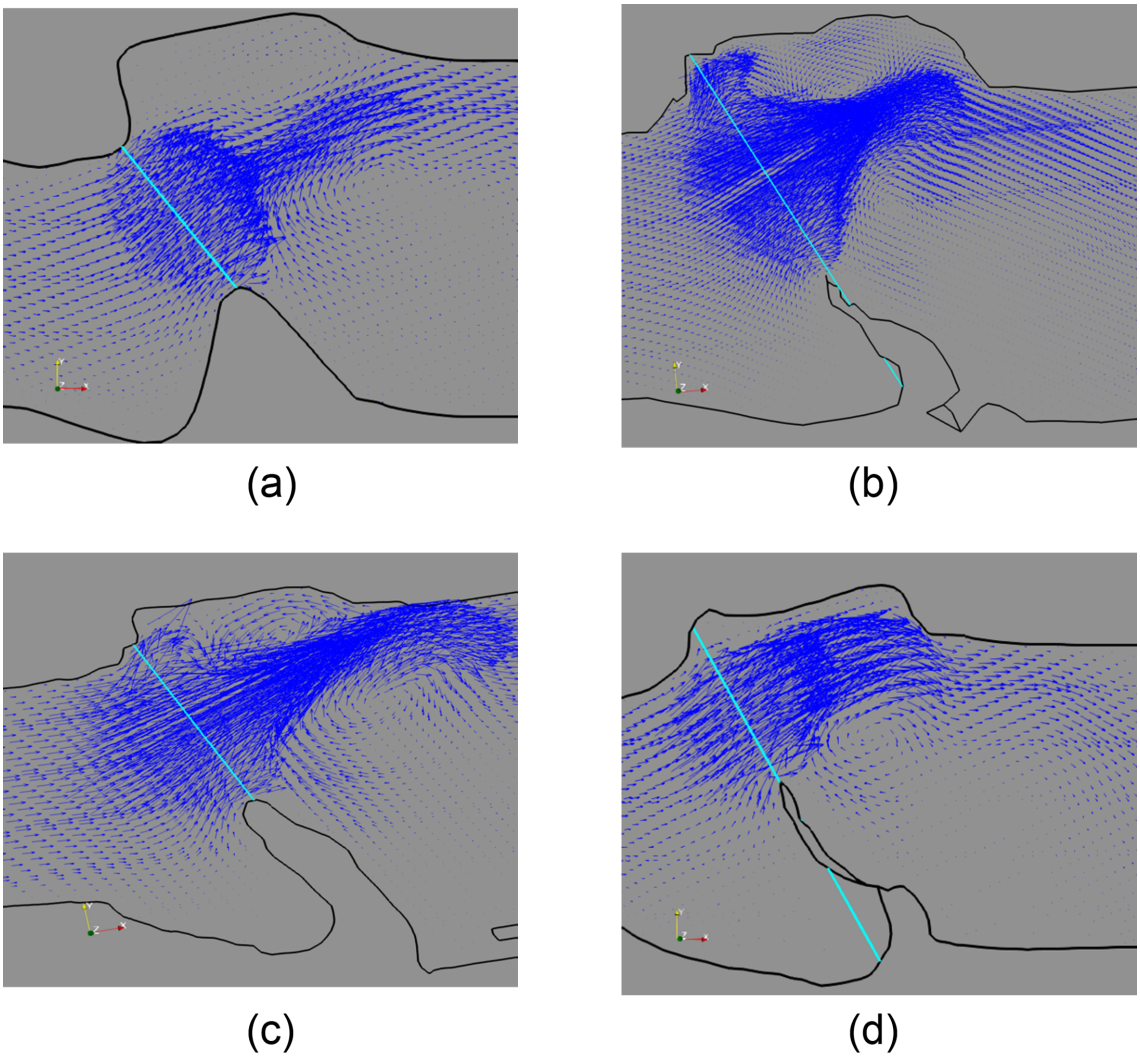

Figure 3.11: Flow pattern in the supraglottal region and the anterior, posterior vortices in Samples 1, 2, 4, and 5 in (a), (b), (), and (d) respectively. The vocal fold is at an open state.

There have been extensive discussions on the supraglottal flow jet symmetry in the lateral direction. Previously, studies conducted both numerically and experimentally have reported varying asymmetrical glottal jet in the lateral direction when using simplified larynx models (Tao et al., 2007; Luo et al., 2008; Zheng et al., 2009, 2011; Xue et al., 2012), and the phenomenon was explained using the bifurcation of the confined jet in a large expansion (Luo et al., 2008). It was found that the presence of the false vocal fold helps reduce the expansion ratio of the geometry and maintain the symmetry of the flow (Luo et al., 2009; Zheng et al., 2009). The subject-specific 3D FSI study by Xue et al. (2014)

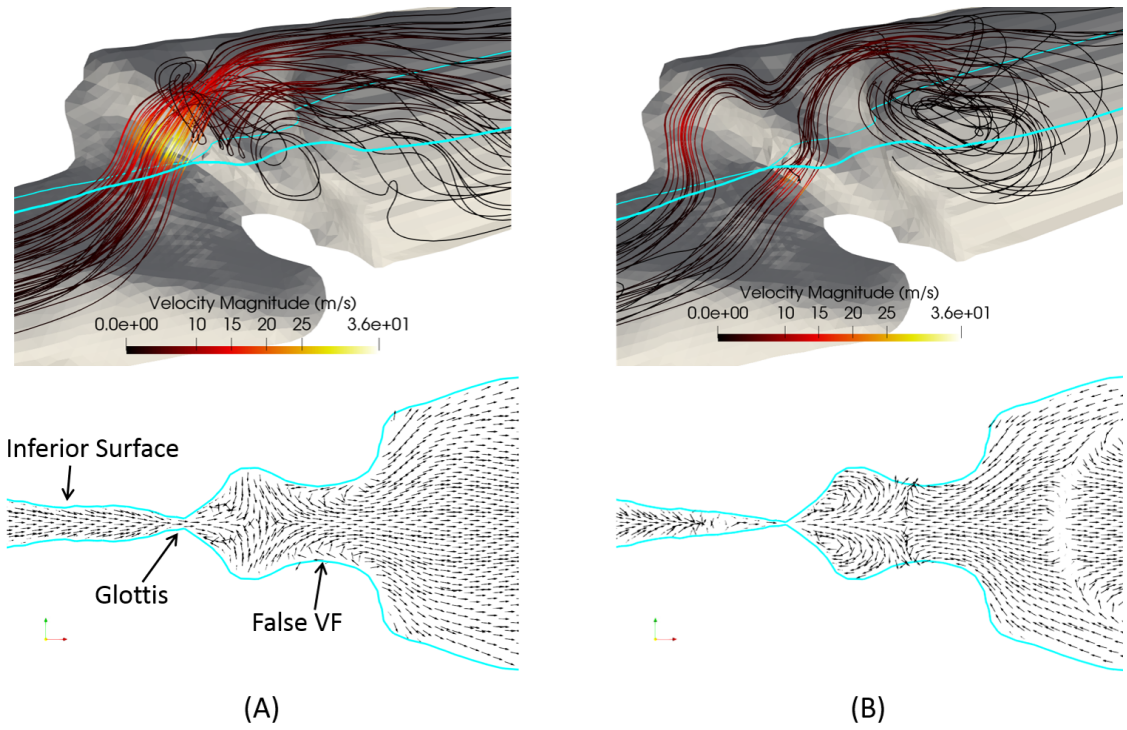

Figure 3.12: 3D flow pattern in Sample 3 at (a) vocal fold opening ($t = 0.6$ cs) and (b) vocal fold closing ($t = 0.66$ cs). Bottom row: corresponding velocity field in the cut plane (blue lines) shown in the top row.

observed a fairly symmetrical jet flow in the lateral direction during most of the vibration cycle, which is consistent with the effect of the false vocal fold. In the current study, we report a symmetrical downstream flow pattern in the lateral direction, owing majorly to similar geometrical factors. In Figure 3.12, a 3D view of the flow is shown at $t = 0.6$ cs (open) and $t = 0.66$ cs (closed) stages, respectively. For each 3D view, a YZ cut plane is made, in which the velocity vectors downstream the vocal fold are shown. These pictures show the lateral symmetry of the flow domain and the presence of the false vocal fold helps maintain the flow symmetry in the lateral direction.

At the open condition (Figure 3.12(A)), we see that some of the flow is reversed in the ventricle region before the false vocal fold, which is due to the circulation of two lateral vortices in that region. Further downstream, a fairly uniform and symmetric outgoing flow is formed. At the closed condition (Figure 3.12(B)), we see in the cut plane that the two

lateral vortices are still present in the ventricle region. Between the false vocal fold and immediately downstream, there is significant reversal flow due to the large posterior-end vortex. Despite the strong asymmetry in the anterior-posterior direction that was discussed early, the flow is able to retain symmetry in the lateral direction.

The 3D characteristic flow patterns observed here have significant similarities to those from human phonation, e.g., the anterior-posterior asymmetry and the lateral symmetry. This finding has important implications. Our current efforts are focused on the study of vocal fold vibration in unilateral vocal fold paralysis (UVFP) as well as in the implanted configuration that aims to improve the implant design for individual subjects. The rabbit and its evoked phonation are being used in such efforts before similar studies can be done on human subjects. One important consideration in the UVFP and implant study is the restoration of symmetric vibration between the left and right sides of the vocal fold and the lateral symmetry in the flow. The present findings from the 3D analyses would help support the use of the rabbit as an intermediate step toward a human study.

3.4 Chapter conclusions

Full 3D FSI simulations have been performed on the five subject-specific samples of the rabbit larynx, which were previously used for *in vivo* phonation experiments and a 1D-flow-based FSI study. These samples vary in size, geometry, and tissue properties, and are subjected to different inlet flow pressure during evoked phonation. Through the simulation, we obtained detailed vibration characteristics and 3D flow patterns. The simulation-predicted vibration agrees with the experiment result for each individual subject. Furthermore, both the vocal fold displacement and intraglottal pressure agree with those from the 1D-flow model based simulation.

In the present rabbit phonation study, it was found that the gentle-slope inferior surface of the vocal fold plays a major role in the energy transfer between the fluid to the vocal fold tissue during vibration. For the flow field, we found that the flow in the supraglottal

region is significantly skewed to the anterior side due to the asymmetrical geometry of the larynx and the inclination of the vocal fold with respect to the axis of the larynx. However, the flow is fairly symmetric in the lateral direction thanks to the presence of the false vocal fold, which limits the expansion ratio of the geometry for the flow exiting the glottis. Such 3D flow patterns are generally consistent with those found previously in subject-specific modeling of healthy human phonation. Therefore, the use of rabbits may provide helpful insight into the study of human phonation.

CHAPTER 4

Computational modeling of Unilateral Vocal Fold Paralysis (UVFP) and type-1 thyroplasty

4.1 Introduction

In the past, computational modeling of phonation has largely contributed to the understanding of its physical process and provided insights into various aspects such as vibratory characteristics, geometric and material parameters, and acoustic output (Xue et al., 2014; Avhad et al., 2022; Movahhedi et al., 2021; Li et al., 2021b; Wu and Zhang, 2023; Cameron et al., 2020) that were not available from experiments (Luo et al., 2009). Earlier computational FSI studies using much simplified or idealized structural models of the larynx were able to simulate generic vibratory characteristics of the VF (Alipour et al., 2000; Thomson et al., 2005; Zörner et al., 2013; Tao et al., 2007; Yang et al., 2018). Recently, several studies have started to employ more realistic laryngeal models that were based on magnetic resonance imaging (MRI) or computerized tomography (CT) scans of individual subjects (Xue et al., 2014; Avhad et al., 2022). With the subject-specific anatomical details incorporated, such computational models may potentially be used to evaluate the effect of the implant on vocal fold vibration prior to the operation, thus serving as a planning tool to improve the surgical outcome.

Along with this line of research, in recent years our lab has performed a series of integrated studies combining rabbit vocal fold experiments and computational models to explore issues such as experiment protocol, model construction, computational efficiency and accuracy, model validation, and outcome assessment. For example, Chang et al. (2015) modeled and validated the healthy phonation condition that was created in vivo in rabbits; Li et al. (2020) developed a simplified 1D pulsatile flow model that was enhanced by machine learning and also validated it against the same set of in vivo phonation data; Wilson

et al. (2021) created different vocal fold configurations in rabbits including bilateral medialization, UVFP, and type-1 thyroplasty; and Li et al. (2023) used a computational model to optimize the implant location for type 1 thyroplasty, and through a controlled experiment, they demonstrated the computational modeling and optimization led to improvement in implant medialization. The use of rabbit models in investigating phonation and voice disorders is justified due to their similarities in anatomical, biological, and biomechanical vocal fold properties with those in the human larynx (Thibeault et al., 2002; Ge et al., 2009; Döllinger et al., 2018).

Despite the recent progress in the subject-specific modeling of vocal fold vibration and the efforts in the modeling of thyroplasty, there is still a lack of work in combining computational modeling with experiments to validate the model and to assess the models' performance in capturing the effect of the implant on the VF's vibratory characteristics. There have been a few recent works that used computational modeling to investigate implant medialization. For example, Smith et al. (2020) studied the insertion depth of the implant on the VF vibration and acoustic output using an idealized VF model, and their results agreed qualitatively with available experiment data. Wu and Zhang (2023) studied the effect of implant stiffness on the VF vibratory characteristics using an MRI-based model, and their results also had qualitative agreement with the *ex vivo* experiment of human larynges by Cameron et al. (2020). A more recent work by Movahhedi et al. (2021) studied the effect of the implant and performed virtual optimization by incorporating flow-structure-acoustics interaction and muscle activation of the VF, but there was no experiment validation in their study.

Following our previous works, in this study we have utilized an integrated approach to develop and validate the computation model based on rabbit phonation. However, different from previous works Li et al. (2023), the current study is focused on modeling of implant medialization as well as subsequent VF vibration with the implant included. In the experiment, a rabbit larynx is used to simulate the type-1 thyroplasty, where one side of the vocal

fold is medialized with trans-muscular suture to mimic the healthy side while the other side is medialized with a silastic implant as in type-1 thyroplasty. Vocal fold vibration is then achieved by flowing air through the larynx and is filmed with a high-speed camera. The 3D computational model is built upon the pre-operative scan of the laryngeal anatomy. This subject-specific model is used to simulate the vocal fold medialization and then FSI of the vocal fold. Model validation is done by comparing the vocal fold displacement with post-operative scan (for medialization), and by comparing the vibratory characteristics with the high-speed images (for vibration).

4.2 Method of experiments

The animal procedures were approved by the University of Pittsburgh's Institutional Animal Care and Use Committee (#21220467) and were performed on a New Zealand white rabbit. The rabbit was sedated with an intramuscular injection of 17.5 mg/kg ketamine and 0.125 mg/kg dexmedesed, laid supine, shaved from sternal notch to sternum, with a single incision made down the midline of the neck. This was followed by dissection of the skin, muscle, and fascia to expose the larynx. The larynx was excised for ex vivo procedures following euthanization by intravenous overdose of Sodium Pentobarbital.

The excised larynx was placed in perfluorocarbon oil and scanned before the medialization procedure (i.e., pre-operative) using MRI with a Bruker® AV3HD 11.7 tesla/89mm vertical-bore microimaging system. T-2 weighted images at an isotropic resolution of 60μ were obtained using a fast spin-echo sequence. Additional details for the MRI scanning are described in our previous work (Li et al., 2021b). The pre-operative scan was performed for the rest state with both VF sides abducted, i.e., rest configuration (or configuration 0), and a post-operative scan was performed with the implant on one side and suture medialization on the other side (configuration 3, as described next). An intermediate configuration was also introduced with one side medialized with the suture and the other side at the rest state. This configuration represented the phonation position at the UVFP configuration (configu-

ration 2), where the paralyzed side (the rest side) could not medialize on itself. The healthy condition with both sides medialized naturally using laryngeal muscles did not need to be modeled in this study (a previous work of ours was concerned with this condition, or configuration 1). Figure 4.1(a) shows the MRI scan of the post-operative VF at configuration 3. The pre-operative scan of the rest configuration was used to build the finite-element method (FEM) model for the subsequent numerical analyses, while the post-operative scan was used to compare vocal fold displacement from actual medialization with the numerically simulated medialization.

During thyroplasty surgery, an implant was inserted unilaterally via a window cut into the thyroid cartilage and secured below the VF muscle to medialize that side of the VF. In the current study, a laser-cut silastic implant having a simple cuboidal implant shape of 1 mm × 1 mm × 2 mm was inserted. The opposing side was medialized using a transmucosal suture that entered the larynx via the thyrohyoid membrane and secured by suturing through the thyroid cartilage and securing with a knot to maintain tension. This suture method was used to mimic medialization of the healthy side in the UVFP.

Following the post-operative MRI, the sample was removed from perfluorocarbon oil and rinsed with phospho-buffered saline, and ex vivo phonation was elicited. In this procedure, the larynx was mounted to pseudo-lung in an excised larynx cabinet and humidified air was supplied using a Neptune Conchatherm system (Medline, Northfield, IL) to elicit phonation, with subglottal pressure determined by an in line digital pressure meter (Cole-Parmer, Vernon Hills, IL). Phonation was initially captured for configuration 3 at 8000 fps using a stabilized AX50 high-speed video (HSV) camera (Photron, Tokyo, Japan). Following this, a control test was done for configuration 0 by removing the implant and the suture to recover the rest condition. Subglottal air pressure was consistent for all configurations, with air pressure maintained at the same level (2 kPa) that produced phonation in configuration 3. Additional details of the experimental setup and methodologies can be found in Novaleski et al. (2016) and Ge et al. (2009). The HSV was processed using a

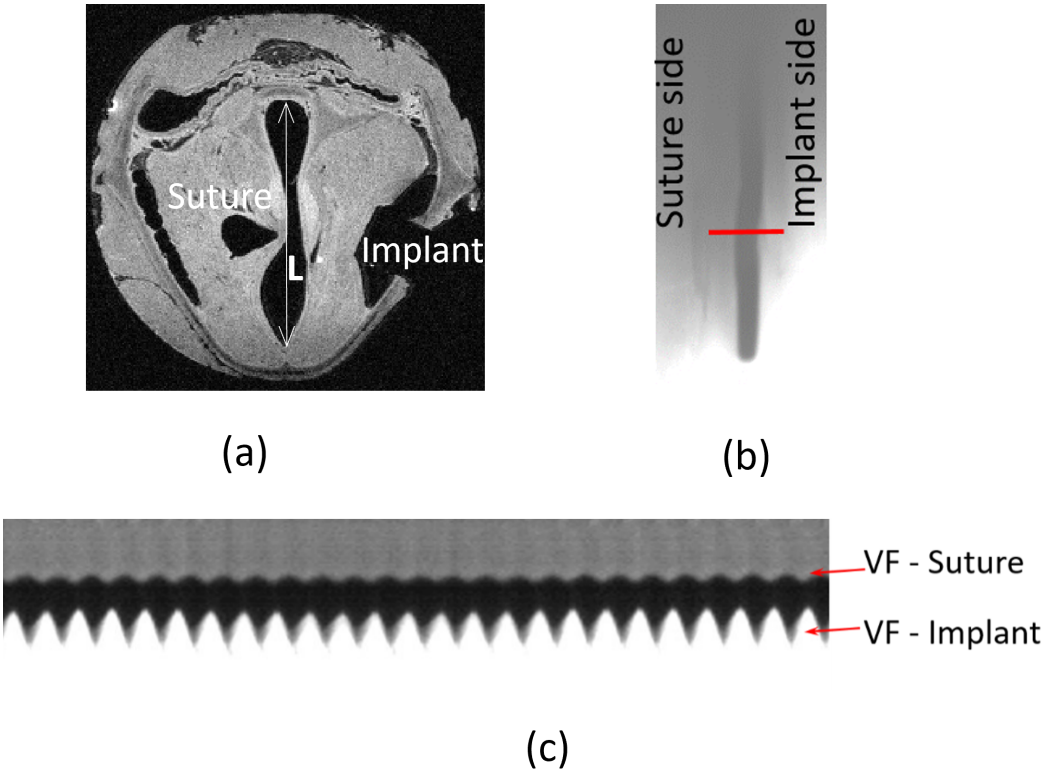

Figure 4.1: : (a) Post-operative MRI scan showing VF medialized by a unilateral suture (left side) and by silastic implant insertion (right side). The length between the anterior and posterior commissure is represented by L. (b) Image from the HSV showing an instantaneous moment of the VF vibration. The red line is where the kymograph was taken.(c) Kymograph showing VF vibration over time at the medialized state (configuration 3).

custom MATLAB code generously provided by Dr. Dimitar Deliyski from Michigan State University to Dr. Rousseau for digital kymograph analysis, as shown in Figure 4.1(c) In the kymograph, the vocal fold waveform, with time represented on the x-axis, was extracted from the HSV.

4.3 Method of computational modeling

4.3.1 Model construction

The laryngeal geometry was reconstructed from the pre-operative MRI scan at the rest configuration, where both VF sides were abducted. Manual segmentation was used in this process (Li et al., 2021b), during which thyroid cartilage, arytenoid cartilage, cricoid cartilage,

vocal fold body, and vocal fold cover were identified from the images and were separately segmented. Here, a two-layer structure, i.e., cover (lamina propria) and body (vocal fold ligament and muscles), was assumed for the vocal fold (Xue et al., 2014; Chang, 2016; Hirano et al., 1981). Another segmentation was done for the entire larynx, in which the lumen surface of the airway was excluded, and all the tissue components were not separated. The entire larynx and individual components were separately meshed in COMSOL Multiphysics (COMSOL Inc., Burlington, MA, USA); then each individual component was registered on the unified mesh model of the entire larynx (Figure 4.2) by comparing the unified mesh with the mesh of that component. Such an approach ensured that meshing of all the components was matched at the interface. Overall, the geometrical model contained a tetrahedral mesh of 94593 elements.

The unified mesh model, with individual components identified on it, was then imported into COMSOL for medialization simulation and subsequent eigenmode analysis. The implant was modeled as a rectangular block of length 2 mm and a width and depth of 1 mm each (Figure 4.3). The suture line was modeled as a flexible cylinder embedded in the tissue with a 0.3 mm diameter and 2 mm length. The specific locations of the implant and suture line are shown in Figure 4.3(b). These precise locations were obtained from the post-operative scan of the larynx. A rectangular window on the thyroid cartilage was created to facilitate implant insertion in the numerical simulation. To mimic the tissue separation from the thyroid cartilage, a gap was created between the thyroid cartilage and the connecting tissue adjacent to it. This gap spanned approximately 2 mm away from the implant edges in the longitudinal and anterior-posterior directions. A similar gap was created on the suture side. The region of tissue separation was approximated based on the observation in the post-operative MRI scan (Figure 4.1; also highlighted in Figure 4.5).

For tissue mechanics, the deformation of all the tissue components was assumed to be governed by the Saint-Venant Kirchhoff model, while Young's moduli of the VF cover and VF body were estimated based on the eigenmode analysis of the medialized state that is

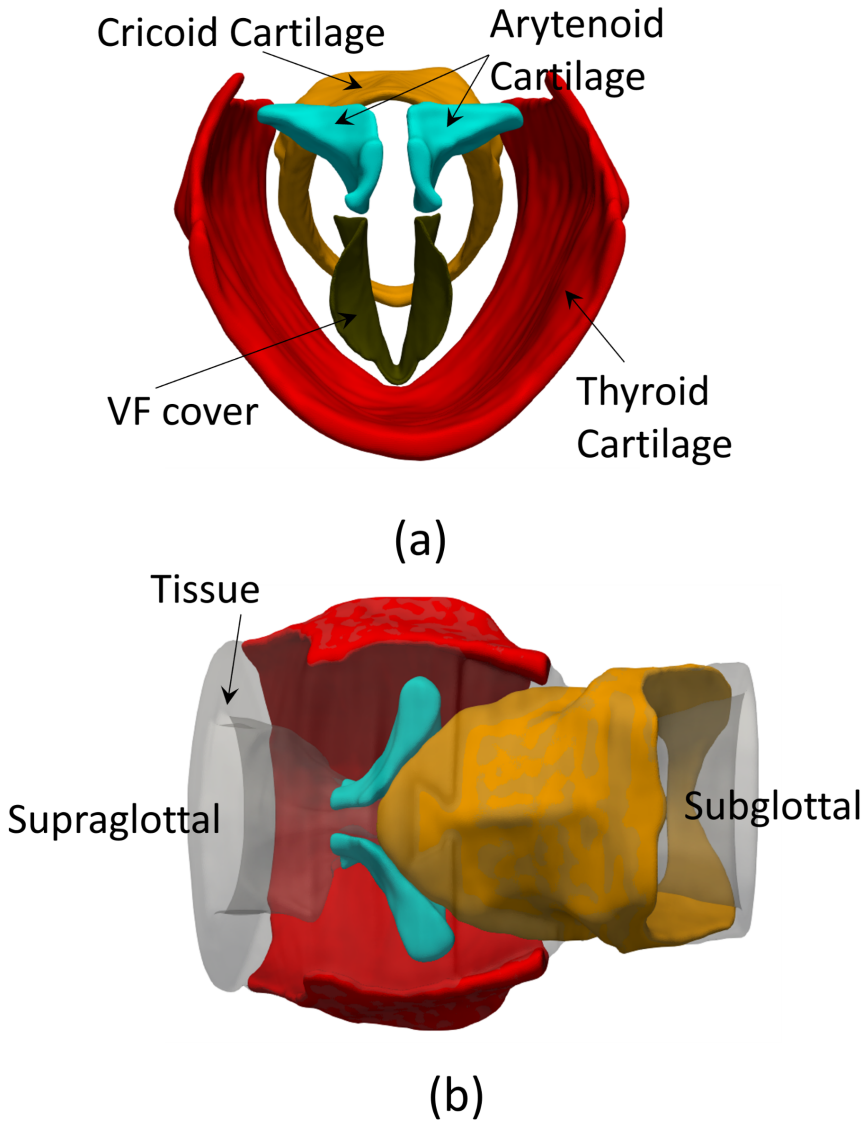

Figure 4.2: Reconstructed geometrical model showing the individual components from a supraglottal view (a) and from a posterior view (b). For clarity, the VF body and other connecting tissue were not shown here.

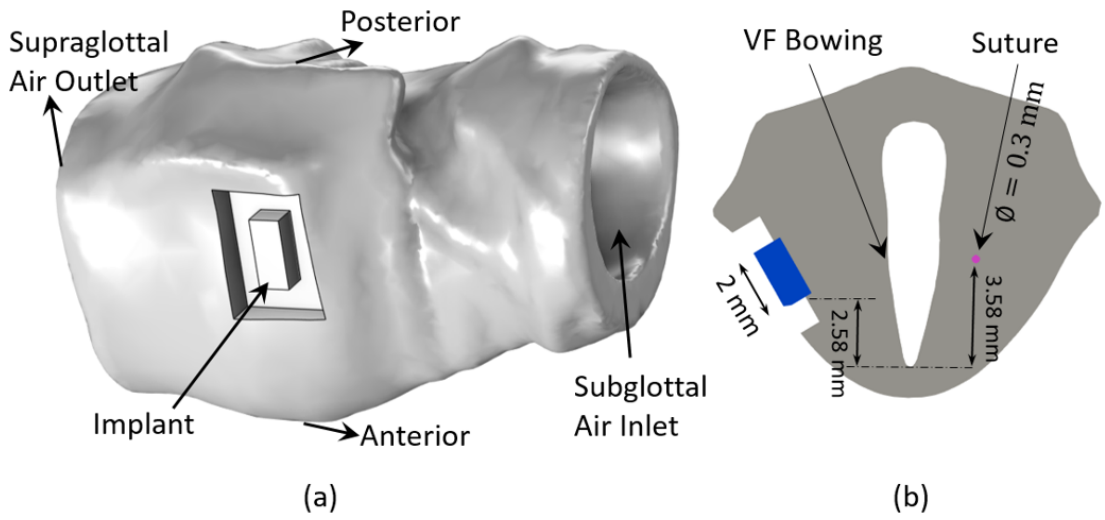

Figure 4.3: Solid model with implant and suture. (a) shows the 3D subject-specific FEM model with the implant. (b) shows the slice in the transverse plane showing the positions of implant and suture.

described next.

4.3.2 Simulation Setup

The numerical simulation was divided into three steps: (1) a quasi-static simulation of medialization in which both the implant side and the suture side were adducted toward the midline; (2) an eigenmode analysis of the vocal fold to check if its natural frequency agrees with the vibration frequency obtained from High-Speed Video (HSV); (3) an FSI simulation in which the glottal airflow and VF vibration were simulated. Steps (1) and (2) were iterated a few times in which Young's moduli of the VF were adjusted accordingly and the eigenmodes were re-calculated (Chang, 2016; Latifi et al., 2014). To repeat (1) and (2), the mesh model of the larynx, on which individual components identified, was imported into COMSOL to perform medialization simulation, and determine the eigenfrequencies at the medialized configuration (i.e., the prestressed state). The first step of VF adduction simulation was attained by using a force ramp that gradually pushed both the implant and suture line towards the midline. The simulation was continued until the implant and suture

line reached the equilibrium. In the FEM model, the outer surfaces of the thyroid and cricoid cartilages were fixed, and they had little deformation due to their high stiffness. The arytenoid cartilage and the inner lumen surfaces were free to move. Young's modulus for the cartilages and the suture line were assumed to be $E = 2000$ kPa, while the implant had a modulus of $E = 20000$ kPa representing a stiffer material (Movahhedi et al., 2021). The densities for tissue and cartilage were 1040 kg/m^3 and 1100 kg/m^3, respectively. For all the components, Poisson's ratio was set at $\nu = 0.3$.

Once Young's moduli of the VF body and VF cover were determined from steps 1 and 2, the FEM model was then imported to our in-house code for the 3D FSI simulation of the vocal fold vibration. These was conducted on Stampede 2 of TACC (allocation provided through the NSF XSEDE program). The 3D FSI simulation was performed at configuration 3, where the two VF sides were respectively medialized by the implant and suture line. The initial flow domain was extracted from the lumen surface of the medialized laryngeal geometry as shown in Figure 4.4, and the inlet and outlet were extended to accommodate the boundary conditions. At the inlet, the air pressure was set to be 2 kPa (gage). The time step for the FSI simulation was $\Delta t = 10^{-4}$ centi-seconds (cs). The mesh used in flow simulation was 156 in the axial direction, 108 in the lateral direction, and 108 in the anterior-posterior direction. The mesh resolution was verified in our previous study of the healthy phonation. The time required for completing 2 centi-seconds, or around 15 vibration cycles, of 3D FSI simulations was 50 hours when using 122 processor cores.

The airflow was assumed to be governed by the 3D viscous incompressible Navier – Stokes equation and was solved by using a Cartesian grid-based immersed-boundary method (Xue et al., 2014; Luo et al., 2008, 2009). For the FSI simulation, the flow solver and the FEM solver were coupled using a partitioned method (Tian et al., 2014), in which the two solvers were modular and were iterated until convergence was reached at the end of each time step. Readers can refer to our previous works (Chang, 2016; Tian et al., 2014) for detailed descriptions of the numerical method and extensive validation of the code.

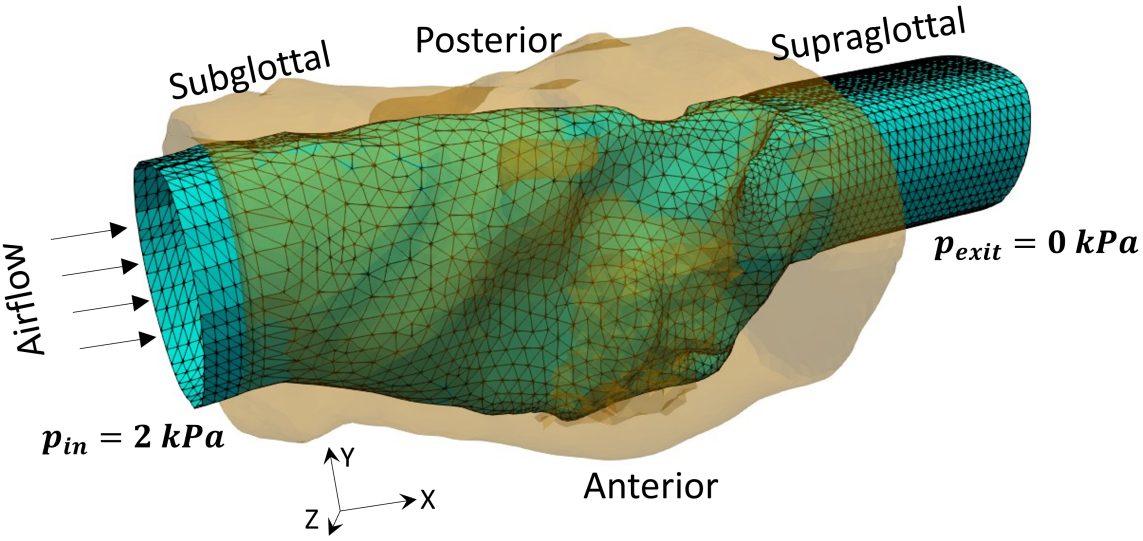

Figure 4.4: Boundary surface for the flow simulation shown as the blue mesh, where the inlet and outlet were extended from the extracted lumen surface. The 3D laryngeal tissue model is shown here as a semi-transparent structure surrounding the flow domain.

4.4 Results and discussions

4.4.1 Results of vocal fold medialization

The function of the medialization process is to reduce the glottal gap by positioning the two sides of the VF closer to the midline in order to promote and sustain the flow-induced VF vibration for phonation. The post-operative scan showed that our experiment achieved type 1 thyroplasty medialization using the implant (Figure 4.5(b)). As measured from the pre-operative scan in Figure 4.5(a), the narrowest gap between the two sides at the rest configuration was 1.63 mm. After implant and suture medialization, this gap was reduced effectively by 1.33 mm, which could be measured from the pre- and post-operative scans.

The corresponding simulation result showed that such medialization was captured by the FEM model (Figure 4.5(d-f)). The initial glottis from the reconstructed larynx at the rest configuration (Figure 4.5(d)), as well as the medialized glottis from the FEM simulation (Figure 4.5(e)), closely resembled their respective shapes from the scan as seen from the axial view in Figure 4.5(a,b). To achieve the medialization in the simulation, the total forces of 0.6 N and 0.85 N were used to displace the implant and the suture, respectively,

by approximately 2 mm towards the midplane. The forces maintained the two sides at the equilibrium state, at which the medial surface (the outer surface of the VF cover) was displaced by 0.43 mm on the implant side and by 0.82 mm on the suture side. These results agreed with the measurements from the post-operative scan. The higher displacement on the suture side was mainly because of localized tissue displacement surrounding the suture line. The asymmetric adduction of the two sides was expected since two different methods of medialization were employed in the current study.

The overall extent of medialization could be also measured by the amount of area reduction at the glottal section. From both the MRI scans and simulation results, the glottal areas were reduced from 11.6 mm^2 to 5.5 mm^2 and 6 mm^2, respectively, by the medialization. A unilateral medialization by suturing alone (i.e., the UVFP configuration without implant insertion) led to a greater glottal area of 8.4 mm^2. The degree of area reduction would have significant effects on the VF vibration as shown later.

Some differences between the experiment and simulation could be observed from the coronal view (Figure 4.5(c,f)), especially for the suture side. Note that in Figure 4.5(c), the tightened suture line created significant displacement of the false vocal fold that is above the true vocal fold, which led to narrowing of the supraglottal region. In the simulation, the suture line was not as soft as in the experiment and thus did not curve as much to cause deformation of the false vocal fold. Such differences were deemed acceptable since the medialization of the true vocal fold, were reasonably captured by the simulation. In addition, the false vocal fold deformation of the suture side did not significantly affect the VF validation for the implant side.

One specific issue was caused by VF tissue separation from the thyroid cartilage when the VF was being pushed toward the midline. Such tissue separation was evident from the post-operative scan (Figure 4.5(b,c)). To incorporate the presence of the separation, the gap between the thyroid cartilage and the VF body was created as described in Section 4.3.1. From the simulation results shown in Figure 4.5(e,f), the enlargement of these gaps during

Table 4.1: VF frequency from the eigenmode analysis (both rest and medialized configurations), 3D FSI simulation, and high-speed videoendoscopy of phonation experiment.

VF frequency (Hz)	Eigenfrequency for rest configuration	Eigenfrequency for medialized configuration	Phonation experiment	3D FSI simulation
Implant Side	595	768	820	733
Suture Side	575	770	819	733

medialization had significant effects on the VF displacement and thus was necessary to include in the modeling process.

4.4.2 Eigenmode analysis and vocal fold stiffness

Eigenfrequencies from the eigenmode analysis were to adjust the tissue stiffness properties, or Young's moduli of the vocal fold, of the sample, and also to study the asymmetries in the vibration mode between the two sides of the VF. The vibration frequency of the current sample at the medialized configuration was approximately 820 Hz according to the high-speed video. Although the eigenfrequency of the rest state is related to Young's modulus by $f_0 \propto 1/l^2\sqrt{E/\rho}$, where l is the VF length, E is the material stiffness, and ρ is the density (Zhang et al., 2009; Kelleher et al., 2010), the presence of the internal stresses due to medialization may change the relationship by stiffening the tissue effectively (Palaparthi et al., 2019; Smith et al., 2020). After a few iterations of medialization simulation and eigenmode analysis, the Young's moduli of the VF cover and VF body were adjusted so that eigenmode analysis of the medialized configuration produced frequencies of the both sides that were close to the experimentally observed frequency. The final results are listed in Table 4.1 for clarity. The corresponding eigenmodes of the two sides are shown in Figure 4.6. Although there were multiple modes from the eigenmode computation, only the mode that corresponded to the opening and closing of the glottis was chosen to guide the analysis.

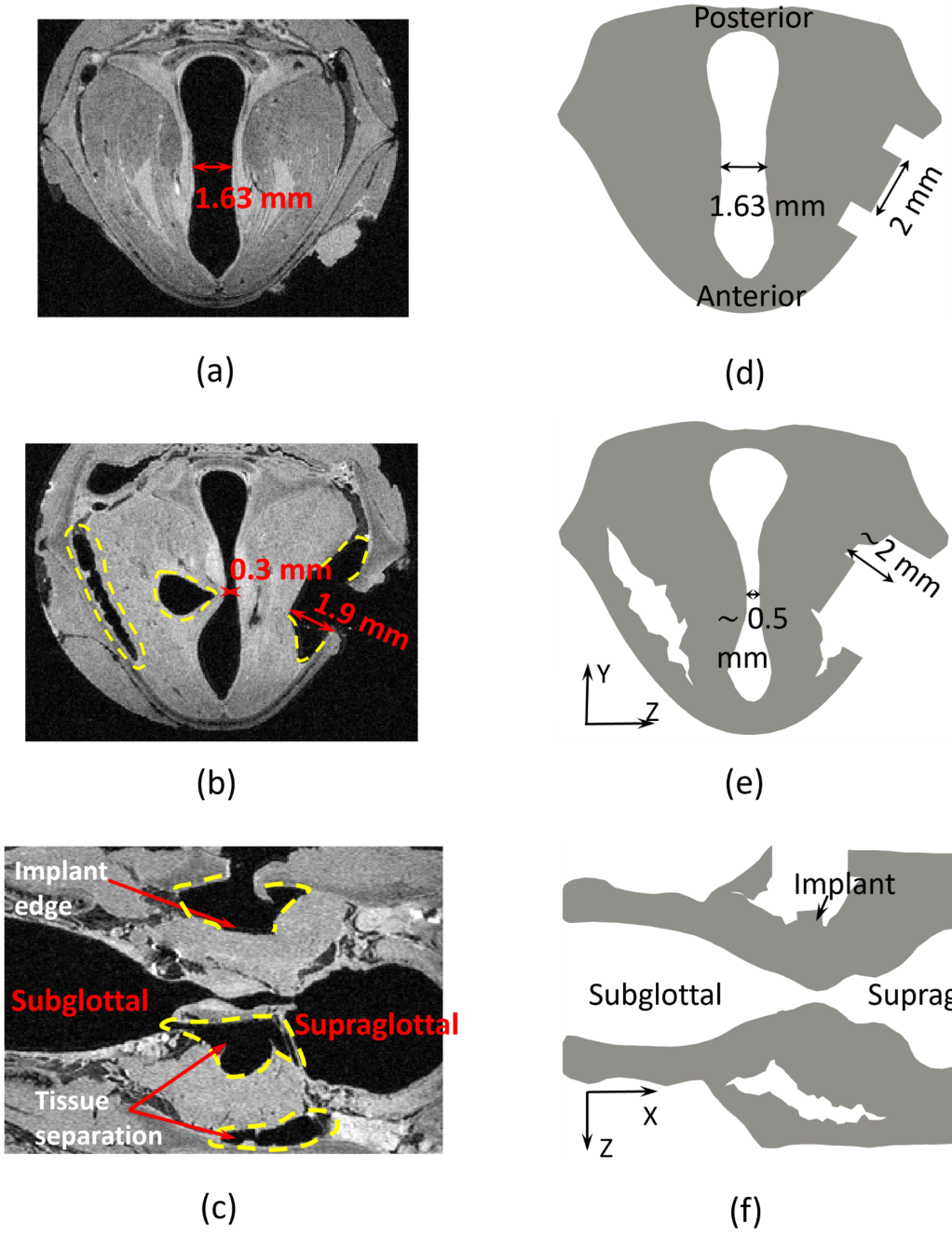

Figure 4.5: Comparison of VF displacement between the MRI images (a-c) and the numerical simulation (d-f). (a,d) The initial rest configuration; (b,e) medialized configuration in the axial view; (c,f) medialized configuration in the coronal view. The yellow dashed line in (b) and (c) indicates the tissues separation from the medialization.

This study resulted in Young's modulus for the VF cover $E_c = 60$ kPa and for the VF body $E_b = 150$ kPa, which led to an eigenfrequency of 768 Hz on the implanted side and 770 Hz on the suture side. Previously, experiments with the rabbit VF by Latifi et al. (2014) showed that Young's modulus could be as high as 174 kPa for the VF cover. Oren et al. (2014) explained tissue stiffness value as a function of strain and several other studies have reported higher E (Miri, 2014; Bauer and König-Heidelberg, 1967; Chan et al., 2007; Perlman et al., 1984; Chang et al., 2013) when tested for high strain values. In comparison, Young's moduli adopted in the current work were in the ballpark of available data.

As a reference, eigenfrequencies of the rest configuration were also computed and listed in Table 4.1. The two sides corresponding to the implant side and suture side had an eigenfrequency of 600 Hz and 575 Hz, respectively, which were much lower compared to the frequencies at the medialized state. This result shows that medialization caused significant internal stresses, leading to tissue stiffening and increase of the vibratory frequency. After medialization, the Von-Mises stress was approximately 21 kPa and 30 kPa on the implant side and suture side VFs, indicating presence of significant stresses in the tissue. At the medialized state, the eigenfrequencies of the two sides became much closer to each other. This frequency symmetry would be beneficial in general for restoration of VF vibration from the UVFP condition and thus could be a factor for consideration in addition to the extent of glottal area reduction.

4.4.3 Results from the 3D FSI Simulation

Two cases were considered for 3D FSI simulation: 1) the medialized condition (configuration 3), where both the implant and suture medializations were present; 2) the UVFP condition (configuration 2) with only the suture medialization present, which served as a reference case for comparison. In both cases, an inlet gage pressure of 2 kPa was used to initiate flow-induced vibration.

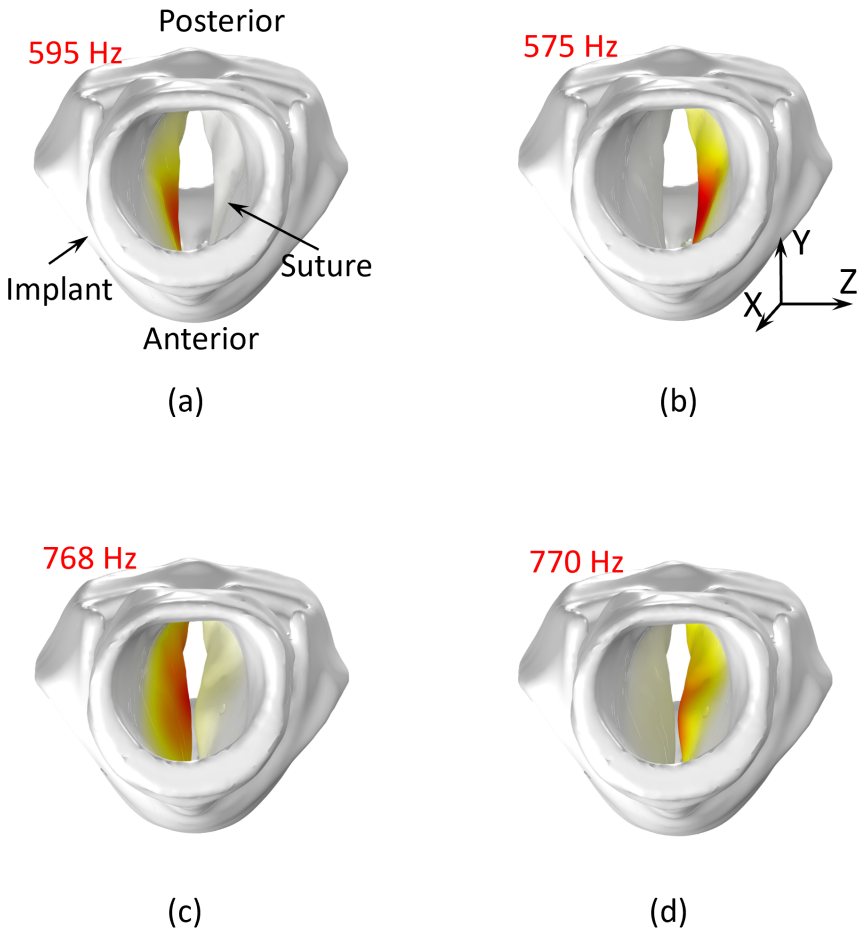

Figure 4.6: (a, b) Eigenmodes of the rest configuration for the implant and suture sides, respectively. (d, e) Eigenmodes of the medialized configuration for the implant and suture sides, respectively.

4.4.3.1 The Unilateral Vocal Fold Paralysis (UVFP) configuration

At this diseased condition, onset of phonation becomes difficult even though the healthy side can be medialized. This is because the glottal gap is wide, and the subglottal pressure is insufficient to induce VF vibration. This situation was reflected from the FSI simulation of this configuration. As shown in Figure 4.7(a), the vibration amplitude of both rest side and suture side was small and less than 0.05 mm. An FFT analysis showed that the vibration frequency was 733 Hz for the suture side and 595 Hz for the rest side, which generally matched the respective eigenfrequencies of that side. Since the amplitude of vibration was small and the glottal gap was relatively constant, a consistent jet of airflow was created from the glottis. At the narrowest cross-section in the glottis, the flow velocity was about 57 m/s (Figure 4.7(c,d)). This jet became asymmetric in the coronal plane and skewed toward the suture side (Figure 4.7(c,d)). Since the VF was inclined at an angle of 23 degrees from the axial direction (Figure 4.7(b)), the jet was guided toward the anterior side of the vocal fold and impinged on the supraglottal region's anterior end (Figure 4.7(e,f)). Like the flow velocity, the pressure distribution along the axial direction also remained largely steady and did not change much between opening and closing phases Figure 4.7(g,h).

4.4.3.2 Results from the medialized configuration

At the rest configuration, no clear VF vibration was observed in the experiment. With the suture and implant medialization, significant vibration was observed from the HSV, although the vibration was dominated by the implant side and the suture side had little vibration as seen from the kymograph in Figure 4.1(c).

The corresponding 3D FSI simulation achieved similar vibratory characteristics. From Figure 4.8(a), the implant side had an amplitude about twice as high as the amplitude of the suture side. The vibration frequency in the simulation was 733 Hz and close to the frequency of 820 Hz that was measured from the HSV. Furthermore, the amplitude of the implant side was 0.15 mm, or 2.1% of the length of the glottis (L). In the HSV, the

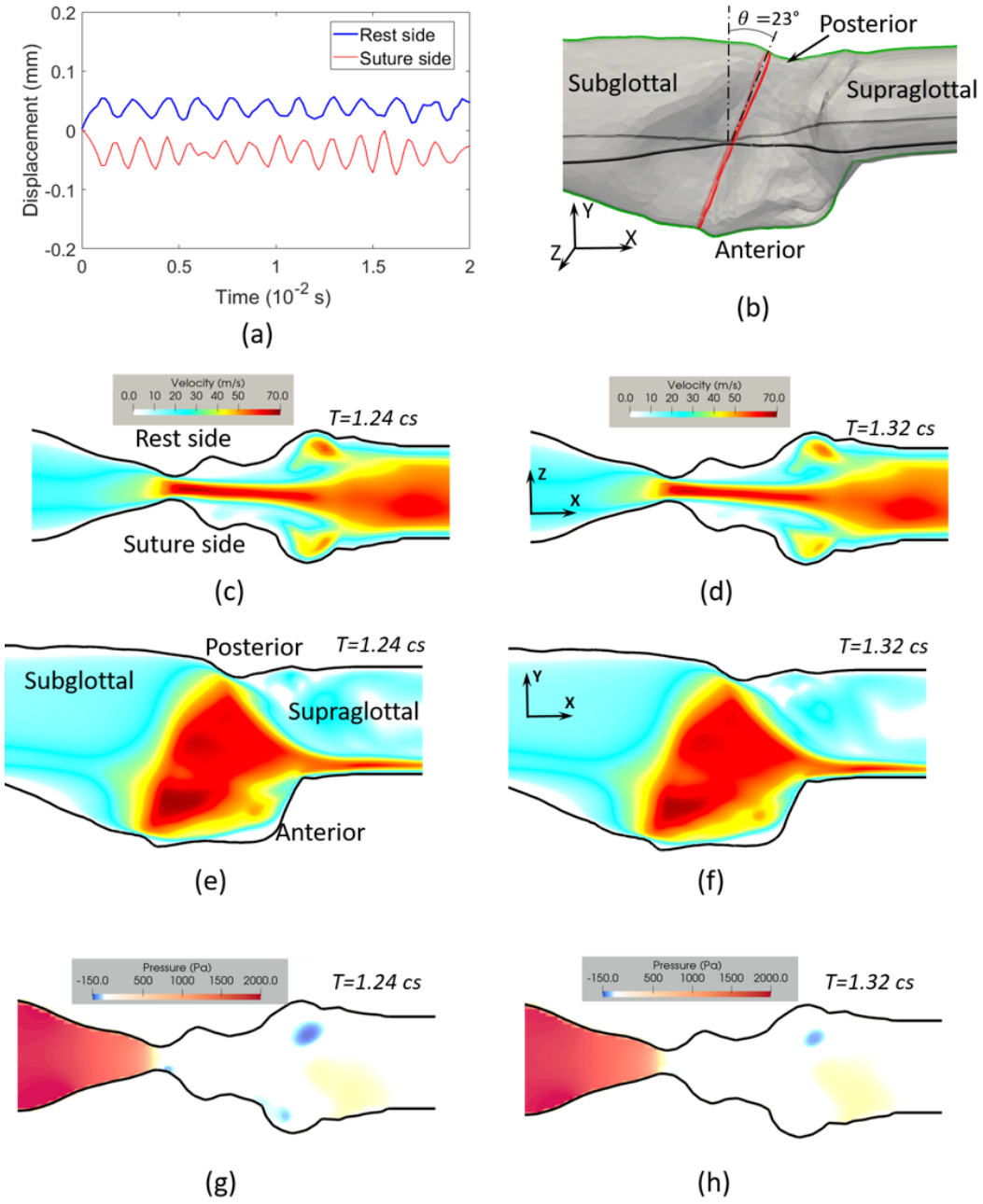

Figure 4.7: FSI simulation results for the UVFP configuration. (a) Displacement of the two VF sides measured around mid-point of the glottis. (b) The flow domain showing the coronal plane (horizontal slice in the figure) and the mid-sagittal plane (vertical slice) for visualization; also included is the orientation of the glottis. (c, d) Velocity magnitude at the closing phase (c) and opening phase (d) in the coronal plane. (e, f) Velocity magnitude at the closing phase (e) and opening phase (f) in the mid-sagittal plane. (g, h) Pressure distribution in the coronal plane for the closing (g) and opening (h) phases.

amplitude of the implant side was 2.6% of L (note that the HSV did not have a length scale; thus, a relative measurement was used here). One difference between the simulation and experimental results was that the suture side in the experiment had less vibration than in the simulation. This was like because in the experiment, the suture line created a significant tissue tear around the line (Figure 4.5(b,c)). This torn region was not incorporated in the model but may have limited the amplitude of that side since there was less mass involved in the vibration.

Overall, the amplitude, frequency, and left-right asymmetry of the simulated vibratory characteristic agreed with those from the phonation experiment. Therefore, the current computational model of type 1 thyroplasty was validated by the experiment in our study.

We point out in human patients that the healthy side of the VF normally has a greater vibration amplitude than the implant side (Qiu et al., 2003; George et al., 2008), which is opposite to the current rabbit study. We attribute this difference to the way that the 'healthy side' was mimicked in the current study. Since a suture line was used to pull the VF toward the midline, the thin line had caused large displacements around the line and thus localized glottal narrowing (see Figure 4.5(b)) as opposed to overall narrowing of the glottis. Furthermore, the localized displacements may have created significantly uneven tension in the tissue that did not necessarily promote the vibration. As a result, the suture side had a much lower amplitude as compared to the implant side in our study. The implication of this issue will be discussed further in the next section.

Flow visualization of the medialized configuration using the simulation data showed certain characteristics as observed in healthy phonation that was studied previously for rabbits (Avhad et al., 2022). As seen in Figure 4.9(a), the flow rate was pulsatile and overall periodic, although it did not reduce to zero at the closing phase due to incomplete closure of the VF. In the current configuration, the mean airflow rate was 235 cm^3/s, while for the UVFP condition it was 330 cm^3/s. The lack of significant vibration amplitude in the UVFP configuration contributed to less variations in the flow rate between phonatory cy-

cles compared to the medialized configuration. From Figure 4.8(c,d), the jet was mostly symmetric as viewed in the coronal plane despite the fact that the VF vibration was asymmetric. This improvement from the UVFP configuration was a result of medialization on both sides of the VF (so that the overall geometry was more symmetric in the medialized state). The presence of the false vocal fold in the supraglottal region also helped maintain the symmetry of the jet, which was beneficial for phonation (Luo et al., 2009; Zheng et al., 2009).

Comparing temporal characteristics of the flow field with that of the UVFP, the jet velocity had more variations between the VF opening and closing phases for the medialized configuration (Figure 4.8(c,d)). Like the UVFP, the jet in the medialized configuration was also directed toward the anterior side (Figure 4.8(e,f)), a feature that was also observed in the healthy phonation of rabbits (Avhad et al., 2022).

Because of a narrower glottal gap, the pressure in the glottis became negative and was significantly lower than that in the UVFP (Figure 4.8(g,h)), especially when the VF is closing ((Figure 4.8(g)). This comparison could be further seen from the pressure oscillations in the glottis ((Figure 4.9(b)). Not only the pressure oscillations had a greater magnitude in the medialized configuration, but also its time average became negative. Such temporal characteristics was a direct result of VF vibration, and it in turn helped to sustain the flow-induced vibration. In Figure 4.9(b,c), both the velocity and pressure displayed nearly periodically, corresponding to the improved vibration of the VF from the UVFP.

4.5 Further Discussion

This study has a few important limitations. For example, the experiment was carried out ex vivo because of difficulties associated with the in vivo surgery. Note that previously we had performed an in vivo study phonation and high-speed imaging using a rabbit model (Avhad et al., 2022; Chang, 2016). However, the current study involved different adduction methods for the two sides of the VF, the in vivo approach thus would be significantly

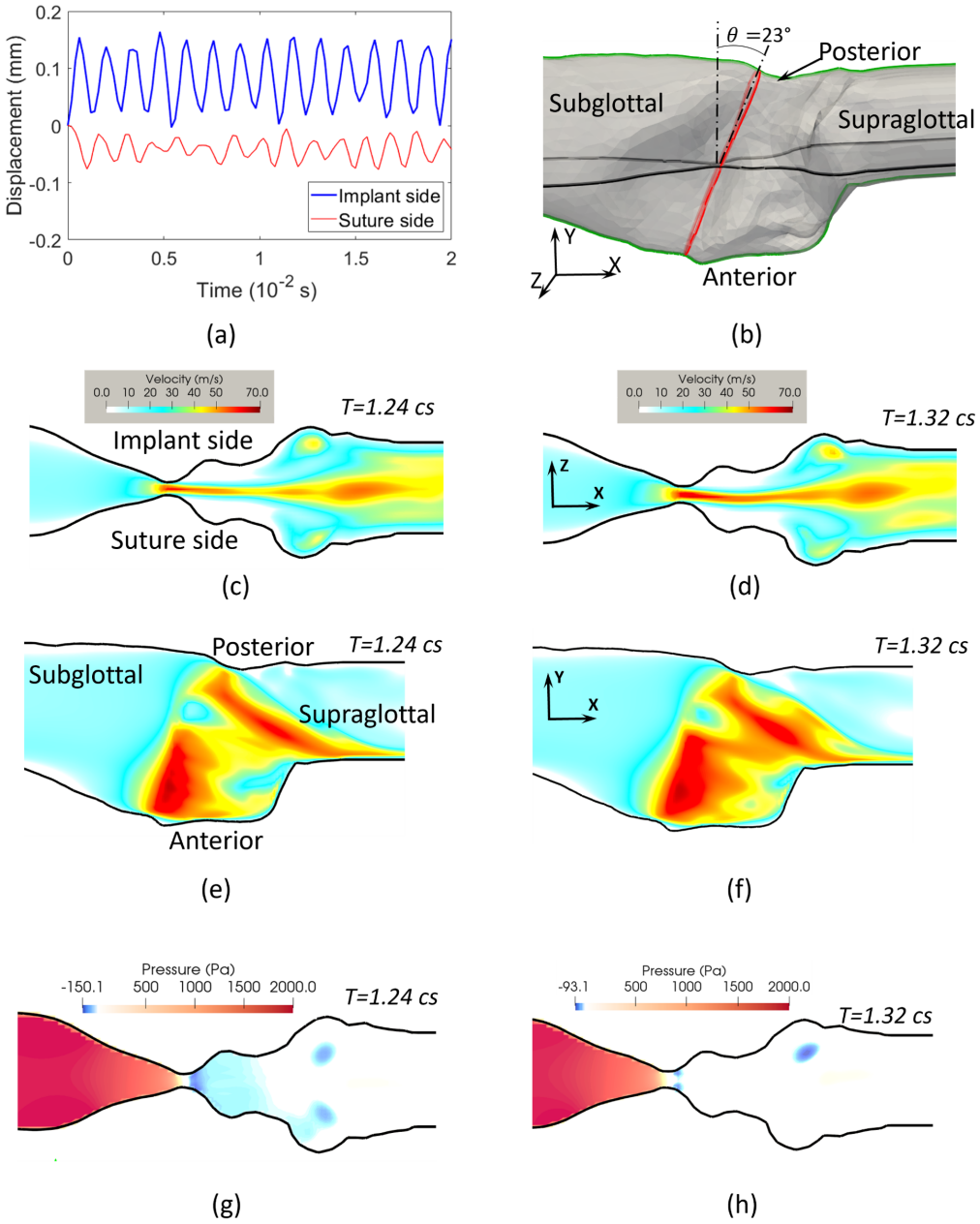

Figure 4.8: FSI simulation results for the medialized configuration. (a) Displacement of the two VF sides measured around mid-point of the glottis. (b) The flow domain showing the coronal plane (horizontal slice in the figure) and the mid-sagittal plane (vertical slice) for visualization; also included is the orientation of the glottis. (c, d) Velocity magnitude at the closing phase (c) and opening phase (d) in the coronal plane. (e, f) Velocity magnitude at the closing phase (e) and opening phase (f) in the mid-sagittal plane. (g, h) Pressure distribution in the coronal plane for the closing (g) and opening (h) phases.

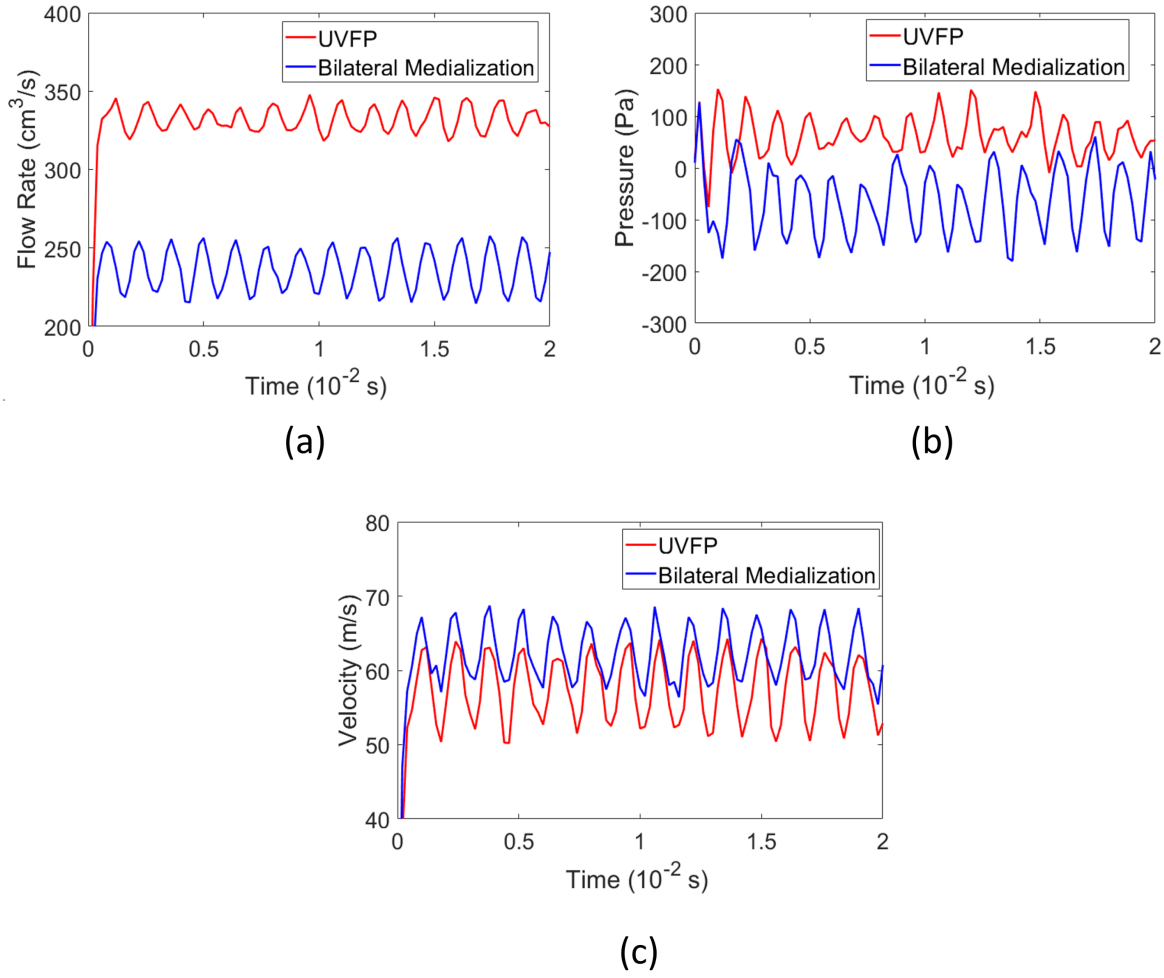

Figure 4.9: Comparison between UVFP and medialized configurations for the flow rate (a), pressure (b) and flow velocity (c) around mid-point in the glottis.

more difficult to carry out. Thus, an ex vivo approach was adopted. Furthermore, the suture method was used here to mimic the VF adduction of the healthy side, which created unnatural local stress and strain concentrations. As a result, this side of the VF did not produce significant vibration as the implant side did, which was different from human patients. Lastly, we did not perform an optimization study to test the best insertion location or shape design parameters for the implant, as such a study would require repeated FSI simulations to assess the effect of the implant on the VF vibration (albeit an optimization study of the implant location on the extent of medialization was performed previously by our group (Li et al., 2023)). Such optimization will be deferred to a following study.

Despite these limitations, the current study still represents an important step toward integrating animal experiment with computer simulation to explore the development of a computational modeling based, individual-specific, surgical planning tool for type 1 thyroplasty. In this study, we have developed the key steps of the procedure that included pre-operative scan, construction of the computational model, estimate of the tissue stiffness properties, post-operative scan, phonation experiment, and validation of the computational model. Although the surgical adduction of the healthy VF side was not natural, the current study successfully demonstrated the capability of modeling the effect of the implant on the VF vibration. We anticipate that a similar procedure could be developed for a physical experiment that mimics the type 1 thyroplasty more closely. Furthermore, a following optimization study would be straightforward to determine the best location and design of the implant, despite the high computational cost that could be involved.

4.6 Chapter conclusions

An integrated experimental and computational study of type 1 thyroplasty was carried out using an ex vivo rabbit larynx. The experiments included various vocal fold configurations that were created surgically to mimic the unilateral vocal fold paralysis as well as the medialized configuration using a silastic implant. Additionally, both pre- and post-

operative MRI scan of the larynx were performed, the flow was introduced to excite the vocal fold, and high-speed imaging was conducted to film the vocal fold vibration. On the computational side, a FEM model was built based on the preoperative scan, and medialization of both sides were simulated to achieve the adducted glottis. Young's moduli of the vocal fold were estimated by performing the eigenmode analysis and adjusting the eigenfrequencies. Finally, a 3D FSI simulation was performed to simulate the vibration, and the vibratory characteristics agreed with the phonation experiment, thus validating the computational model. Furthermore, the medialized vocal fold after thyroplasty showed favorable characteristics in vibration and the flow field when compared to the UVFP. These results demonstrate the potential of using the current approach for surgical planning of implant design and placement in type 1 thyroplasty.

CHAPTER 5

Computational optimization of type-1 thyroplasty through FSI simulations

5.1 Introduction

Performing computational study and optimization of the implant for type-1 thyroplasty prior to the surgical operation and generating useful guidance for the surgeon is the overarching goal of this research project. In previous chapters, we have conducted computational modeling studies of the healthy phonation condition, diseased or UVFP condition, as well as type-1 thyroplasty or surgical condition. At each of these conditions, we have performed an integrated experimental/computational study for model construction and validation. In this chapter, we will build upon these previous steps and move toward computational optimization of the implant as if this optimization were for pre-surgical planning. Here, surgical planning is in a hypothetical sense because no corresponding experiment is being carried out currently to test the numerically optimized implant and validate its optimality. The objectives of the numerical study in this chapter are to investigate the sensitivity of the implant window placement on the vocal fold vibration for the present animal model, to gain physical insight into the effects of the implant location and depth, and to explore practical issues related to numerical optimization such as parameter space and computational cost.

To summarize this study, we utilize the subject-specific larynx model built in Chapter 4 as the baseline case, which includes the 3D laryngeal geometry, tissue properties, implant location, medialization of the healthy side, as well as the simulation setup. Then, we systematically vary the window location of the implant in the anterior-posterior and the inferior-superior directions. FEM simulation of implant medialization is repeated for each case, and the degree of the vocal fold closure is measured. Then, FSI simulations are performed for each case to assess the effect of the implant location on the fundamental frequency, vibration amplitude, and other characteristics including the flow behavior. The

result of optimization and its implications will be discussed in the end.

5.2 Computational model and optimization setup

The 3D laryngeal geometry was reconstructed from the pre-operative MRI scan at the rest configuration as discussed in detail in Section 4.3.1 of Chapter 4. The vocal fold was assumed to be a two-layer structure, i.e., cover (lamina propria) and body (vocal fold ligament and muscles). Here we aim to study the effects of the implant location. Thus, the implant window location described in Chapter 4 formed the 'baseline' case in our current study (refer to Figures 4.2, 4.3 and 5.1(a)) in which the specific location of the implant and suture line were obtained from the post-operative scan of the larynx. Figure 5.1(a) provides the quantitative information on the implant location in the baseline case. Specifically, the implant was 3.2 mm from the inferior end of the thyroid cartilage and 4.1 mm from the midplane.

To study the effect of the implant location on vocal fold vibration, we systematically adjusted the initial (prior to insertion) implant location either in the subglottal-supraglottal (SS) direction, or in the anterior-posterior (AP) direction. In the subglottal-supraglottal (SS) direction, we moved the implant by 1 mm or 2 mm from the baseline location toward the supraglottal direction (SS-1 or SS-2, respectively), or 1 mm or 2 mm toward the subglottal direction (SS+1 or SS+2, respectively), as shown in Figure 5.1(b). Similarly, we moved the implant by 1 mm or 2 mm from the baseline location toward the anterior direction (AP+1 or AP+2, respectively), or 1 mm or 2 mm toward the posterior direction (AP-1 or AP-2, respectively), as shown in Figure 5.1(c,d). Therefore, there were nine cases of implant location.

For all the cases, the suture side representing the "healthy side" of the vocal fold remained the same in terms of the location of the suture and magnitude of adduction. As discussed in Chapter 4, significant tissue separation from the thyroid cartilage was observed in the post-operative scan. Since this separation has a significant effect on the degree of VF

adduction, it was incorporated here in each case. In doing so, we created a gap between the thyroid cartilage and the VF tissue adjacent to it as described in Section 4.3.1. This gap spanned approximately 2 mm away from the implant edges in both the inferior-superior and anterior-posterior directions.

The material properties of the tissue and air are both the same as those in Chapter 4. Specifically, Young's modulus for the VF body and cover are $E_b = 150$ kPa and $E_c = 60$ kPa, respectively. For all the components, Poisson's ratio was set at $\nu = 0.3$.

The implant shape in this study is somewhat different from that in Chapter 4 and is tapered toward the anterior direction to conform to the general shape of the thyroid cartilage (Figure 5.3). This shape is also commonly used in human thyroplasty (Desuter et al., 2017; Daniero et al., 2014; Zapater et al., 2019). In the experimental study described in Chapter 4, a rectangular shape of the implant was used for convenience due to the small size of the rabbit larynx and of the implant.

In addition to the nine implant locations, we also explored two variations of implant insertion depth. In the first group, the implant apex (the posterior edge) penetrates 2 mm into the tissue, while the anterior edge penetrates 1 mm (Figure 5.3(a)). In the second group, the implant apex reaches 3 mm inside the tissue, and the anterior edge reaches 2 mm (Figure 5.3(b)). For the second group, only five implant locations were considered, i.e., SS$\pm$1, AP$\pm$1, and the baseline.

5.3 Simulation setup

As described in Chapter 4, here the numerical simulation followed a two-step procedure: (1) a quasi-static medialization simulation, replicating the implant insertion in type-1 thyroplasty surgery (depicted in Figure 5.3) on the paralyzed side of the VF, and (2) a fluid-structure interaction (FSI) simulation of the VF vibration at the medialized state.

The simulation parameters were consistent with those described in Section 4.3.2. At the inlet, the pressure was set to be 2 kPa (gage). At the outlet, the pressure was kept at

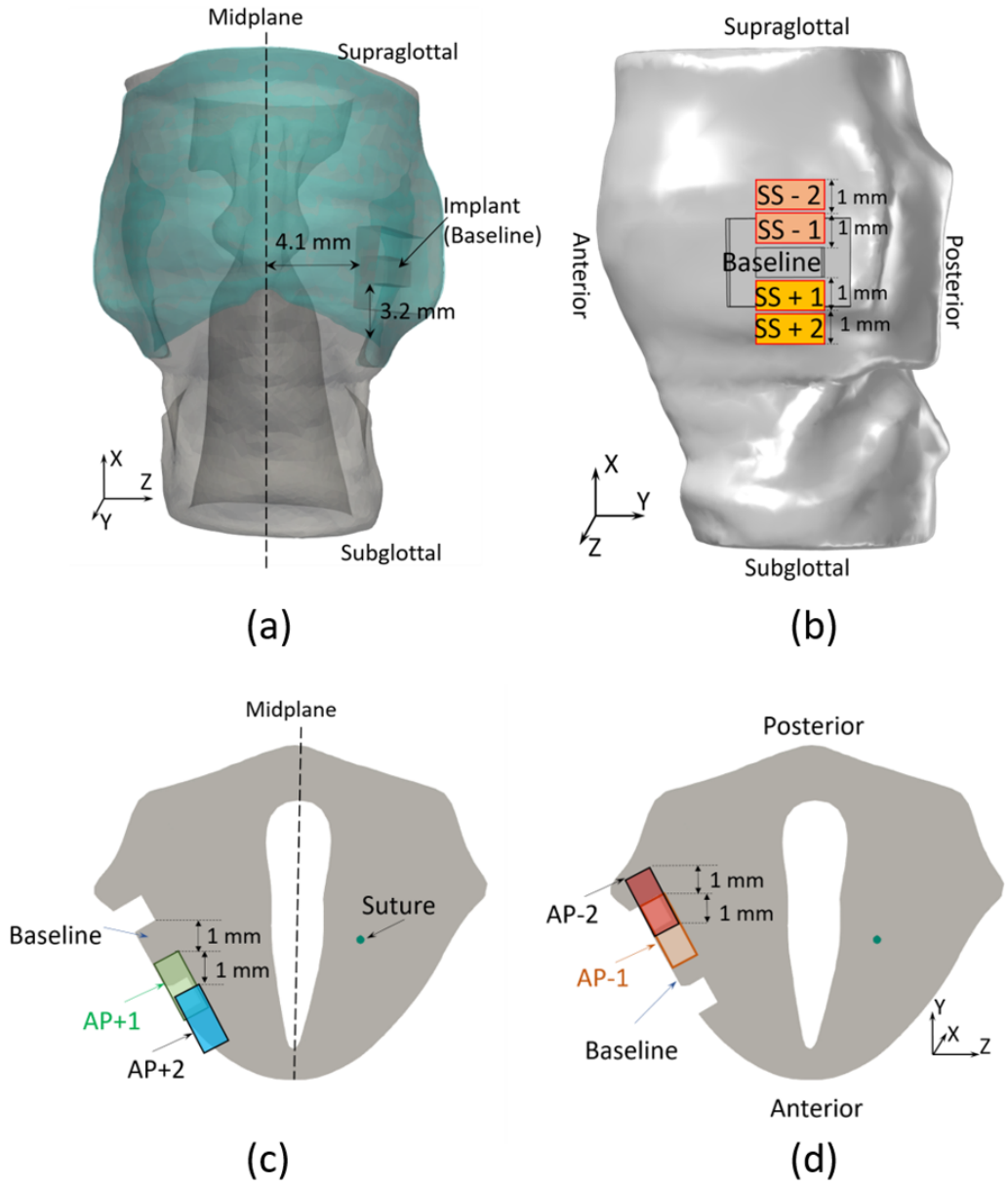

Figure 5.1: Illustration of various implant positions considered in this study with their nomenclature. (a) The baseline location from Chapter 4, (b) new implant positions along the subglottal-supraglottal direction, (c) and (d) new implant positions towards the anterior and posterior directions, respectively.

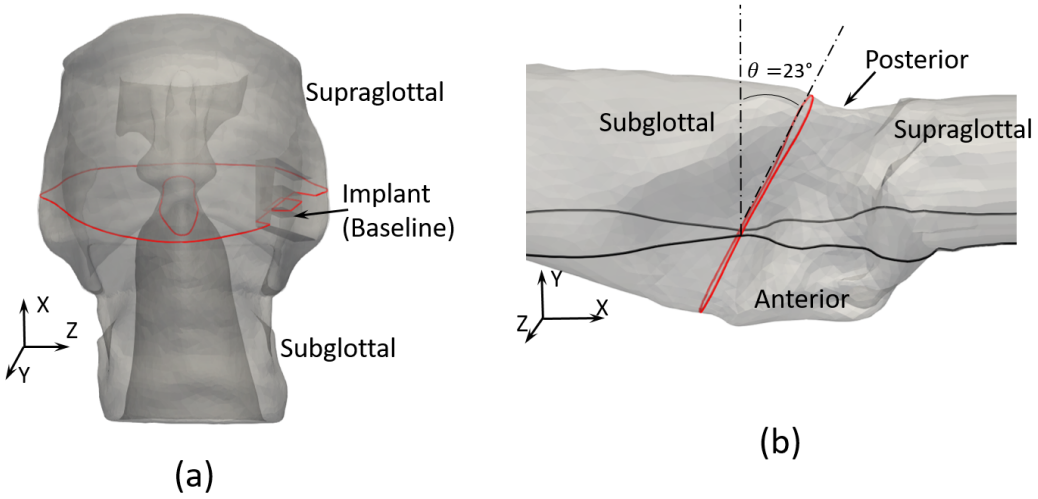

Figure 5.2: Illustration of the plane (red line) in which the VF adduction and vibration were evaluated. The plane generally cuts through the narrowest section of the glottis. (a) A 3D view of the layrnx; (b) lumen surface only. The glottis orientation is measured by the angle θ.

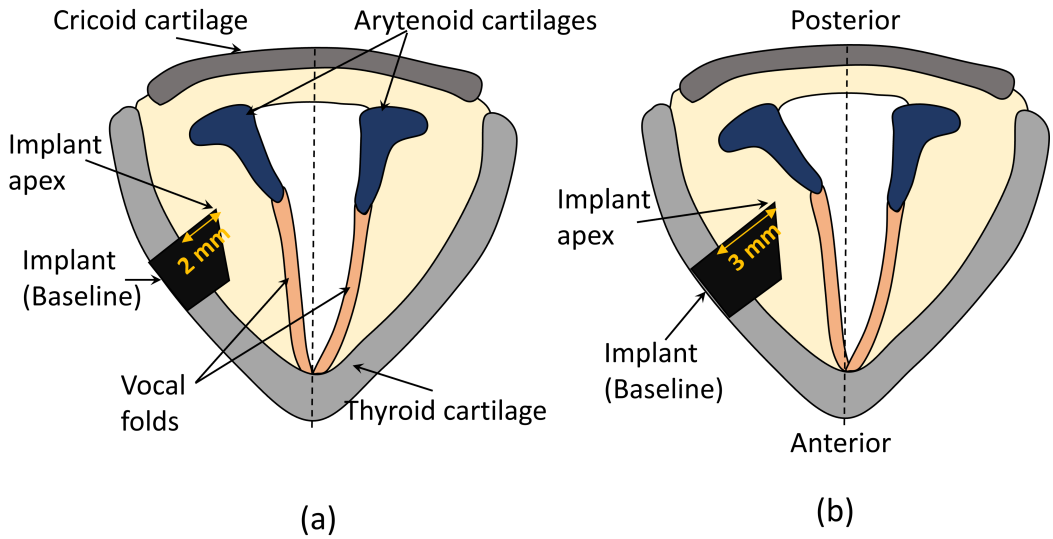

Figure 5.3: (a) Illustration of implant shape and insertion depth. (a) Insertion depth of 2 mm, and (b) 3 mm.

Table 5.1: Glottal Area, VF curvature radius (implant side), and VF displacement at the midpoint (implant side) in various cases after type-1 thyroplasty medialization simulation.

Implant location	Glottal area (mm^2)	VF curvature radius (mm) and shape	VF displacement (mm)
Group 1 (insertion depth 2 mm)			
Baseline	6.5	32 (Concave)	0.29
SS+1	6.4	36 (Concave)	0.27
SS-1	6.6	35 (Concave)	0.3
AP+1	5.8	20 (Convex)	0.4
AP-1	6.8	17 (Concave)	0.23
SS+2	7.1	32 (Concave)	0.2
SS-2	7	22 (Concave)	0.14
AP+2	6.6	21 (Convex)	0.36
AP-2	6.9	11 (Concave)	0.18
Group 2 (insertion depth 3 mm)			
Baseline	5.7	74 (Convex)	0.48
SS+1	6.3	53 (Concave)	0.36
SS-1	6.5	67 (Concave)	0.32
AP+1	5.5	14 (Convex)	0.51
AP-1	6.2	24 (Concave)	0.3

0 kPa (gage). For the solid mechanics, each laryngeal model consisted of approximately 90,000 tetrahedral Tet10 elements and 150,000 mesh points. The FSI simulation employed a time step of $\Delta t = 10^{-4}$ centi-seconds (cs).

These simulations were conducted on Stampede2 of TACC (allocation provided through the NSF ACCESS program).

Table 5.2: Effect of implant position on VF vibration frequency and amplitude following 3D FSI simulation.

Implant location	Implant side VF vibration frequency (Hz)	Implant side VF amplitude (mm)
Group 1 (insertion depth 2 mm)		
Baseline	686	0.04
SS+1	626	0.061
SS-1	649	0.057
AP+1	700	0.105
AP-1	652	0.035
SS+2	643	0.059
SS-2	595	0.02
AP+2	693	0.053
AP-2	667	0.025
Group 2 (insertion depth 3 mm)		
Baseline	769	0.11
SS+1	654	0.1
SS-1	693	0.03
AP+1	795	0.05
AP-1	700	0.06

5.4 Results

For the quasi-static simulation of the implant medialization, we evaluated the degree of VF adduction by measuring: (1) the glottal area, (2) displacement at the mid-point of the VF length, and (3) curvature of the displaced medial surface. All three variables were measured in a plane cutting through the narrowest section of the VF shown in Figure 5.2. In general, more displacement and a smaller glottal area correspond to a greater extent of medialization, which is more helpful for flow-induced vibration. The results of these variables for all fourteen cases considered in this study are presented in Table 5.1.

For the subsequent FSI simulations, we obtained the VF vibration frequency and amplitude of the implant side for each case. The results are presented in Table 5.2. The following sections discuss the detailed effects of the implant position and depth.

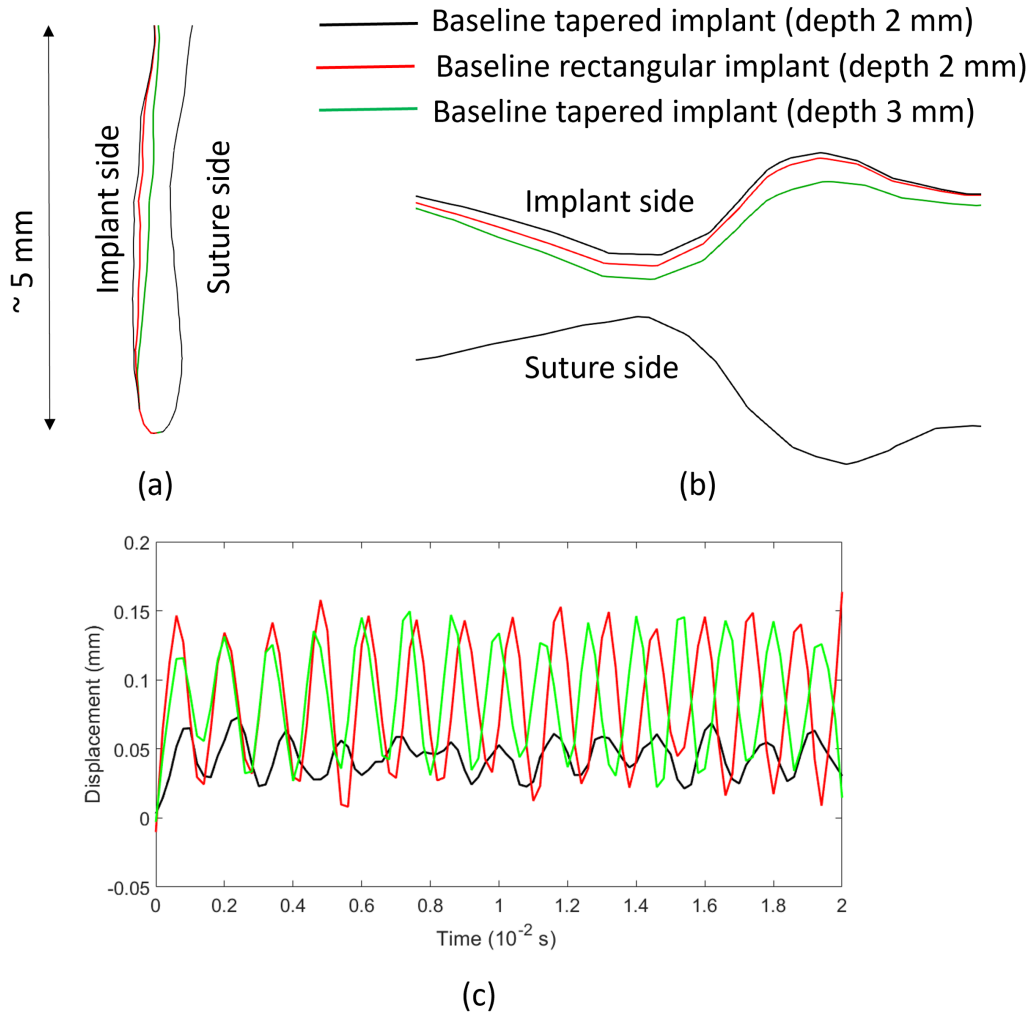

Figure 5.4: Effect of implant shape and insertion depth. (a) 2D shape of the glottis viewed in the cut plane shown in Figure 5.2(a). (b) 2D shape of the lumen surface viewed in the coronal plane cut through the midpoint of the VF. (c) Displacement of the VF in the FSI simulation. The rectangular-shaped implant was used in the study in Chapter 4.

5.4.1 Effect of implant shape and depth for baseline position

We first discuss the effects of the implant shape and insertion depth for the baseline position.

Figures 5.4(a) and (b) show the glottal outline in the transverse and coronal views, respectively (refer to Figure 5.2 for locations of the view planes). Comparing with the rectangular implant whose insertion depth is 2 mm, the tapered implant with insertion of 2 mm has a reduced VF displacement at the medial surface (0.29 mm vs. 0.43 mm at the VF mid-point). This is because the anterior edge of the implant is shorter and has only been inserted by 1 mm, thus displacing less tissue volume. Increasing the depth to 3 mm for the tapered implant produced more displacement than the rectangular implant. As anticipated, the 3-mm depth results in the highest glottal closure among the three cases in terms of the glottal area, measuring at 5.7 mm^2.

Importantly, implant insertion induces a 3D glottal displacement, as evident in Figure 5.4 (b), where the implant has caused significant displacement in both subglottal and supraglottal regions. The subglottal displacement may have an impact on the glottal flow.

As the tapered implant depth is increased from 2 mm to 3 mm, the curvature radius of the glottis on the implant side has changed from 32 mm to 73.5 mm, and the outline of the glottis has changed from a concave shape to a convex shape. As a reference, the rectangular implant case has a curvature radius of 133 mm and has a concave shape. Generally, the greater the curvature radius is, the more uniform the VF displacement is along the longitudinal direction. This observation underscores the significance of the implant shape and insertion depth in achieving not only local glottal displacement but also glottal curvature characteristics that are closer to those of healthy VFs.

Comparing VF vibration for the implant-medialized side, as depicted in Figure 5.4(c), the tapered implant with 2-mm depth demonstrates the lowest vibration frequency and amplitude among the three cases. Increasing the implant depth to 3 mm has significantly improved the vibration amplitude. On the other hand, the vibration frequency has increased

from 686 Hz for the 2-mm depth to 769 Hz for the 3-mm depth. The rectangular implant shows the greatest vibration amplitude (0.15 mm) among all three cases. For the tapered implant, the 3-mm depth has led to significant improvement as compared to the 2-mm depth.

As seen in these comparisons, the implant shape and insertion depth have to be considered at the same time to achieve significant vibrations of the VF. Furthermore, more displacement of tissue volume does not necessarily produce greater VF vibration, as seen by comparing the tapered implant with a 3-mm depth and the rectangular implant with a 2-mm depth (the former implant has more volume displacement).

5.4.2 Effect of implant shifting toward the supraglottal direction

Building upon the previous analysis, we now examine the effects of implant position variations towards the supraglottal direction (SS-), i.e., shifting up along the axial direction from the baseline position. Four cases are considered here for comparison: baseline, SS-1, and SS-2, with all three at 2 mm depth, and SS-1 at 3 mm depth.

The implant SS-1 with 2 mm depth demonstrates a static VF displacement at the midpoint that is comparable to the baseline case with the same depth (0.3 mm and 0.29 mm, respectively). As illustrated in Figure 5.5(a,b), the glottal shape at the narrowest section has little change either in the axial plane or in the coronal plane. Further increasing the SS-1 implant insertion depth to 3 mm only slightly changed the shape in the coronal view; in the axial view, there is almost no visible change to the glottal shape.

In comparison, shifting the implant further, as in SS-2, reduces the VF medialization as seen from the glottal outlines. The quantitative information is detailed in Table 5.1. From Figure 5.5(b), in this case there are significant tissue displacements in the supraglottal region where the false vocal fold (FVFs) is. Thus, the supraglottal region becomes more asymmetric.

Figure 5.5(c) shows the vibration amplitude of the implant side for these four cases.

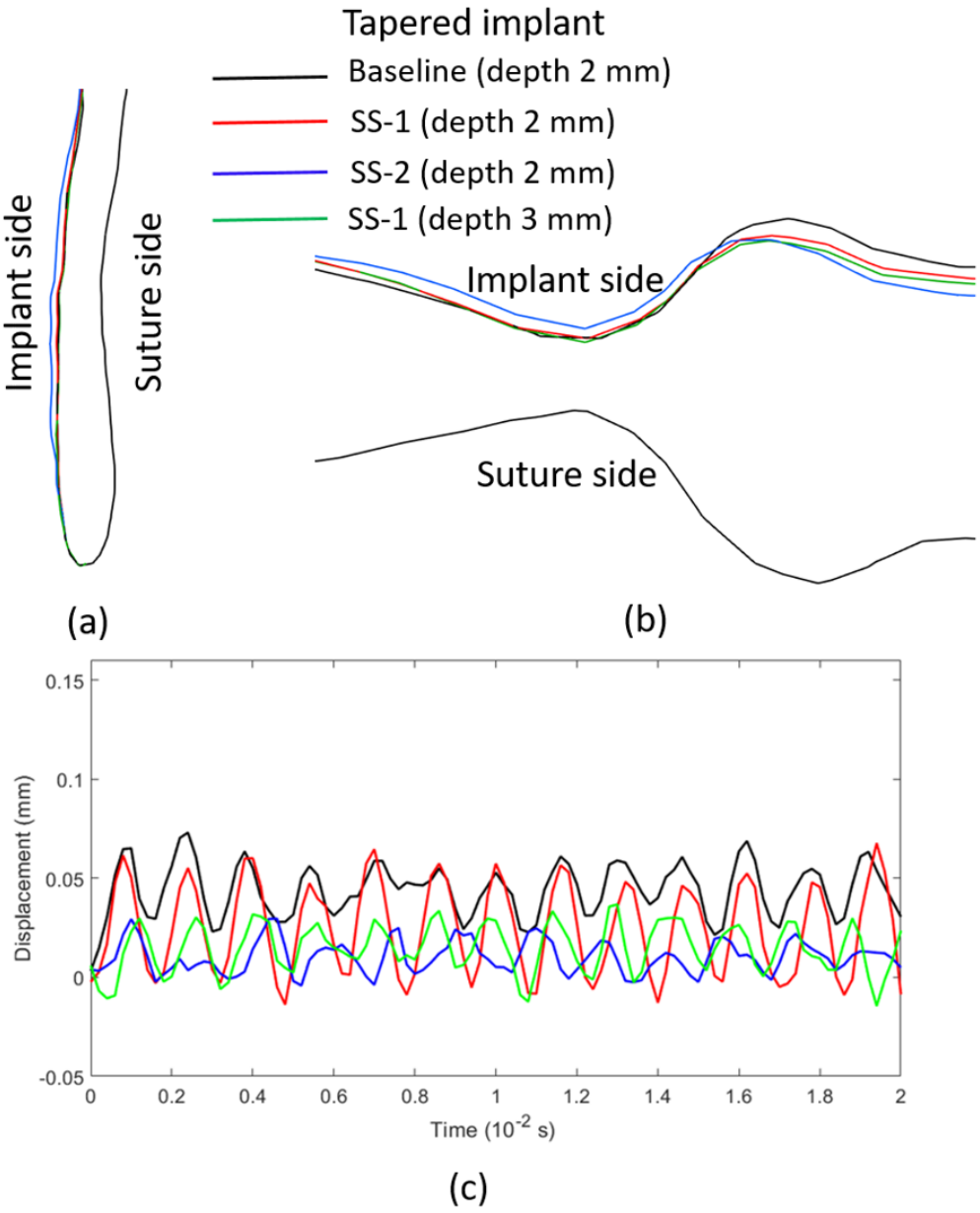

Figure 5.5: Effect of the implant shifting in the supraglottal direction. (a) and (b) Glottal outlines in the axial view and coronal view, respectively. (c) Vibration of the implant side as measured at the mid-point.

Compared to the baseline position, SS-1 has significantly improved vibration, suggesting that some shift in the superior direction is favorable without much difference in their vibration frequencies (approximately 5% different). However, increasing the insertion depth to 3 mm for the same SS-1 position only results in a higher VF vibration frequency (693 Hz vs. 649 Hz) but has reduced the vibration amplitude to nearly half.

Note that the static displacements of medialization for these three cases are very close to one another. However, their vibration amplitudes are quite different. Another observation I that for the baseline case, the mean displacement of the VF during oscillation is the greatest among these cases, but its amplitude is not necessarily greater than the other cases. These results highlight the importance of evaluating the performance of implant medializaton using the vibration characteristics as criteria in addition to the degree of medialization.

Figure 5.5(c) shows that shifting the implant further in the supraglottal direction, i.e., the SS-2 case, does not help with the vibration. The amplitude is actually reduced as compared with SS-1.

5.4.3 Effect of implant shifting toward the subglottal direction

We now examine the effects of implant position variations towards the subglottal direction (SS+), i.e., shifting downward along the axial direction from the baseline position. Four cases are considered here for comparison: baseline, SS+1, and SS+2, with all three at 2 mm depth, and SS+1 at 3 mm depth.

The case of SS+1 with 2 mm depth yields VF displacements (0.27 mm) that are close to the baseline (0.29 mm), as shown by the outlines in Figure 5.6(a,b). In contrast, SS+2 exhibits reduced VF displacements in the glottis region as compared to the baseline. On the other hand, SS+2 results in significantly larger displacements in the subglottal region. With a deeper implant insertion to 3 mm, the SS+1 case shows increased VF displacements in the glottal region (0.36 mm at the mid-point of the VF) compared to the other three cases, and the subglottal region also becomes narrower. Furthermore, this case displays an

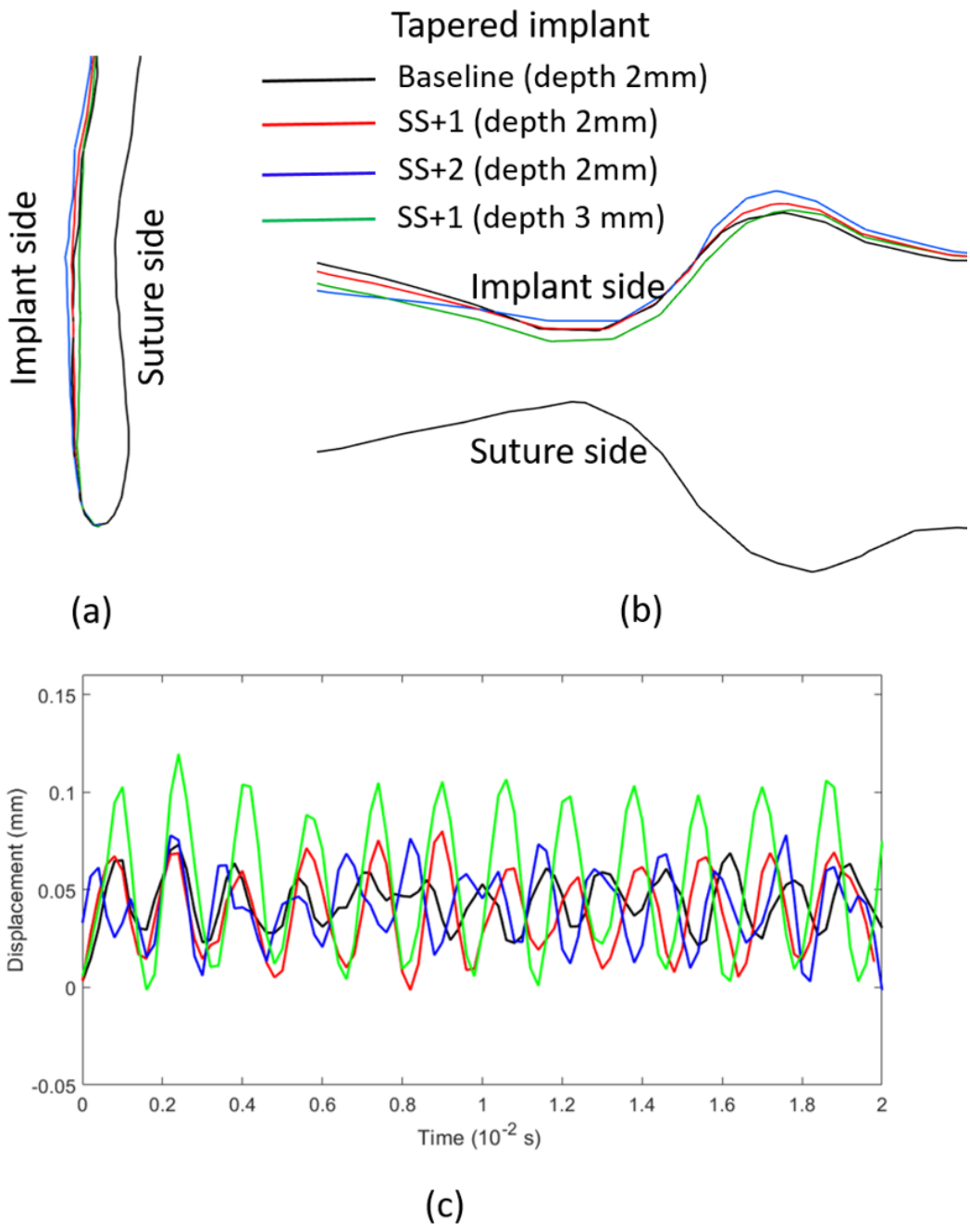

Figure 5.6: Effect of implant shifting in the subglottal direction. (a) and (b) Glottal outlines in the axial view and coronal view, respectively. (c) Vibration of the implant side as measured at the mid-point.

improved VF curvature radius, as outlined in Table 5.1.

The vibration of the implant side has a lower vibration frequency for all three SS+ cases compared to the baseline (refer to Table 5.2). However, their vibration amplitudes are all greater than the baseline case as shown in Figure 5.6(c).

Note that the implant cannot be further shifted toward the subglottal direction since the implant window would be too close to the inferior edge of the thyroid cartilage.

5.4.4 Effect of implant shifting toward the anterior direction

Now we consider the effects of implant position variations towards the anterior direction (AP+). Four cases are included here for comparison: baseline, AP+1, and AP+2, with all three at 2 mm depth, and AP+1 at 3 mm depth.

All three cases (AP+1, AP+2, and AP+1 with 3 mm depth) resulted in improved glottal closure compared to the baseline position (refer Table 5.1). This effect is evident from the glottal outlines in Figure 5.7(a,b). Comparing AP+1 and AP+2, both at 2 mm depth, AP+1 has slightly better displacements in the glottal region as seen in Figure 5.7(b). This is attributed to the implant apex in the AP+1 position prominently influencing the midsection of the VF. In contrast, for the AP+2 case, the implant is too close to the anterior commissure, and the anterior implant edge has a minimal effect on VF displacement.

It is worth pointing out that for the AP+1 case, even with a 2 mm insertion depth the current tapered implant produces a narrowed glottal area that is comparable to the rectangular implant from Chapter 4 (5.9 mm^2 vs. 6 mm^2 after medialization). The current implant is advantageous because it displaces less tissue volume than the rectangular implant but still leads to a similar degree of medialization in terms of area reduction.

Increasing the implant depth to 3 mm for AP+1 results in even more medialization. The glottal outlines show that in this case, the VF has significant displacements in both the glottal region and the subglottal region. Another observation from Figure 5.7(a) and Table 5.1 is about the VF curvature radius and shape in the axial plane. All three cases

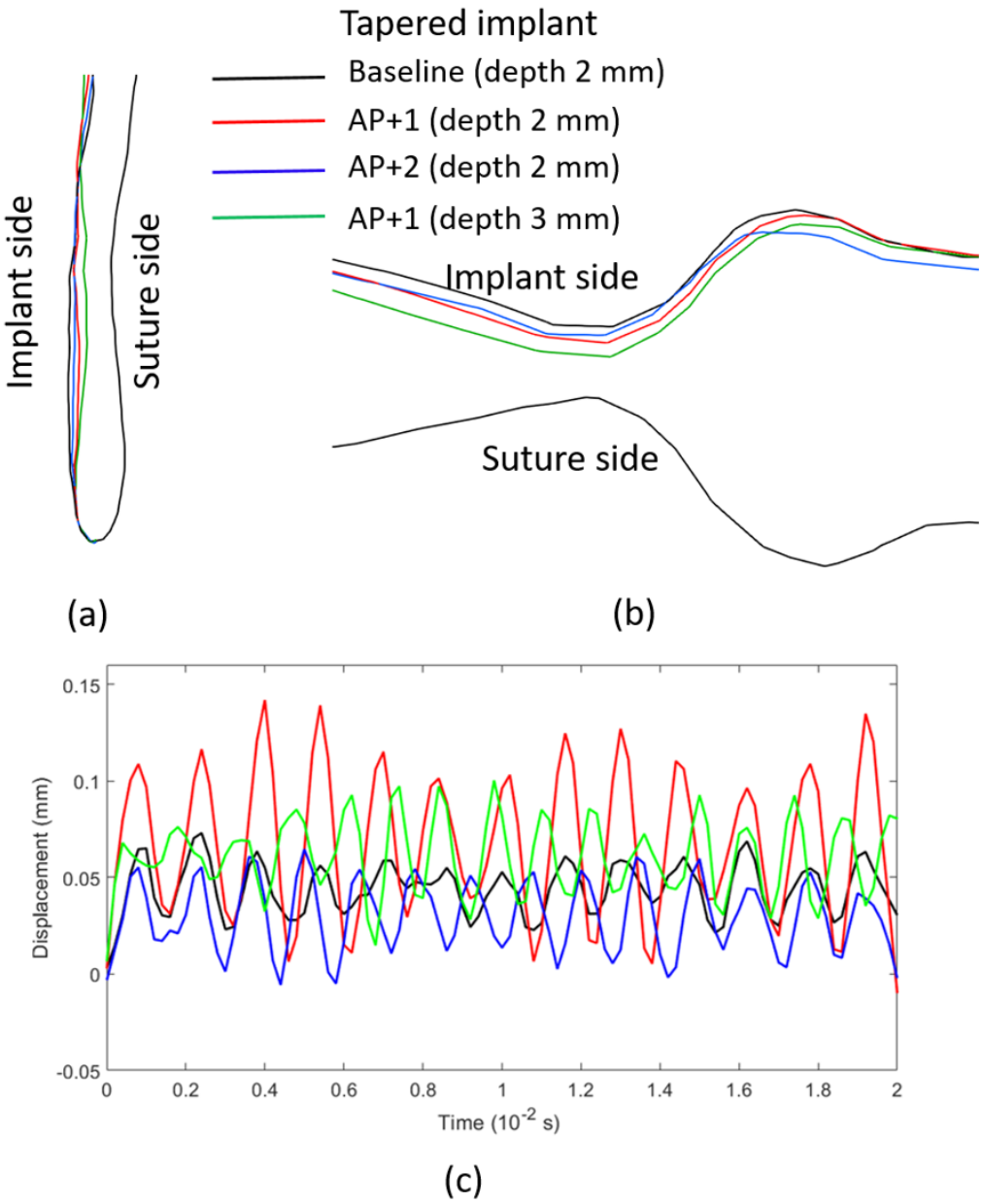

Figure 5.7: Effect of the implant shifting in the anterior direction. (a) and (b) Glottal outlines in the axial view and coronal view, respectively. (c) Vibration of the implant side as measured at the mid-point.

of anterior shift exhibit a convex shape on the implant side. While the AP+1 (2 mm) and AP+2 cases have a larger curvature radius, the AP+1 (3 mm) case shows a smaller curvature radius, indicating a more localized medialization.

For the vibration characteristics, the three cases with 2 mm depth (baseline, AP+1, AP+2) have similar frequencies (Table 5.2). However, their vibration magnitudes are quite different, with AP+1 showing the greatest magnitude and the baseline showing the lowest amplitude, as seen from Figure 5.7(c).

When the insertion depth is increased to 3 mm, we observe that the vibration frequency for AP+1 increases, while the vibration amplitude decreases. These results suggest the VF has become stiffer following implant medialization.

5.4.5 Effect of implant shifting toward the posterior direction

Figure 5.8(a,b) shows the glottal outlines in the axial and coronal planes for the implant positions shifting toward the posterior direction. This comparison group includes the baseline, AP-1, AP-2 at 2 mm depth, and AP-1 at 3 mm depth.

Compared to the baseline case, AP-1 and AP-2 at 2 mm depth yield a decreased VF displacement of 0.23 mm and 0.18 mm, respectively, at the mid-point. Further inspection of the implant location shows that the implant at these positions interacts with the arytenoid cartilage and has a weaker direct effect on the VF displacement. As a result, they produce less medialization than the baseline. Additionally, the VF curvature radius for AP-1 and AP-2 are low (Table 5.1), and the glottis maintains a concave shape in the axial view.

AP-1 at 3 mm depth displays a slight improvement in the displacement at the mid-point (0.3 mm) compared to the baseline (0.29 mm) and in the glottal closure (6.2 mm^2 in the area) than the baseline (6.5 mm^2). This enhanced glottal closure is attributed to the medial displacement of the arytenoid cartilage due to implant insertion, indicating a stronger implant-arytenoid interaction.

AP-1 with 2 mm depth shows comparable vibration frequency (652 Hz) and amplitude

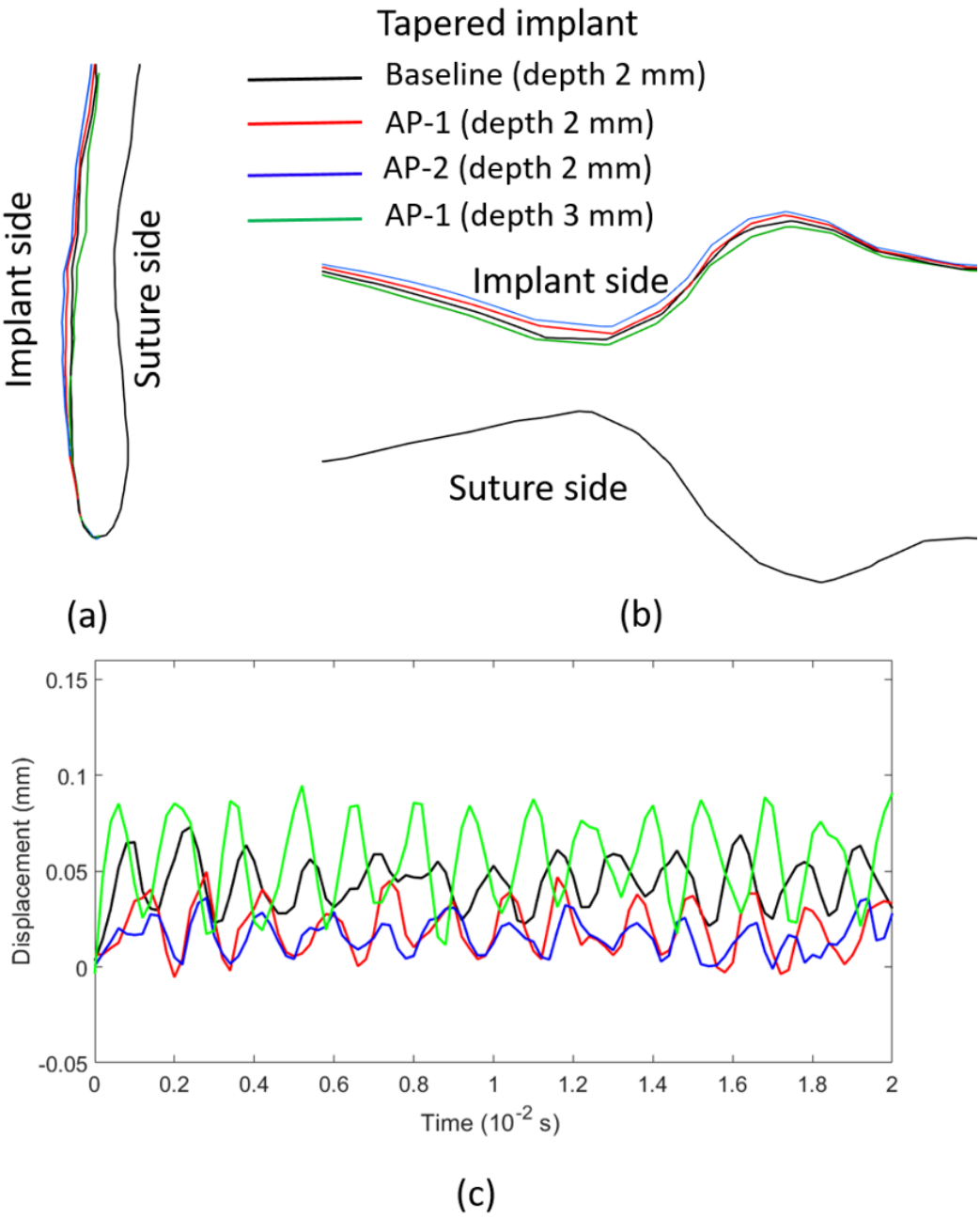

Figure 5.8: Effect of the implant shifting in the posterior direction. (a) and (b) Glottal outlines in the axial view and coronal view, respectively. (c) Vibration of the implant side as measured at the mid-point.

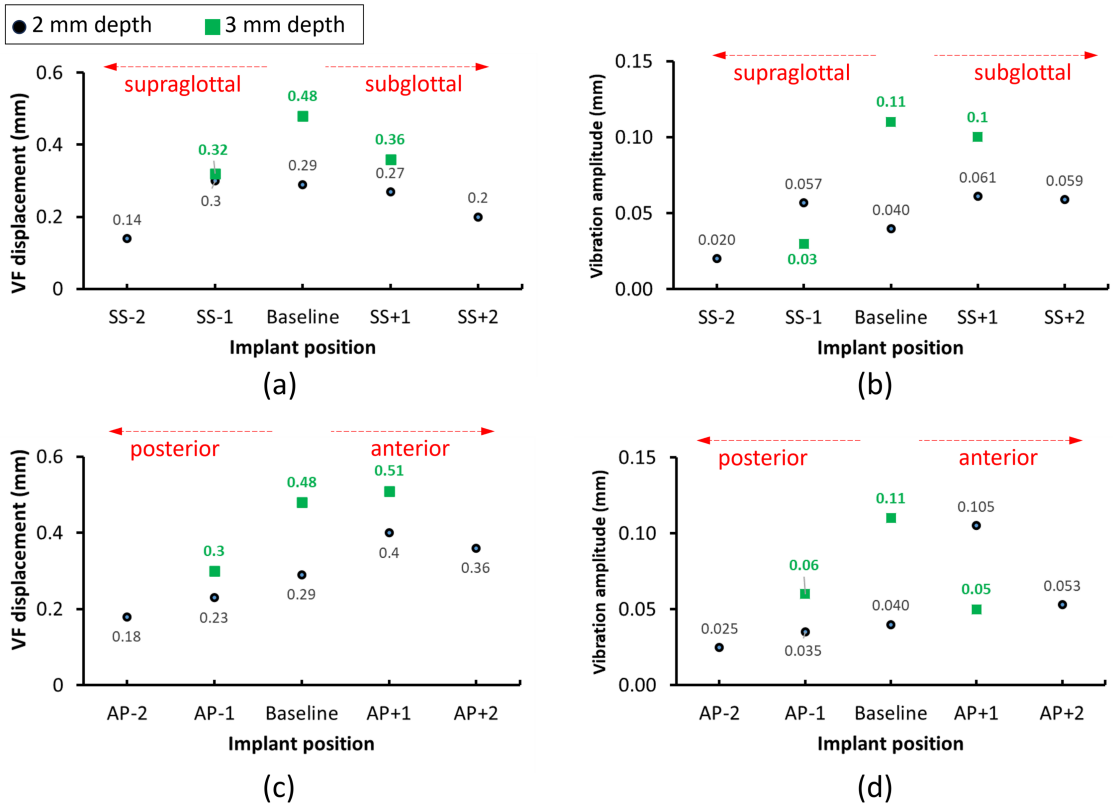

Figure 5.9: Comparing the VF displacement (a,c) and vibration frequency (b,d) for supraglottal-subglottal (SS) variations (a,b) and for anterior-posterior (AP) variations.

(0.035 mm) to the baseline. In comparison, for AP-2 the vibration frequency and amplitude are 667 Hz and 0.025 mm, respectively; thus, its magnitude is significantly lower than AP-1. AP-1 with 3 mm depth exhibits both elevated vibration frequency (700 Hz) and increased amplitude (0.06 mm) compared to its corresponding 2 mm depth case and the baseline.

5.5 Discussions

5.5.1 Comparison of all cases considered

All the cases considered in this Chapter are grouped in Figure 5.9 according to the supraglottal-subglottal variations or the anterior-posterior variations. We compare the VF displacement that is measured at the mid-point of the VF and vibration frequency. This figure shows that if we fix the implant shape and insertion depth, then there is generally an optimal implant location for the greatest VF displacement and an optimal implant location for the greatest

vibration amplitude. These two optimal locations are not necessarily the same, as the figure shows. For example, at 3 mm depth and along the AP direction, the AP+1 location has the greatest VF displacement, but the baseline case has the greatest vibration amplitude. Therefore, using the simulation of medialization to generate the results for the assessment of surgery would not be sufficient, and one should perform FSI simulation as well to predict the effect of the implant on vibration.

Overall, the implant position with a 1 mm shift from the baseline exhibits better medialization and vibration characteristics as compared to the position with a 2 mm shift in the same direction. Therefore, mm-scale adjustments of the implant location would be significant for outcome improvement.

Increasing the insertion depth from 2 mm to 3 mm generally results in more VF displacement and better glottal closure. Also, raising implant insertion depth consistently increases vibration frequency. However, its impact on amplitude varies depending on the implant location.

Although in this study we have focused primarily on the effects of the implant location and depth, the tapered shape effect could be compared with the rectangular shape used in Chapter 4. All the cases with the tapered shape have a lower vibration amplitude than the rectangular shape at the baseline location and with a 2 mm depth.

In summary, the implant location, depth, and shape are all important in the vibration of the VF and should be considered together during optimization. This explains the lack of consensus on the optimal implant shape in various studies (Orestes et al., 2014; Zhang et al., 2015; Reddy et al., 2022; Movahhedi et al., 2021), when the shape is considered alone.

5.5.2 Relevance of current results to previous experiment studies

Based on the anatomy of the larynx and underlying physical principle for flow-induced VF vibration, it is understandable that the implant positioning is important for type-1 thyro-

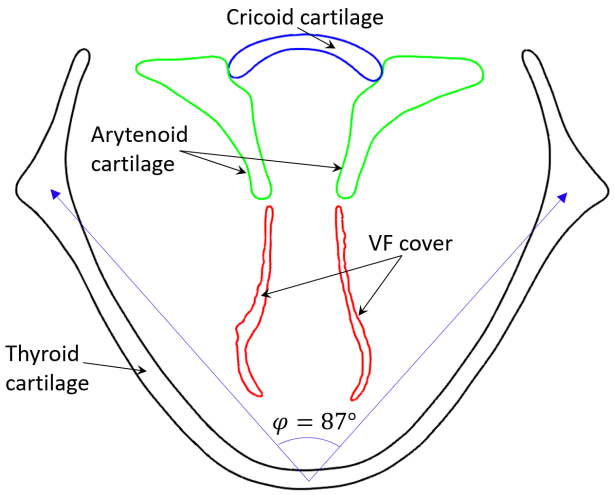

Figure 5.10: Outlines of the laryngeal components in the current model indicating the thyroid angle φ.

plasty to work. Indeed, many studies have emphasized the crucial importance of implant positioning in type-1 thyroplasty surgery in humans (Laccourreye et al., 2021; Desuter et al., 2017; Orestes et al., 2014; Maragos, 2001; Iwahashi et al., 2015). However, there is no single location that could be used for all patients given the unique laryngeal features of each individual patient.

Studies by Desuter et al. (2020) and Rapoport and Courey (2022) have advocated for placing the implant window in the inferior region of the thyroid cartilage for humans. This recommendation is further supported by Laccourreye et al. (2021), who suggested that optimal implant placement should be as anterior and inferior as possible to minimize the risk of arytenoid cartilage tilt and associated respiratory complications. In our computational study of the rabbit larynx, the AP+1 and SS+1 positions from Group 1 (2mm depth) yield favorable vibratory characteristics and are generally consistent with the previous studies.

A crucial parameter, the thyroid angle (φ), represents the angle between the two laminae of the thyroid cartilage. It serves as a distinctive identifier of larynx shape and is depicted in Figure 5.10. Multiple studies have discussed the significance of the thyroid angle and thyroid cartilage shape in the type-1 thyroplasty surgical planning (Desuter et al.,

2017; Aronson and Bless, 2009; Blake Simpson and Sulica, 2006). A larger thyroid angle necessitates deeper implant insertion compared to a smaller thyroid angle at a specific landmark position on the thyroid cartilage(Desuter et al., 2017). Females typically exhibit wider thyroid cartilages and higher thyroid angles, with a mean of 91° for women vs. a mean of 77° for men (Desuter et al., 2017). This necessitates generally distinct implant locations and sizes for males and females.

In our subject-specific geometric model, the thyroid angle is 87°. Consequently, placing an implant window towards the posterior results in a greater distance between the implant and the medial surface. On the other hand, an anterior location would allow the implant to have a shorter distance to the medial surface and affect the surface displacement more. This explains that in our study, the AP+1 location has achieved the most VF displacement. Overall, our computational study supports the previous findings about the impact of thyroid angle on medialization. Patients with higher thyroid angles may benefit from implants with a greater insertion depth.

Finally, experimental findings by Noordzij et al. (1998) and Orestes et al. (2014) on canine larynges emphasize that the optimal implant shape is contingent on the insertion depth, while no single best implant shape fits everyone. In agreement with this, our study demonstrates that the implant shape should be considered along with other variables such as position and depth. Therefore, a broader optimization than the current study considering all these parameters would be necessary in the future for patient-specific design.

5.6 Chapter conclusion

Using computational FSI modeling, we have investigated the optimal implant position and depth for type-1 thyroplasty. A subject-specific laryngeal model, based on rabbit MRI data, was used to generate different implant positions along the axial and anterior-posterior axes in addition to the insertion depth. We have used both the VF displacements and vibration amplitude as criteria to assess the performance of the implant. The results show that the

optimal implant for vibration is not necessarily the same optimal implant for maximal VF displacements. Thus, FSI modeling is needed besides the modeling of medialization to predict the comprehensive effects of the implant in type-1 thyroplasty. Our computational modeling predictions are aligned with existing experimental data from previous studies, and the findings emphasize the importance of subject-specific considerations in type-1 thyroplasty planning and the need to include the location, depth, and shape parameters together during implant optimization.

CHAPTER 6

Conclusion and future work

6.1 Lessons and conclusions from this research

In this dissertation, we have worked with our collaborators to carry out an integrated computational/experimental study and explore the feasibility of using computational modeling of phonation to perform surgical planning for type-1 thyroplasty. All the experimental work was done by Dr. Rousseau's group, which included animal samples, MRI scans, surgeries, and phonation tests. I personally was responsible for all the computational modeling-related work, which included image segmentation, model construction, model simulations, flow and tissue visualization, data processing, etc, unless otherwise noted. Given the nature of integrated research, the conclusion and future work are given here for experiment and computational modeling together.

To our knowledge, this was the first attempt to combine experiment and computational modeling to build subject-specific phonation models, predict the effects of the implant in type-1 thyroplasty, and validate the computational model. We have taken logical steps to advance the overall objective. First, we studied healthy phonation and validated the FSI model by an *in vivo* phonation experiment. Then, we studied the diseased/UVFP condition and the implant-medialized VF condition, and we validated by an *ex vivo* experiment. Lastly, we used the implanted model and performed an optimization study to test the capability of computationally determining the optimal implant placement in a virtual surgery. Although the outcome of the optimization was not compared with any experiment, the study itself still relied on experimental data (e.g., MRI scan) to build the subject-specific model.

Since they relied on each other, the experimental and computational tasks had to be well coordinated in the process, and the workflow depended on the specific objective of the

study. For example, in Chapter 3 where we studied healthy phonation, since the VF adduction was not part of the primary focus and we were mainly interested in the FSI modeling of the vibration, the computational models were built on the postoperative scan. However, in Chapter 4 where we studied UVFP and type-1 thyroplasty, the effects of implant medialization were part of the investigation and had to be modeled; therefore, the computational models were built on the preoperative scan (the exact implant and suture locations were still taken from the postoperative scan to ensure the consistency between the model and the experiment). To determine the optimal placement of the implant for surgical planning, the model in Chapter 5 was naturally built on the preoperative scan.

In order to match the experimental results and validate the computational models, several issues had to be considered in this research. First, in addition to the subject-specific laryngeal anatomy that could be built from 3D scans, subject-specific tissue properties should be incorporated as well for the individual samples. Typically, these properties are not available and thus have to be estimated. In this project, we have shown that simple computational models, e.g., eigenmode analysis and 1D flow-based fast FSI simulations, could be used for that purpose. With this step, the resulting model may match the experiment much better than one that merely adopts material properties from population data. Second, the tissue separation due to medialization should also be incorporated to correctly capture the VF displacement at the medial surface and subsequently VF vibration in the FSI simulation.

Through the model simulation, we gained important information regarding physical insight into the FSI processes of healthy, diseased, and surgically altered phonation. For example, the subglottal shape of the VF has a significant effect on the energy transfer between the flow and the tissue. The inclined orientation of the VF in the larynx has a large impact on the airflow through the glottis and in the supraglottal region. The false vocal fold helps maintain the flow symmetry and is instrumental for VF vibration. In addition to vibration frequency and amplitude, the implant placement also affects the glottal flow

characteristics. A better implant placement not only leads to greater vibration amplitude of the VF but also produces a more pulsatile flow and greater flow efficiency. Finally, the optimal placement of the implant should be highly subject-specific and depends on many factors of the individual such as the 3D vocal fold shape and the shape of the thyroid cartilage. This feature underscores the need to use computational modeling to determine the implant placement for individual patients.

Overall, the present research investigated the potential application of computational modeling to enhance the efficacy of the type-1 thyroplasty procedure. This interdisciplinary exploration involved a concerted effort between engineers and medical scientists, and it encompassed animal experimental design, image processing, and computational modeling and simulation. The results from this research have shown computational modeling of phonation could be a promising tool for pre-surgical planning.

6.2 Limitations of present research and future work

Although the integrated study in this research represents a significant contribution toward the development of a computational modeling-based tool for surgical planning of type-1 thyroplasty, there are a few important limitations in our work, which lead to directions of the future work as described below.

6.2.1 Validation of the model-based optimization

Due to limited resources, the optimized implant placement was not validated in the experiment. In the future, the resulting implant, including its placement and shape parameters, could be tested using the same larynx sample that the model is built upon. Such a study would prove the reliability of the model-based optimization.

Another kind of and very important validation is to demonstrate that the computational models can indeed provide useful guidance for the surgical procedure as compared to the current standard procedure without using model-based guidance. Recently, our group (Li et al., 2023) demonstrated that the preoperative modeling of medialization led to a better

outcome (in terms of the degree of medialization) as compared to the procedure by the same surgeon without relying on the model prediction. A similar study could be done to validate the FSI modeling and optimization. This type of study needs special considerations to design the workflow to coordinate the experimental and computational tasks, and to eliminate all kinds of potential human biases.

6.2.2 Integration of *in vivo* experiment and computational models

In Chapter 4, we only considered *ex vivo* animal experiment where the excised larynx was used for MRI scan, medialization, and phonation test. Preferably an *in vivo* experiment of live animals would be used to develop and evaluate the capability of the computational model. To conduct such an experiment, the modality and protocols of scans will have to be redesigned. Furthermore, the type-1 thyroplasty procedure on the animal including the implant medialization and the "healthy side" medialization would have to be explored. For the computational side, not much has to be changed. As long as the preoperative and postoperative scans are available and have sufficient resolution, the same method as described in this dissertation can be used to build the FSI model and to perform model simulation.

6.2.3 Combining multi-fidelity models for implant optimization

In Chapter 5, we employed 3D FSI simulations to perform the model-based optimization for the implant placement. This approach is extremely computationally expensive and not suitable in practice if a large parameter space is considered and if limited time is available in reality for surgical planning purposes. Fortunately, we have developed multi-fidelity models that could be combined to reduce the computational cost and accelerate the optimization process. For example, we may use the 1D-flow coupled with 3D FEM tissue model to perform fast FSI simulations as done recently by our group (Li et al., 2021a). The high-fidelity, full 3D FSI models like the ones in this dissertation could be used for limited search or for verification of the low-fidelity model-based search. In addition, parallel

searches could be conducted in the parameter space using modern computing resources.

6.2.4 Moving to human study

Finally, only animal study was used in this dissertation. Moving to a study of live human subjects will certainly have additional challenges. For example, modality and protocols of scans, turnaround time of model-based optimization, *in vivo* phonation and flow measurements, etc, will all have to be carefully considered in addition to the obvious safety issues related to human study.

References

Alipour, F., Berry, D. A., and Titze, I. R. (2000). A finite-element model of vocal-fold vibration. *The Journal of the Acoustical Society of America*, 108(6):3003–3012.

Alipour, F., Scherer, R., and Knowles, J. (1996). Velocity distributions in glottal models. *Journal of Voice*, 10(1):50–58.

Andrews, B. T., Van Daele, D. J., Karnell, M. P., McCulloch, T. M., Graham, S. M., and Hoffman, H. T. (2008). Evaluation of open approach and injection laryngoplasty inrevision thyroplasty procedures. *Otolaryngology–Head and Neck Surgery*, 138(2):226–232.

Aronson, A. and Bless, D. (2009). Normal voice development. *Clinical voice disorders*, 3.

Avhad, A., Li, Z., Wilson, A., Sayce, L., Chang, S., Rousseau, B., and Luo, H. (2022). Subject-specific computational fluid-structure interaction modeling of rabbit vocal fold vibration. *Fluids*, 7(3):97.

Bauer, H. and König-Heidelberg, W. (1967). Physikalische und histologische untersuchungen an normalen und einem weiblichen virillsierten kehlkopf. *Archiv für klinische und experimentelle Ohren-, Nasen-und Kehlkopfheilkunde*, 188:358–363.

Berry, D. A., Reininger, H., Alipour, F., Bless, D. M., and Ford, C. N. (2005). Influence of vocal fold scarring on phonation: Predictions from a finite element model. *Annals of Otology, Rhinology & Laryngology*, 114(11):847–852.

Blake Simpson, C. and Sulica, L. (2006). Principles of medialization laryngoplasty. *Vocal fold paralysis*, pages 135–143.

Cameron, B. H., Zhang, Z., and Chhetri, D. K. (2020). Effects of thyroplasty implant stiffness on glottal shape and voice acoustics. *Laryngoscope investigative otolaryngology*, 5(1):82–89.

Chan, R. W., Fu, M., Young, L., and Tirunagari, N. (2007). Relative contributions of collagen and elastin to elasticity of the vocal fold under tension. *Annals of biomedical engineering*, 35(8):1471–1483.

Chang, S. (2016). *Computational Fluid-structure Interaction for Vocal Fold Modeling*. PhD thesis, Vanderbilt University.

Chang, S., Novaleski, C. K., Kojima, T., Mizuta, M., Luo, H., and Rousseau, B. (2015). Subject-Specific Computational Modeling of Evoked Rabbit Phonation. *Journal of Biomechanical Engineering*, 138(1):011005.

Chang, S., Tian, F.-B., Luo, H., Doyle, J. F., and Rousseau, B. (2013). The role of finite displacements in vocal fold modeling. *Journal of Biomechanical Engineering*, 135(11):111008.

Chen, Y., Li, Z., Chang, S., Rousseau, B., and Luo, H. (2020). A reduced-order flow model for vocal fold vibration: from idealized to subject-specific models. *Journal of Fluids and Structures*, 94:102940.

Chen, Y. and Luo, H. (2020). Pressure distribution over the leaflets and effect of bending stiffness on fluid–structure interaction of the aortic valve. *Journal of Fluid Mechanics*, 883.

Cohen, J. T., Bates, D. D., and Postma, G. N. (2004). Revision gore-tex medialization laryngoplasty. *Otolaryngology—Head and Neck Surgery*, 131(3):236–240.

Cook, D. D. and Mongeau, L. (2007). Sensitivity of a continuum vocal fold model to geometric parameters, constraints, and boundary conditions. *The Journal of the Acoustical Society of America*, 121(4):2247–2253.

Daniero, J. J., Garrett, C. G., and Francis, D. O. (2014). Framework surgery for treatment of unilateral vocal fold paralysis. *Current otorhinolaryngology reports*, 2:119–130.

Desuter, G., Cartiaux, O., Pierard, J., Henrard, S., van Lith-Bijl, J., van Benthem, P. P., and Sjögren, E. (2020). Accuracy of thyroid cartilage fenestration during montgomery medialization thyroplasty. *Journal of Voice*, 34(4):609–615.

Desuter, G., Henrard, S., Van Lith-Bijl, J. T., Amory, A., Duprez, T., van Benthem, P. P., and Sjögren, E. (2017). Shape of thyroid cartilage influences outcome of montgomery medialization thyroplasty: a gender issue. *Journal of Voice*, 31(2):245–e3.

Döllinger, M., Kniesburges, S., Berry, D. A., Birk, V., Wendler, O., Dürr, S., Alexiou, C., and Schützenberger, A. (2018). Investigation of phonatory characteristics using ex vivo rabbit larynges. *The Journal of the Acoustical Society of America*, 144(1):142–152.

Francis, D. O., McKiever, M. E., Garrett, C. G., Jacobson, B., and Penson, D. F. (2014). Assessment of patient experience with unilateral vocal fold immobility: a preliminary study. *Journal of voice*, 28(5):636–643.

Ge, P. J., French, L. C., Ohno, T., Zealear, D. L., and Rousseau, B. (2009). Model of evoked rabbit phonation. *Annals of Otology, Rhinology & Laryngology*, 118(1):51–55.

George, N. A., de Mul, F. F., Qiu, Q., Rakhorst, G., and Schutte, H. K. (2008). Depth-kymography: high-speed calibrated 3d imaging of human vocal fold vibration dynamics. *Physics in Medicine & Biology*, 53(10):2667.

Hara, H., Hori, T., Sugahara, K., and Yamashita, H. (2014). Surgical planning of isshiki type i thyroplasty using an open-source digital imaging and communication in medicine viewer osirix. *Acta oto-laryngologica*, 134(6):620–625.

Henrich, N., Sundin, G., Ambroise, D., d'Alessandro, C., Castellengo, M., and Doval, B. (2003). Just noticeable differences of open quotient and asymmetry coefficient in singing voice. *Journal of Voice*, 17(4):481–494.

Hiramatsu, H., Tokashiki, R., and Suzuki, M. (2008). Usefulness of three-dimensional computed tomography of the larynx for evaluation of unilateral vocal fold paralysis before and after treatment: technique and clinical applications. *European archives of oto-rhino-laryngology*, 265:725–730.

Hirano, M., Kurita, S., Nakashima, T., and Stevens, K. (1981). Vocal fold physiology. *The structure of the vocal folds*, page 33.

Hunter, E. J., Titze, I. R., and Alipour, F. (2004). A three-dimensional model of vocal fold abduction/adduction. *The Journal of the Acoustical Society of America*, 115(4):1747–1759.

Isshiki, N., Okamura, H., and Ishikawa, T. (1975). Thyroplasty type i (lateral compression) for dysphonia due to vocal cord paralysis or atrophy. *Acta oto-laryngologica*, 80(1-6):465–473.

Iwahashi, T., Ogawa, M., Hosokawa, K., Mochizuki, R., and Inohara, H. (2015). Computed tomographic assessment of the causal factors of unsuccessful medialization thyroplasty. *Acta Oto-Laryngologica*, 135(3):283–289.

Ji, M., Liu, B., Jiang, J., Hoffman, M. R., Lan, J., and Fang, J. (2022). Effect of controlled muscle activation in a unilateral vocal fold polyp setting on vocal fold vibration. *Applied sciences*, 12(23):12486.

Jiang, J. J., Diaz, C. E., and Hanson, D. G. (1998). Finite element modeling of vocal fold vibration in normal phonation and hyperfunctional dysphonia: Implications for the pathogenesis of vocal nodules. *Annals of Otology, Rhinology & Laryngology*, 107(7):603–610.

Jiang, W., Rasmussen, J. H., Xue, Q., Ding, M., Zheng, X., and Elemans, C. P. (2020). High-fidelity continuum modeling predicts avian voiced sound production. *Proceedings of the National Academy of Sciences*, 117(9):4718–4723.

Kelchner, L. N., Stemple, J. C., Gerdeman, B., Le Borgne, W., and Adam, S. (1999). Etiology, pathophysiology, treatment choices, and voice results for unilateral adductor vocal fold paralysis: a 3-year retrospective. *Journal of Voice*, 13(4):592–601.

Kelleher, J. E., Zhang, K., Siegmund, T., and Chan, R. W. (2010). Spatially varying properties of the vocal ligament contribute to its eigenfrequency response. *Journal of the mechanical behavior of biomedical materials*, 3(8):600–609.

Khosla, S., Murugappan, S., Lakhamraju, R., and Gutmark, E. (2008). Using particle imaging velocimetry to measure anterior-posterior velocity gradients in the excised canine larynx model. *Annals of Otology, Rhinology & Laryngology*, 117(2):134–144.

Koufman, J. A. (1986). Laryngoplasty for vocal cord medialization: An alternative to teflon®. *The Laryngoscope*, 96(7):726–731.

Laccourreye, O., Rubin, F., van Lith-Bijl, J., and Desuter, G. (2021). Keys to successful type-1 thyroplasty with montgomery® implant for unilateral laryngeal immobility in adults. *European annals of otorhinolaryngology, head and neck diseases*, 138(3):191–194.

Lasota, M., Šidlof, P., Kaltenbacher, M., and Schoder, S. (2021). Impact of the sub-grid scale turbulence model in aeroacoustic simulation of human voice. *Applied Sciences*, 11(4):1970.

Latifi, N., Miri, A. K., and Mongeau, L. (2014). Determination of the elastic properties of rabbit vocal fold tissue using uniaxial tensile testing and a tailored finite element model. *journal of the mechanical behavior of biomedical materials*, 39:366–374.

Leder, S. B., Suiter, D. M., Duffey, D., and Judson, B. L. (2012). Vocal fold immobility and aspiration status: a direct replication study. *Dysphagia*, 27:265–270.

Li, Z., Chen, Y., Chang, S., and Luo, H. (2020). A reduced-order flow model for fluid-structure interaction simulation of vocal fold vibration. *Journal of Biomechanical Engineering*, 142:021005.

Li, Z., Chen, Y., Chang, S., Rousseau, B., and Luo, H. (2021a). A one-dimensional flow model enhanced by machine learning for simulation of vocal fold vibration. *The Journal of the Acoustical Society of America*, 149(3):1712–1723.

Li, Z., Wilson, A., Sayce, L., Avhad, A., Rousseau, B., and Luo, H. (2021b). Numerical and experimental investigations on vocal fold approximation in healthy and simulated unilateral vocal fold paralysis. *Applied Sciences*, 11(4):1817.

Li, Z., Wilson, A., Sayce, L., Ding, A., Rousseau, B., and Luo, H. (2023). Subject-specific modeling of implant placement for type i thyroplasty surgery. *Annals of Biomedical Engineering*, pages 1–10.

Lundeberg, M. R., Flint, P. W., Purcell, L. L., McMurray, J. S., and Cummings, C. W. (2011). Revision medialization thyroplasty with hydroxylapatite implants. *Laryngoscope*, 121(5):999.

Luo, H., Dai, H., de Sousa, P. J. F., and Yin, B. (2012). On the numerical oscillation of the direct-forcing immersed-boundary method for moving boundaries. *Computers & Fluids*, 56:61–76.

Luo, H., Mittal, R., and Bielamowicz, S. A. (2009). Analysis of flow-structure interaction in the larynx during phonation using an immersed-boundary method. *The Journal of the Acoustical Society of America*, 126(2):816–824.

Luo, H., Mittal, R., Zheng, X., Bielamowicz, S. A., Walsh, R. J., and Hahn, J. K. (2008). An immersed-boundary method for flow–structure interaction in biological systems with application to phonation. *Journal of computational physics*, 227(22):9303–9332.

Maragos, N. E. (2001). Revision thyroplasty. *Annals of Otology, Rhinology & Laryngology*, 110(12):1087–1092.

Meiteles, L. Z., Lin, P.-T., and Wenk, E. J. (1992). An anatomic study of the external laryngeal framework with surgical implications. *Otolaryngology–Head and Neck Surgery*, 106(3):235–240.

Miri, A. K. (2014). Mechanical characterization of vocal fold tissue: a review study. *Journal of Voice*, 28(6):657–667.

Mittal, R., Erath, B. D., and Plesniak, M. W. (2013). Fluid dynamics of human phonation and speech. *Annual Review of Fluid Mechanics*, 45:437–467.

Mittal, R. and Iaccarino, G. (2005). Immersed boundary methods. *Annu. Rev. Fluid Mech.*, 37:239–261.

Movahhedi, M., Geng, B., Xue, Q., and Zheng, X. (2021). A computational framework for patient-specific surgical planning of type 1 thyroplasty. *JASA Express Letters*, 1(12):125203.

Nasseri, S. S. and Maragos, N. E. (2000). Combination thyroplasty and the "twisted larynx:" combined type iv and type i thyroplasty for superior laryngeal nerve weakness. *Journal of Voice*, 14(1):104–111.

Netterville, J. L., Stone, R., Civantos, F. J., Luken, E. S., and Ossoff, R. H. (1993). Silastic medialization and arytenoid adduction: the vanderbilt experience: a review of 116 phonosurgical procedures. *Annals of Otology, Rhinology & Laryngology*, 102(6):413–424.

Noordzij, J. P., Opperman, D. A., Perrault Jr, D. F., and Woo, P. (1998). The biomechanics of the medialization laryngoplasty (thyroplasty type 1) in an ex vivo canine model. *Journal of Voice*, 12(3):372–382.

Novaleski, C. K., Kojima, T., Chang, S., Luo, H., Valenzuela, C. V., and Rousseau, B. (2016). Nonstimulated rabbit phonation model: Cricothyroid approximation. *The Laryngoscope*, 126(7):1589–1594.

Oren, L., Dembinski, D., Gutmark, E., and Khosla, S. (2014). Characterization of the vocal fold vertical stiffness in a canine model. *Journal of Voice*, 28(3):297–304.

Orestes, M. I., Neubauer, J., Sofer, E., Salinas, J., and Chhetri, D. K. (2014). Phonatory effects of type i thyroplasty implant shape and depth of medialization in unilateral vocal fold paralysis. *The Laryngoscope*, 124(12):2791–2796.

Palaparthi, A., Smith, S., Mau, T., and Titze, I. R. (2019). A computational study of depth of vibration into vocal fold tissues. *The Journal of the Acoustical Society of America*, 145(2):881–891.

Paniello, R. C., Edgar, J. D., Kallogjeri, D., and Piccirillo, J. F. (2011). Medialization versus reinnervation for unilateral vocal fold paralysis: a multicenter randomized clinical trial. *The Laryngoscope*, 121(10):2172–2179.

Parker, N. P., Barbu, A. M., Hillman, R. E., Zeitels, S. M., and Burns, J. A. (2015). Revision transcervical medialization laryngoplasty for unilateral vocal fold paralysis. *Otolaryngology–Head and Neck Surgery*, 153(4):593–598.

Payr, E. (1915). Plastik am schildknorpel zur behebung der folgen einseitiger stimmbandlahmung. *Dtsch Med Wochenschr*, 43(1):65–1.

Perlman, A. L., Titze, I. R., and Cooper, D. S. (1984). Elasticity of canine vocal fold tissue. *Journal of Speech, Language, and Hearing Research*, 27(2):212–219.

Qiu, Q., Schutte, H., Gu, L., and Yu, Q. (2003). An automatic method to quantify the vibration properties of human vocal folds via videokymography. *Folia Phoniatrica et Logopaedica*, 55(3):128–136.

Rapoport, S. K. and Courey, M. S. (2022). Type i thyroplasty and arytenoid adduction: Review of the literature and current clinical practice. *International Journal of Head and Neck Surgery*, 12(4):166–171.

Reddy, N., Lee, Y., Zhang, Z., and Chhetri, D. K. (2022). Optimal thyroplasty implant shape and stiffness for treatment of acute unilateral vocal fold paralysis: Evidence from a canine in vivo phonation model. *Proc. Interspeech 2022*, pages 2273–2277.

Riede, T. and Titze, I. R. (2008). Vocal fold elasticity of the rocky mountain elk (cervus elaphus nelsoni)–producing high fundamental frequency vocalization with a very long vocal fold. *Journal of Experimental Biology*, 211(13):2144–2154.

Ruben, R. J. (2000). Redefining the survival of the fittest: communication disorders in the 21st century. *The Laryngoscope*, 110(2):241–241.

Saran, M., Georgakopoulos, B., and Bordoni, B. (2023). *Anatomy, Head and Neck, Larynx Vocal Cords*. StatPearls Publishing.

Shurtz, T. E. and Thomson, S. L. (2013). Influence of numerical model decisions on the flow-induced vibration of a computational vocal fold model. *Computers & structures*, 122:44–54.

Siu, J., Tam, S., and Fung, K. (2016). A comparison of outcomes in interventions for unilateral vocal fold paralysis: a systematic review. *The Laryngoscope*, 126(7):1616–1624.

Smith, S. L. and Thomson, S. L. (2012). Effect of inferior surface angle on the self-oscillation of a computational vocal fold model. *The Journal of the Acoustical Society of America*, 131(5):4062–4075.

Smith, S. L., Titze, I. R., Storck, C., and Mau, T. (2020). Effect of vocal fold implant placement on depth of vibration and vocal output. *The Laryngoscope*, 130(9):2192–2198.

Swanson, E. R., Ohno, T., Abdollahian, D., and Rousseau, B. (2010). Effects of raised-intensity phonation on inflammatory mediator gene expression in normal rabbit vocal fold. *Otolaryngology—Head and Neck Surgery*, 143(4):567–572.

Tao, C., Zhang, Y., Hottinger, D. G., and Jiang, J. J. (2007). Asymmetric airflow and vibration induced by the coanda effect in a symmetric model of the vocal folds. *The Journal of the Acoustical Society of America*, 122(4):2270–2278.

Thibeault, S. L., Gray, S. D., Bless, D. M., Chan, R. W., and Ford, C. N. (2002). Histologic and rheologic characterization of vocal fold scarring. *Journal of Voice*, 16(1):96–104.

Thomson, S. L., Mongeau, L., and Frankel, S. H. (2005). Aerodynamic transfer of energy to the vocal folds. *The Journal of the Acoustical Society of America*, 118(3):1689–1700.

Tian, F.-B., Dai, H., Luo, H., Doyle, J. F., and Rousseau, B. (2014). Fluid–structure interaction involving large deformations: 3d simulations and applications to biological systems. *Journal of computational physics*, 258:451–469.

Titze, I. (1994). *Principles of voice production*. Prentice-Hall, Englewood Cliffs, NJ.

Titze, I. R. (1992). Phonation threshold pressure: A missing link in glottal aerodynamics. *The Journal of the Acoustical Society of America*, 91(5):2926–2935.

Triep, M., Brücker, C., and Schröder, W. (2005). High-speed piv measurements of the flow downstream of a dynamic mechanical model of the human vocal folds. *Experiments in Fluids*, 39(2):232–245.

Tucker, H. M., Wanamaker, J., Trott, M., and Hicks, D. (1993). Complications of laryngeal framework surgery (phonosurgery). *The Laryngoscope*, 103(5):525–528.

Van den Berg, J., Zantema, J., and Doornenbal Jr, P. (1957). On the air resistance and the bernoulli effect of the human larynx. *The journal of the acoustical society of America*, 29(5):626–631.

Wilson, A., Kimball, E. E., Sayce, L., Luo, H., Khosla, S. M., and Rousseau, B. (2021). Medialization laryngoplasty: A review for speech-language pathologists. *Journal of Speech, Language, and Hearing Research*, 64(2):481–490.

Woo, J.-H., Kim, D.-Y., Kim, J.-W., Oh, E.-A., and Lee, S.-W. (2011). Efficacy of percutaneous vocal fold injections for benign laryngeal lesions: prospective multicenter study. *Acta oto-laryngologica*, 131(12):1326–1332.

Woo, P., Pearl, A. W., Hsiung, M.-W., and Som, P. (2001). Failed medialization laryngoplasty: management by revision surgery. *Otolaryngology–Head and Neck Surgery*, 124(6):615–621.

Wu, L. and Zhang, Z. (2016). A parametric vocal fold model based on magnetic resonance imaging. *The Journal of the Acoustical Society of America*, 140(2):EL159–EL165.

Wu, L. and Zhang, Z. (2023). Effects of implant and vocal fold stiffness on voice production after medialization laryngoplasty in an mri-based vocal fold model. *Journal of Biomechanics*, 149:111483.

Xue, Q., Mittal, R., Zheng, X., and Bielamowicz, S. (2012). Computational modeling of phonatory dynamics in a tubular three-dimensional model of the human larynx. *The Journal of the Acoustical Society of America*, 132(3):1602–1613.

Xue, Q., Zheng, X., Mittal, R., and Bielamowicz, S. (2014). Subject-specific computational modeling of human phonation. *The Journal of the Acoustical Society of America*, 135(3):1445–1456.

Yang, J., Wang, X., Krane, M., and Zhang, L. T. (2017). Fully-coupled aeroelastic simulation with fluid compressibility—for application to vocal fold vibration. *Computer methods in applied mechanics and engineering*, 315:584–606.

Yang, J., Yu, F., Krane, M., and Zhang, L. T. (2018). The perfectly matched layer absorbing boundary for fluid–structure interactions using the immersed finite element method. *Journal of fluids and structures*, 76:135–152.

Yin, J. and Zhang, Z. (2013). The influence of thyroarytenoid and cricothyroid muscle activation on vocal fold stiffness and eigenfrequencies. *The Journal of the Acoustical Society of America*, 133(5):2972–2983.

Yumoto, E., Sanuki, T., and Hyodo, M. (1999). Three-dimensional endoscopic images of vocal fold paralysis by computed tomography. *Archives of Otolaryngology–Head & Neck Surgery*, 125(8):883–890.

Zapater, E., Basterra, J., López, I., Oishi, N., and García-Lliberós, A. (2019). Use of individual anatomical variations to customise window location in montgomery implant thyroplasty: A case series study. *Clinical Otolaryngology*, 44(6):1162–1165.

Zapater, E., García-Lliberós, A., López, I., Moreno, R., and Basterra, J. (2014). A new device to improve the location of a montgomery thyroplasty prosthesis. *The Laryngoscope*, 124(7):1659–1662.

Zeiberg, A. S., Silverman, P. M., Sessions, R. B., Troost, T. R., Davros, W. J., and Zeman, R. K. (1996). Helical (spiral) ct of the upper airway with three-dimensional imaging: technique and clinical assessment. *AJR. American journal of roentgenology*, 166(2):293–299.

Zhang, K., Siegmund, T., Chan, R. W., and Fu, M. (2009). Predictions of fundamental frequency changes during phonation based on a biomechanical model of the vocal fold lamina propria. *Journal of Voice*, 23(3):277–282.

Zhang, Z. (2017). Effect of vocal fold stiffness on voice production in a three-dimensional body-cover phonation model. *The Journal of the Acoustical Society of America*, 142(4):2311–2321.

Zhang, Z., Chhetri, D. K., and Bergeron, J. L. (2015). Effects of implant stiffness, shape, and medialization depth on the acoustic outcomes of medialization laryngoplasty. *Journal of Voice*, 29(2):230–235.

Zheng, X., Bielamowicz, S., Luo, H., and Mittal, R. (2009). A computational study of the effect of false vocal folds on glottal flow and vocal fold vibration during phonation. *Annals of biomedical engineering*, 37(3):625–642.

Zheng, X., Mittal, R., and Bielamowicz, S. (2011). A computational study of asymmetric glottal jet deflection during phonation. *The Journal of the Acoustical Society of America*, 129(4):2133–2143.

Zheng, X., Xue, Q., Mittal, R., and Beilamowicz, S. (2010). A coupled sharp-interface immersed boundary-finite-element method for flow-structure interaction with application to human phonation. *Journal of biomechanical engineering*, 132(11):111003.

Zörner, S., Kaltenbacher, M., and Döllinger, M. (2013). Investigation of prescribed movement in fluid–structure interaction simulation for the human phonation process. *Computers & fluids*, 86:133–140.